

Dissertation

submitted to the

**Combined Faculties
for the Natural Sciences and for Mathematics
of the Ruperto-Carola University
of Heidelberg, Germany**

**for the degree of
Doctor of Natural Sciences**

presented by

**Dipl.-Phys. Oliver Schütz
born in: Munich, Germany**

**Oral examination:
February 9th, 2005**

Abstract:

This work presents a multi-wavelength search (near-IR, mid-IR, mm) for previously unknown circumstellar disks and a study of those disk candidate objects which are not yet well characterised in the literature. 22 candidate stars, most of these constituting known exoplanet systems, were examined for circumstellar material using the Adaptive Optics instrument ADONIS at La Silla Observatory (Chile). With the new Adaptive Optics system NAOS-CONICA at Paranal (Chile) we tested the technique of Polarimetric Differential Imaging. Advances in mid-IR data reduction were achieved, e.g., a method was developed to correct the chromatic and airmass dependent extinction. We show new N-band photometry and spectra for eight pre-main sequence stars, six main sequence stars and one post-MS object using the TIMMI2 camera at La Silla, and model the emission spectra with a mixture of silicates consisting of different grain sizes and composition. The most important result thereof is the discovery of two previously unknown circumstellar disks around HD 72106 and HD 113766. Both objects are host to highly processed silicates, resembling those found in solar-system comets. We further present the first observational confirmation for an extended circumstellar dust disk around ϵ Eri obtained with the bolometer array SIMBA at the 15 m radio telescope SEST in La Silla and demonstrate that the previously claimed disk substructure may alternatively be explained by remnant noise effects.

Zusammenfassung:

Die vorliegende Arbeit beschreibt eine Suche nach neuen, noch unbekanntem circumstellaren Staub-Scheiben im nahen und thermischen Infrarot sowie im Millimeter-Bereich. Ferner studieren wir mutmaßliche Scheiben, die in der Literatur erst unzureichend beschrieben sind. 22 Sterne, die zum Teil eine Scheibe besitzen könnten, wurden mit Adaptiver Optik (AO) und der Kamera ADONIS am Observatorium La Silla (Chile) untersucht. Mit dem AO-System NAOS-CONICA am Paranal (Chile) testen wir eine neue Nachweismethode für Scheiben: Differenzielle Polarimetrie. Für die Reduktion von Daten des thermischen Infrarots haben wir neue Methoden entwickelt, z.B. eine Möglichkeit die chromatische und von der Luftmasse abhängige Extinktion zu korrigieren. Wir zeigen bisher unveröffentlichte N-Band Photometrie und Spektren – aufgenommen mit der TIMMI2 Kamera in La Silla – für acht Vor-Hauptreihensterne, sechs Sterne der Hauptreihe und ein Objekt am Ende des Hauptreihenstadiums. Die Emissionsspektren modellieren wir mit bekannten Spektren von Silikaten verschiedener Zusammensetzung und Größe. Bei diesen Untersuchungen wurden bisher unbekannte Scheiben um die Sterne HD 72106 und HD 113766 gefunden. Beide Scheiben beinhalten Silikate in einem sehr weit fortgeschrittenen Entwicklungszustand, ähnlich jenen in Kometen unseres Sonnensystems. Wir zeigen ferner die erste Bestätigung einer großen Scheibe um ϵ Eri anhand von Daten, die mit dem Bolometer Array SIMBA am 15 m Radioteleskop SEST in La Silla gewonnen wurden. Die aus früheren Beobachtungen gefolgerte innere Struktur dieser Scheibe kann alternativ aber auch durch Rauscheffekte erklärt werden.

Contents

1	Introduction	1
1.1	Formation of stars and planets	1
1.2	Observation of circumstellar disks	3
2	Goal of this work	7
3	Near-infrared observations	9
3.1	Technical introduction	9
3.1.1	Observing in the near-IR	9
3.1.2	Adaptive Optics	9
3.1.3	The ADONIS instrument	12
3.1.4	The NAOS-CONICA instrument	12
3.2	A search for circumstellar dust disks with ADONIS	14
3.2.1	Introduction	14
3.2.2	Observation	14
3.2.3	Data reduction	17
3.2.4	Results	17
3.2.5	Discussion	19
3.2.6	Conclusion	23
3.3	Polarimetric Differential Imaging with NACO	25
3.3.1	Introduction	25
3.3.2	Observation and data reduction	27
3.3.3	Results	29
3.3.4	Discussion	30
4	Mid-infrared observations	33
4.1	Technical introduction	33
4.1.1	Observing in the mid-infrared	33
4.1.2	The TIMMI2 camera	34
4.1.3	The reduction pipeline for TIMMI2	36
4.1.4	Calibration of mid-IR data	37
4.2	Correcting the chromatic and airmass dependent extinction for TIMMI2 spectra	38
4.2.1	The influence of atmospheric extinction in the mid-IR	38
4.2.2	Data analysis	39
4.2.3	Results	41

4.2.4	Application to spectroscopic data	43
4.3	Disks around pre-main sequence stars	46
4.3.1	Introduction	46
4.3.2	Observed sources	47
4.3.3	Observations and data reduction	50
4.3.4	Analysis and modelling results	50
4.3.5	Discussion	55
4.3.6	Summary and conclusions	62
4.4	Disks around Vega-type and post-main sequence stars	63
4.4.1	Introduction	63
4.4.2	Observed sources	65
4.4.3	Observation and data reduction	67
4.4.4	Spectral Energy Distributions	68
4.4.5	Mid-IR spectral features	71
4.4.6	SIMBA measurements	73
4.4.7	Summary and conclusions	75
5	Millimeter observations	77
5.1	Technical introduction	77
5.1.1	The SEST	77
5.1.2	Observing with SIMBA	77
5.1.3	Concept of data reduction	79
5.2	SIMBA's view of the ϵ Eri disk	81
5.2.1	Introduction	81
5.2.2	Observation	82
5.2.3	Numerical simulations	83
5.2.4	Discussion	84
5.2.5	Conclusions	86
6	Summary and conclusion	87
A	Flatfield experiments with TIMMI2	91
A.1	Why are conventional flatfields not possible in the mid-IR ?	91
A.2	The current observing situation with TIMMI2	91
A.3	Basic ideas for creating a detector gain map	92
A.4	Realisation of a mid-IR flatfield	93
A.4.1	Observation at different airmasses	93
A.4.2	Clouds	93
A.4.3	Creating the flatfield from a science exposure	93
A.5	Application to test data	97
A.5.1	Photometry before applying the flatfield correction	97
A.5.2	Photometry after applying the flatfield correction	97
A.6	Conclusions	97
B	Acknowledgements	99
C	Acronyms	101

<i>CONTENTS</i>	ix
List of Figures	103
List of Tables	105
Bibliography	107

Chapter 1

Introduction

1.1 Formation of stars and planets

Historically, the *Nebular Hypothesis* by Laplace (1796) constitutes one of the first scientific explanations for the solar system's formation. It is based on previous ideas by Immanuel Kant and René Descartes. A rotating gas cloud is thought to shrink under its self-gravitation, while the speed of rotation increases due to angular momentum conservation. The cloud flattens to a disk, instabilities occur and the disk separates into rings in which the material accretes to planets.

Two further theories, although developed later, provide quite exotic explanations: In the *Tidal Theory*, proposed by Jeans (1922), the matter of which planets condensate was extracted from the Sun during a close passage of another star. The *Supernova Hypothesis* by Fred Hoyle (in 1944) considers a stellar companion to the Sun which underwent a supernova. Later, the planets were formed from its remnant material. Modern star and planet formation has much in common with the nebular hypothesis, which was revived in 1944 by Carl Friedrich von Weizsäcker.

According to modern theories, stars and planets form by a collapsing cloud of cold gas and dust when its gravitation dominates over the particles' kinetic energy. The cloud may fragment into various sub-clouds in which the (sub-)cloud's nucleus accretes to a protostellar core. Because of angular momentum conservation the matter cannot accrete directly onto the core and thus forms a circumstellar disk, parallelly rotating to the protostar. This disk is geometrically and optically thick, consisting to 99% of gas (dominated by H_2) while the 1% of dust primarily constitutes silicates. As angular momentum is lost in the disk by viscous friction, the material spirals further inward and finally accretes onto the star.

A protostar turns into a star when it reaches a critical inner temperature to support nuclear fusion. By this time the accretion comes to an end. In the remaining disk chemical differentiation has taken place. As a consequence of this, we find solid planets in the inner solar system and gas giants towards its outer part. The remaining gas disappears likely within the first 15 Myr during which planet formation is thought to be finished (Greaves et al. 2000, Pollack et al. 1996).



Figure 1.1: Upper panel: Near-infrared view of a class I disk. The star is only seen indirectly via the reflection nebula IRAS 04302+2247 it illuminates. The disk itself is visible edge-on as a dark band across the nebula. **Mid panel:** DG Tau B shows a stage between a class I and II disk. The disk midplane is still obscure, while the star can be seen directly in this near-IR image (it is, however, not visible in images of the same object at visual wavelengths). **Bottom panel:** β Pic (R-band image with coronagraph) is possibly the most prominent representative of a debris disk (class III), reflecting the stellar light. Only very few debris disks can be seen at optical wavelengths. (Image credit: upper and mid panel obtained from STScI press release 1999-05a, see also Padgett et al. 1999 for further information. Bottom panel: image by Paul Kalas, taken from Zuckerman 2001).

The silicate dust aggregates into macroscopic dimensions, later on forming larger bodies and planetesimals (e.g. Weidenschilling & Cuzzi 1993). These interact gravitationally and reach by collisions within 10^5 yr a further growth up to lunar sizes (e.g. Wetherill & Stewart 1993). In the final phase of terrestrial planet formation the large bodies continue colliding and merge. Remnant dust disks are supposed to disappear for a solar-like star after about 10 Myr, although for some stars they still are found up to an age of ~ 1 Gyr. This (dis)appearance of circumstellar disks depends on various factors (cf. Sect. 4.3).

The formation of Jovian planets is probably also based on aggregation of planetesimals into a large nucleus. However, when these reach a critical mass, a run-away gas accretion starts, whereas in those regions where terrestrial planets form the gas is already largely depleted. Jovian planet formation, however, may also be described by theories without a solid condensation nucleus.

In the outer region of the Solar System the planetesimal number density was not high enough to form planets. Due to gravitational interactions their orbits are not necessarily spherical. Today, this zone is referred to as *Kuiper Belt* and the objects therein are named *Trans-Neptunian Objects* (TNO). Pluto is just the largest among the TNOs and for historical reasons is still regarded as a planet, although after the discovery of several large-sized TNOs it does not fulfil the planet definition any longer.

1.2 Observation of circumstellar disks

The evolutionary stages from a protostellar cloud to a planetary system were described in the previous section. Lada (1987) defined a sequence in terms of the observable infrared (IR) excess, which later was amended by André et al. (1993) with the introduction of Class 0 sources:

- **Class 0 (protostellar core):** Gas and dust is accreting onto a protostellar core which is obscured at all wavelengths. The protostellar nebula may be visible in the far-IR or (sub-)mm (cf. Fig. 1.2).
- **Class I (evolved protostar):** An evolved protostar star is surrounded by a geometrically and optically thick accretion disk, accompanied by molecular outflows and jets parallel to the stellar rotation axis. While the outflows are a prominent observational feature, the protostar remains invisible at all wavelengths, as it is enshrouded by a spherical envelope of gas and dust. The disk midplane appears in images as a dark absorption band. The observed spectral energy distribution (SED) is rising between 2 and $100 \mu\text{m}$ (cf. Figs. 1.1 and 1.2).
- **Class II ('classical' T Tauri star, young Herbig Ae/Be star):** Accretion onto the star continues. The enshrouding shell has disappeared and the star becomes visible at optical wavelengths. In spectral energy distributions the slope is slightly decreasing longwards of $2 \mu\text{m}$ (cf. Fig. 1.2).

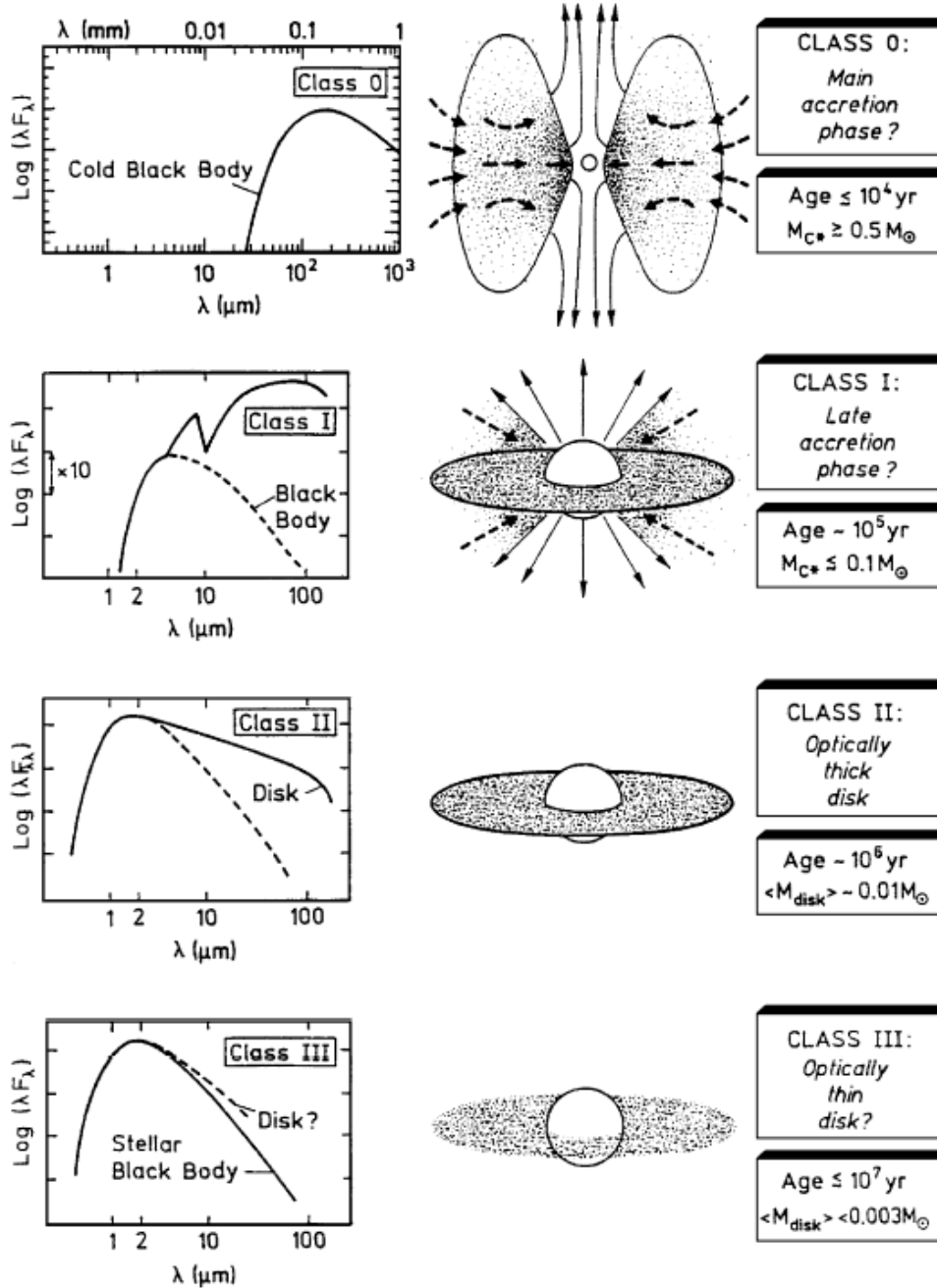


Figure 1.2: Characterisation of the Lada Classes 0-III in terms of their infrared excess and spectral energy distributions (left column). The middle figures illustrate the disk evolution. Ages in the right column correspond to a solar-like star. (Image credit: André 1994)

T Tauri stars (TTS) are progenitors of solar-like objects with masses up to $2 M_{\odot}$; during this stage they are referred to as 'classical' TTS. Herbig Ae/Be stars are the analogue to the TTS for intermediate mass stars between 2 and $8 M_{\odot}$.

- **Class III (debris disk):** No accretion on the star takes place any longer. The circumstellar material consists of remnants from the planet formation process. Most of the dust is 'secondary' generation, i.e. caused by collisions of planetesimals, and will gradually disappear with time. The SED resembles a reddened stellar blackbody (cf. Figs. 1.1 and 1.2).

We can obtain different insights into a disk depending on the wavelength of observation. Visual wavelengths are unsuited, beside of very few exceptions (e.g. Fig. 1.1, bottom panel), as a star will clearly outshine its surrounding disk or, for a class 0-I disk, no emission occurs at these wavelengths yet (cf. Fig. 1.2).

In the near-IR (1 - 5 μm) the disk is observable in scattered stellar light, while the central midplane of class I sources is still obscured. For class II and III objects, coronagraphy is commonly performed to image the disk.

At mid-IR wavelengths (approx. 5 - 30 μm) we observe the emission from various silicate compounds. The prominent emission feature around 10 μm is thought to arise from Si-O stretching modes in the tetrahedral silicate lattice, when these silicates are embedded in a hot surface layer of the inner disk (e.g. Chiang & Goldreich 1997). With the current mid-IR instrumentation, spectroscopy can be more instructive than attempts to image a disk (cf. Sects. 4.3 and 4.4). Advances to resolve disks with mid-IR interferometers have recently begun.

Observations at (sub-)millimeter wavelengths trace the cold dust towards the outer disk, resp. in case of a class 0 nebula this is the only possible method of observation. For optically thin disks (rather class III) their mass can be determined from millimeter photometry (cf. Sect. 4.4.6). Spatially resolved debris disk images were acquired by (sub-)millimeter interferometry.

Chapter 2

Goal of this work

We present a multi-wavelength search for previously unknown circumstellar disks together with a study of those disk candidate objects which are not yet well characterised in the literature. Our search is neither restricted to special types of stars nor to certain ages, however most of the observed sources are pre-main sequence or young main sequence stars. The detection methods presented are heterogeneous and the sections of this thesis may, in principle, be read independently. Each section provides its own introduction and conclusion.

In Sect. 3.2 a large sample of known planetary systems is investigated for the presence of circumstellar debris disks using Adaptive Optics coronagraphy. Subsequently, we test the new method of Polarimetric Differential Imaging in Sect. 3.3, which is a technique to enhance the contrast between a disk and the star: two orthogonally polarised images of the star are simultaneously observed and the unpolarised scattered light is removed by the subtraction of both beams.

A major part of this work describes mid-IR observations, which we successfully applied as a method to find previously unknown circumstellar disks. In Sect. 4.2 we describe a model to correct spectra for differential extinction. We analyse spectral dust features of eight pre-main sequence stars in Sect. 4.3 and find a new disk around HD 72106, a star which previously was de facto unknown in the literature. A corresponding sample of main sequence stars is investigated in Sect. 4.4. Therein, we discover another new disk around the star HD 113766. Both targets show extremely rich spectral dust features which hardly is observed in other young stellar objects.

A large number of theoretical publications provide explanations for the structures observed in the disk around ϵ Eri, relating these to dust being trapped in the resonance points of orbiting planets. However, this disk was never observationally confirmed. We performed its first confirmation and show in Sect. 5.2 that the observed disk substructure may rather be explained by remnant noise.

In Appendix A we discuss the flatfielding of mid-IR data, which is an unsolved problem up to now. The overall summary of this work is given in Sect. 6.

Chapter 3

Near-infrared observations

3.1 Technical introduction

3.1.1 Observing in the near-IR

Observations in the near-IR require a different strategy than at visual wavelengths. For the reader who may not be familiar with near-IR observing techniques, we recommend, for example, the good introduction given in the user manual of the Calar Alto MAGIC camera¹ written by T. M. Herbst & P. Bizenberger (both MPIA).

3.1.2 Adaptive Optics

At $\lambda = 2.2 \mu\text{m}$ (K-band) the VLT would possess a diffraction-limited resolution of $\lambda/D = 0''.057$. However, due to atmospheric turbulence the incoming wavefronts are deformed and the resolution is seeing-limited, which for Paranal during most of the nights lies between $0.4''$ - $1.2''$.

With a wavefront sensor (WFS) in an Adaptive Optics (AO) system the distortions in the wavefronts can be measured. These are analysed by a real-time computer which controls a tip-tilt mirror (compensating the tip and tilt in the wavefront) and – even more important – a deformable mirror (correcting the higher order aberrations). The latter one is a thin plate mirror controlled by piezoelectric actuators, that modify the mirror's shape. An indication for the quality of correction is given by the *Strehl ratio* (SR), which corresponds to the amount of light contained in the diffraction-limited core relative to the total source flux. A typical correction with NAOS-CONICA results in a Strehl ratio larger than 30% in the K-band. The SR, however, decreases (1) towards shorter wavelengths, i.e. especially in the J-band, (2) if the object for wavefront sensing is faint, not close to the science target or a narrow binary system with few arcsec separation or (3) if the atmospheric conditions are poor. In some of the before mentioned cases the SR may drop to just a few percent. The AO correction is

¹<http://www.mpia-hd.mpg.de/IRCAM/MAGIC/>

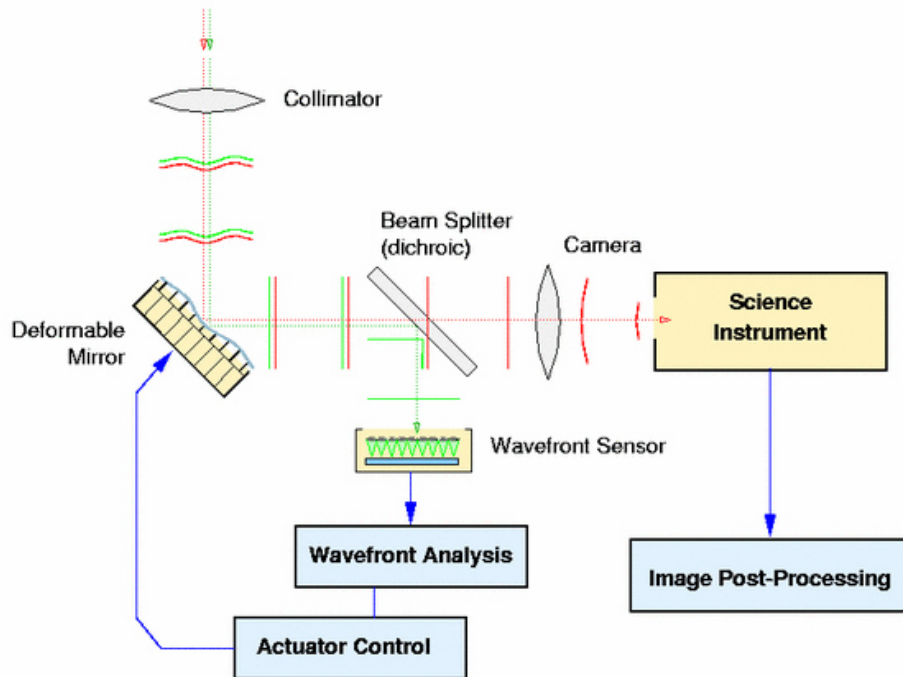


Figure 3.1: The science target (*red beam*) and a close reference star for wavefront sensing (*green beam*)— which may also be the same object – are observed simultaneously. From the measured wavefront distortions the computer calculates how the mirror must be deformed to correct the incoming wavefronts. (Image credit: Center for Adaptive Optics / USA)

applied in real-time via the deformable mirror and the residual wavefront distortions are measured again by the WFS. This operation is called 'closed loop' and displayed in Fig. 3.1.

The most frequently used type of WFS is a *Shack-Hartmann* array of identical lenslets (cf. Fig. 3.2), which can measure the slope of a wavefront. Each lenslet produces a miniature image of the object on a detector, called Shack-Hartmann spots. When the incoming wavefront is plane, all Shack-Hartmann spots appear in a regular grid defined by the geometry of the lenslet array. As soon as the wave-front is distorted, the spots become displaced from their nominal positions. The displacements of the spots' centroids in two orthogonal directions (x,y) are proportional to the wave-front slopes in the lenslet sub-apertures. A computer calculates from these displacements the commands sent to the actuators of the deformable mirror to correct the mirror shape correspondingly. The individual spots must be well sampled, however, each pixel of a CCD detector contributes a readout noise which dominates the photon noise for the faintest guide stars. Therefore, in some AO systems (e.g. at the Gemini Observatories) each spot is only projected on 2×2 detector pixel. The x,y slopes are then deduced from the intensity ratios within these pixel. Most other WFS, however, use larger subarrays.

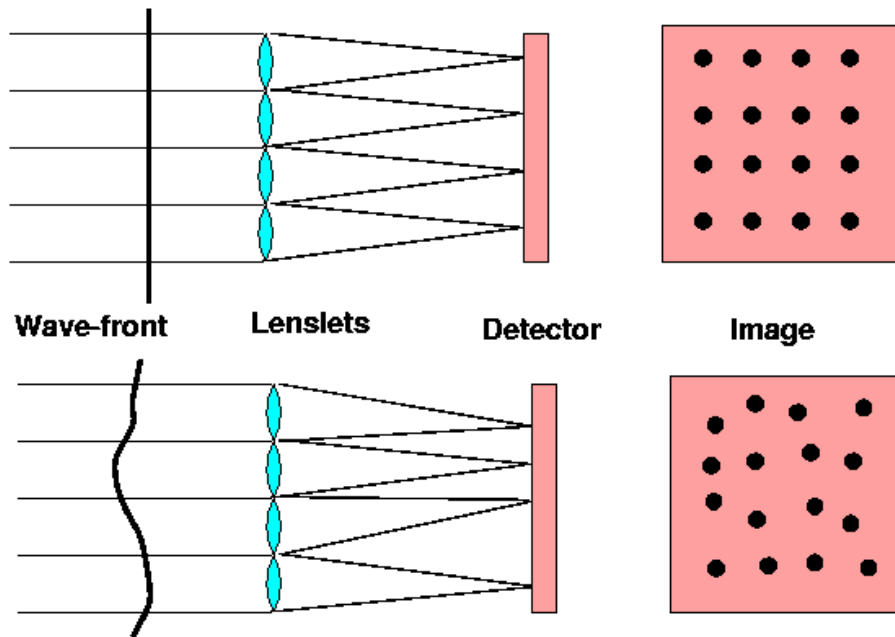


Figure 3.2: The principle of a Shack-Hartmann wavefront sensor as explained in the text. (Image credit: A. Tokovinin, CTIO observatory, Chile)

Curvature wavefront sensors measure the light's intensity distribution in defocused images obtained at an intra- and extra-focal position. Any local wavefront curvature will change the local intensity distribution in both images. Curvature wavefront sensors are used, for example, at the Gemini Observatories.

Pyramid wavefront sensors are a new technique currently under development. The wavefront sensor consists of a lens relay and an oscillating pyramidal-shaped prism, that is placed in the focal plane and dissects the stellar image into four beams. These are projected on a detector and their fluxes would be equal for a plane wavefront. Any wavefront slope changes the exact position of the source on the pyramid and thus also modifies the flux detected in each of the four beams. The normalised intensity differences are proportional to the wavefront slopes.

A good tutorial of Adaptive Optics with a more mathematical description is maintained on-line² by A. Tokovinin (CTIO).

²<http://www.ctio.noao.edu/~atokovin/tutorial/>

3.1.3 The ADONIS instrument

ADONIS (ADaptive Optics Near Infrared System) is a complete Adaptive Optics system installed at the ESO 3.6 m telescope in La Silla. It was operated between the years 1993 to 2002.

Reference wavefront sensing is done in the visual with two types of Shack-Hartmann sensors to permit bright as well as fainter reference stars. The high-flux Shack-Hartmann WFS is an intensified Reticon operating with reference stars brighter than $V = 8$ mag, while the other Shack-Hartmann sensor, for reference stars between 8 and 12.5 mag, is an Electron Bombarded CCD (EBCCD). Each object used for wavefront sensing must be located within $30''$ from the science target. Even better, it may be the target itself, providing its intrinsic angular size is smaller than $3''$. Above a maximal zenith angle of 50° the correction efficiency decreases rapidly.

Near-IR observations are performed with one of the two cameras described below, which together cover the entire near-IR ($1 - 5 \mu\text{m}$).

A coronagraph can be attached as a pre-focal optics which allows to insert different sizes of occulting masks. More details about coronagraphy with ADONIS is given in Sect. 3.2.

SHARPII+ camera

SHARPII+ is based on a 256×256 Nicmos III (HgCdTe) detector array which is sensitive at $1 - 2.5 \mu\text{m}$. With a fast shutter at the internal cold Lyot stop integration times shorter than 300 ms can be realised (down to a minimum of 20 ms). Available lens scales are $0''.1/\text{pixel}$ ($25.6'' \times 25.6''$), $0''.05/\text{pixel}$ ($12.8'' \times 12.8''$) and $0''.035/\text{pixel}$ ($8.5'' \times 8.5''$). The known Nicmos III remanence effect influences also SHARPII+. To avoid detector artefacts, wait frames have to be taken between observations of a target and the sky (i.e. the detector is read without saving the data to a file).

COMIC camera

COMIC is optimised for observations in the L and M bands, although the 128×128 HgCdTe detector array – in principle – is sensitive in the entire near-IR. Available lens scales are $0''.1/\text{pixel}$ ($12.8'' \times 12.8''$) and $0''.035/\text{pixel}$ ($4.5'' \times 4.5''$).

3.1.4 The NAOS-CONICA instrument

NAOS (Nasmyth Adaptive Optics System) and the near-IR camera CONICA constitute the NAOS-CONICA system, often referred to as *NACO*.

Two wavefront sensors are implemented in NAOS, one operating in the visible, the other in the near-IR. To permit a wide range of objects for wavefront sensing, both WFS can be operated in various configurations with different Shack-Hartmann lenslets

Table 3.1: List of cameras, plate-scales and fields of view.

Camera	Scale [mas/pixel]	FOV ["]	Spectral Range
S13	13.25	14 × 14	1.0 - 2.5 μm
S27	27.03	28 × 28	1.0 - 2.5 μm
S54	54.3	56 × 56	1.0 - 2.5 μm
L27	27.12	28 × 28	2.5 - 5.0 μm
L54	54.7	56 × 56	2.5 - 5.0 μm
SDI	17.25	5 × 5	1.6 μm

and pixel binning. The five dichroics, splitting the light from the telescope between the NAOS wavefront sensor and CONICA, differ with regard to the amount and wavelength of the light reflected to the WFS resp. transmitted to CONICA. Natural guide stars can be selected within 55" from the science target, while the obtained SR decreases in case of large distances. The limiting brightness for reference stars is 12 mag in the infrared WFS and 16 mag for the visual WFS.

CONICA is permanently attached to NAOS and equipped with a 1024 × 1024 pixel Aladdin (InSb) detector, sensitive at 1 - 5 μm . In May 2004 (after the observations described in Sect. 3.3) the detector was upgraded to an Aladdin 3, which possesses a larger dynamical range to reduce saturation effects. Some electronical and optical ghost features are known for bright sources.

NACO permits imaging, coronagraphy, long-slit spectroscopy and imaging polarimetry. New observing modes are still added. For an up to date instrument status, please see the instrument webpage and its manual³. Three cameras with different field of view (FOV) are available for observations between 1 - 2.5 μm and two cameras for the wavelength range 2.5 - 5 μm . The Simultaneous Differential Imager (SDI) was recently added, which is specialised for on-off imaging in the 1.6 μm methane band, an important wavelength region for the detection of extrasolar planets. Table 3.1 lists the cameras, fields of view and pixel scales.

A Wollaston prism and wire grid polarisers are available for imaging polarimetry. The Wollaston splits the incoming light into an ordinary and extra-ordinary beam, thus each source appears twice on the detector. To avoid source overlapping, e.g. for stellar fields, a mask is inserted into the focal beam, consisting of alternating opaque and transparent stripes. The Wollaston prism needs to be rotated in steps of 45° to measure the Stokes parameters and the degree and position angle of polarisation, which is achieved by rotating the entire instrument. J-band polarimetry is not possible, since the J-band filter is mounted in the same wheel as the Wollaston and the wire grids. The polarisation induced by the instrument itself is assumed to be 1-2%. A definition of the Stokes vectors and further details on polarimetric observing techniques are given in Sect. 3.3.

³<http://www.eso.org/instruments/naco>

3.2 A search for circumstellar dust disks with ADONIS

We present results of a coronagraphic imaging search for circumstellar dust disks with the Adaptive Optics Near Infrared System (ADONIS) at the ESO 3.6 m telescope in La Silla (Chile). 22 candidate stars, known to be orbited by a planet or to show infrared excess emission, were examined for circumstellar material. In the PSF-subtracted images no clear disk was found. We further determine the detection sensitivities and outline how remaining atmospheric fluctuations still can hamper adaptive optics observations.

3.2.1 Introduction

Observations of circumstellar matter and searches for new disks bring further understanding on the process of planetary system formation and evolution: in some young and spatially resolved disks, observed with the HST, the existence of asymmetrical structures is attributed to a yet unknown massive body (e.g. in the case of HD 163296, see Grady et al. 2000). Similar conclusions have been drawn from sub-mm observations of dust around Vega and Fomalhaut (Wilner et al. 2002, Holland et al. 2003). Most of the currently known extrasolar planets orbit stars with an age similar to the Sun, where disks already should have disappeared or their emission would be very faint. Therefore, disk detections are often ambiguous. In the case of 55 Cnc, for example, which is a system with three planets, a disk of 40 AU extension and 27° inclination was claimed (Trilling & Brown 1998; Trilling et al. 2000). Later, from sub-mm observations the disk mass was determined (Jayawardhana et al. 2000). With NICMOS/HST, however, it was not possible to confirm these previous detections (Schneider et al. 2001). For remnant disks an upper lifetime of 400 million years is currently assumed (e.g. Habing et al. 2001).

In this section we present results from a ground-based, Adaptive Optics (AO) search for yet unknown circumstellar disks around stars with planets or IR-excess. Some known disks are added for comparison. We outline in Sect. 3.2.5 similar surveys by other authors obtained *after* our studies.

3.2.2 Observation

Program goal and observing equipment

The goal of our observing program was the detection of new disks as well as the search for structures caused by unseen planets in known circumstellar disks. To reach an optimal resolution and brightness contrast we used the ESO Adaptive Optics Near Infrared System (ADONIS) mounted to the 3.6 m telescope at La Silla Observatory (Chile). Typical Strehl ratios are around 0.1 in J-band and 0.3 in K-band. Three observing runs of eight nights in total were allocated to this project between June 2000 and October 2001. ADONIS had been coupled with the near-IR camera SHARPII+ which operates in the J- to K-band. We further attached a fully opaque coronagraphic

Table 3.2: Presentation of our target sample and their stellar parameters. The objects were selected either because of an existing planetary system or observational hints for a disk. See the column *remarks* for a classification of the targets (we do not distinguish between a single planet or a planetary system). Three resolved disks were also included. V-band fluxes are taken from SIMBAD and near-IR fluxes from the 2MASS catalogue. The distances are obtained either via the *Extrasolar Planets Encyclopaedia* (cf. footnote 4) or the cited papers. Where none of this was available the distance is estimated from Hipparcos parallaxes.

- (1) HD 141569: Resolved disk (Clampin et al. 2003)
(2) HD 163296: Resolved disk (Grady et al. 2000)
(3) HD 207129: Unresolved disk (Jourdain de Muizon et al. 1999)
(4) HR 4796: Resolved disk (Augereau et al. 1999a)

Star	d [pc]	Type	V [mag]	J [mag]	H [mag]	K [mag]	Date of Observation	Remarks
HD 142	20.6	G1IV	5.70	4.69	4.65	4.47	Oct. 2001	planet
HD 1237 (= GJ 3021)	17.6	G6V	6.59	5.37	4.99	4.86	Oct. 2001	planet
HD 4208	33.9	G5V	7.79	6.57	6.24	6.16	Oct. 2001	planet
HD 23079	34.8	F8/G0V	7.1	6.03	5.81	5.71	Oct. 2001	planet
HD 33636	28.7	G0V	7.06	5.93	5.63	5.57	Oct. 2001	planet
HD 52265	28.0	G0V	6.30	5.24	5.03	4.95	Oct. 2001	planet
HD 82943	27.5	G0	6.54	5.51	5.25	5.11	Apr. 2001	planet
HD 102647 (= β Leo)	11.1	A3V	2.14	1.85	1.93	1.88	Apr. 2001	IR-excess
HD 134987	25.7	G5V	6.45	5.27	5.12	4.88	Apr. 2001	planet
HD 139664	17.5	F5IV-V	4.64	4.02	3.73	3.80	Apr. 2001	IR-excess
HD 141569	99	B9.5Ve	7.0	6.87	6.86	6.82	Jun. 2000	known disk ⁽¹⁾
HD 155448	~600	B9	8.72	8.65	8.51	8.53	Jun. 2000	IR-excess
HD 158643 (= 51 Oph)	131	A0V	4.81	4.90	4.71	4.30	Jun. 2000	PMS star
HD 160691	15.3	G3IV-V	5.15	4.16	3.72	3.68	Apr. 2001	planet
HD 163296	122	A1Ve	6.87	6.20	5.53	4.78	Jun. 2000	known disk ⁽²⁾
HD 179949	27.0	F8V	6.25	5.30	5.10	4.94	Apr. 2001	planet
HD 207129	15.6	G0V	5.58	4.72	4.31	4.24	Apr. 2001	IR-excess ⁽³⁾
HD 217107	37.0	G8IV	6.18	4.95	4.76	4.54	Oct. 2001	planet
HD 319139	?	K5	10.5	8.07	7.44	7.25	Jun. 2000	T Tauri
HR 4796	67	A0V	5.78	5.78	5.79	5.77	Jun. 2000	known disk ⁽⁴⁾
HT Lup	~160	Ge	10.4	7.57	6.87	6.48	Jun. 2000	T Tauri
SAO 185668	?	B3	9.64	8.66	8.55	8.50	Jun. 2000	IR-excess

mask in front of the Lyot (pupil) stop to reject the peak of the PSF. This is necessary to increase the integration time and sensitivity in order to reveal the much fainter emission from circumstellar material. Details on the coronagraph and its performance are given in Beuzit et al. (1997). We iteratively centered the star 'behind' the mask. To account for the different distances of our targets and thus the varying disk size, coronagraphic masks with three different diameters were used (0.84'', 1.0'' and 1.4''). These can also be applied to study one object with various sensitivity. Most of the images were acquired with the 1.0'' mask.

The targets

In June 2000 we focused on young stars which were known or suspected to possess a circumstellar disk. In April 2001 we selected stars with known planetary companion, where the survival of a remnant disk is likely. Some targets with IR-excess were also included in this run. The search for remnant disks around recently discovered planetary systems was continued in October 2001. Notes for all targets are shown in Table 3.2. Further references of the planet parameters can be obtained from the *Extrasolar Planets Encyclopaedia*⁴ maintained by Jean Schneider.

Observing technique

Beside of photometric standard stars, all data were acquired with the object centered behind the coronagraphic mask. We performed the integrations by co-adding several exposures, each single frame taken with the longest reasonable detector integration time, which depending on the targets' brightness was between 0.3 and 60 seconds. The total co-added times are shown in Table 3.3. Two reference stars (to the best of our knowledge without circumstellar matter) were observed in an alternating sequence with each target for a later subtraction of the point-spread-function (PSF). To reject eventual influences of atmospheric instabilities on the adaptive optics correction, one *PSF1-Target-PSF2* cycle was limited to approx. 30 minutes (including all overheads), then the sequence was repeated several further times. Any possible circumstellar matter must be firmly detected in the PSF-subtracted images of each cycle to exclude artefacts caused by atmospheric variations.

From previous ADONIS observations a different response of the adaptive optics correction with regard to the stellar brightness was known. This can result in Strehl ratio variations while it is essential to maintain the conditions between target and PSF star. Therefore, PSF calibration stars were selected which differ not more than 0.3 mag in brightness from the science target, which also have a similar spectral type and which are spatially close to the target (a few degrees).

⁴<http://www.obspm.fr/planets>

3.2.3 Data reduction

Basic data reduction

All raw data were inspected in order to exclude eventual bad images, e.g. structures caused by irregular electrical noise. Data cube clean-up, dark and flatfield correction as well as sky subtraction were performed in a standard way. Flux calibration was achieved via aperture photometry of photometric standard stars.

PSF subtraction

The main reduction step is the optimal subtraction of a reference PSF from the target PSF to unveil the faint circumstellar disk. We use a software developed by E. Pantin (Pantin et al. 2000). For each pair of disk candidate image (Obj) and corresponding PSF the following parameters have to be determined: a scaling factor R , sub-pixel shifts δx and δy between both images in x and y directions, the residual background Bg and the noise standard deviation σ . These parameters are determined by minimising the penalty functional

$$J = \sum_{pixel} \frac{\left(Obj - \left(\text{shift}\left(\frac{PSF}{R}, \delta x, \delta y\right) - Bg\right)\right)^2}{\sigma^2}. \quad (3.1)$$

The sum is performed over pixels inside a precise mask, not too close to the star, nor too far. Via a software interface showing the resulting image of the optimal PSF subtraction the data reducer checks the numerically obtained fit and can further optimise the subtraction by adjusting some of the parameters. To get an impression of the natural residues, also the two PSF stars are subtracted from each other.

3.2.4 Results

Reduction artefacts

During the reduction process we became aware of several artefacts which despite of a very careful PSF subtraction may occur. These can be characterised as follows:

- (a) Diffraction spikes resulting from the mounting of the coronagraphic mask: these are stripes of varying intensity and thickness along the wires holding the coronagraphic mask, i.e. at 0° modulo 90° . They are uncritical and can be hidden with an artificial mask created by our reduction software.
- (b) Small rings close to the mask: as a result of an imperfect centering, sickle-shaped structures can appear close to the coronagraphic mask. Since they are always very close to the mask position, they are easily identified as artefacts and can also be hidden with a software mask.

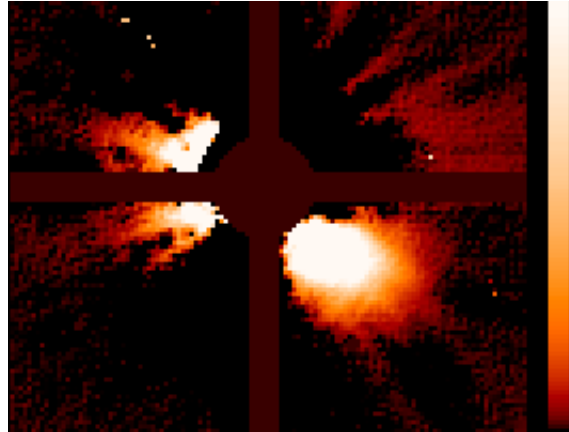


Figure 3.3: Looking like an edge-on disk around HD 142 (J-band), this is just a very special artefact which we explain in (3.2.4c). Intensities therein are scaled logarithmically. Recognisable is the software mask in form of a cross, which is laid over artefacts caused by the coronographic mask. The diameter of the circular mask corresponds to $\sim 1.2''$.

- (c) Diffraction spikes resulting from the support structures of the telescope's secondary mirror: in our special telescope-instrument configuration thin lines at position angles 45° modulo 90° sometimes can be seen, which originate from the mounting of the telescope's secondary mirror. In rare cases and in coincidence with PSF instabilities due to atmospheric variations, these lines may form bright stripes or cause unpredictable results. A very interesting example of this is shown in Fig. 3.3.
- (d) Variations in the PSF shape due to atmospheric fluctuations: speckles, which result from atmospheric turbulence, can also influence an adaptively corrected PSF for any ground-based observation. As shown in Racine et al. (1999) the speckle noise dominates all other sources of noise (photon, sky and read noise) within the halo. In our data we saw that during unstable atmospheric conditions the PSF shape can even vary within the short time between observation of a target and its corresponding reference star. This naturally results in Strehl ratio fluctuations and a subtraction of these frames would show a circumstellar halo resembling a face-on disk as in Fig. 3.4.

Disk search and upper limits for disk magnitudes

In the PSF-subtracted images of all targets no clear evidence for a disk could be found within the detection sensitivities. In order to estimate for which brightness an eventually existing disk would have been detectable, we carried out a PSF subtraction with artificial disks added to one of the two reference stars. Instead of the target both reference stars were chosen, since we must be sure to use stars without circumstellar matter. As simple-case approximation we used circular, face-on disks with a surface brightness $I(r) = I_0$, i.e. without a radial dependence. I_0 was successively reduced until the disk

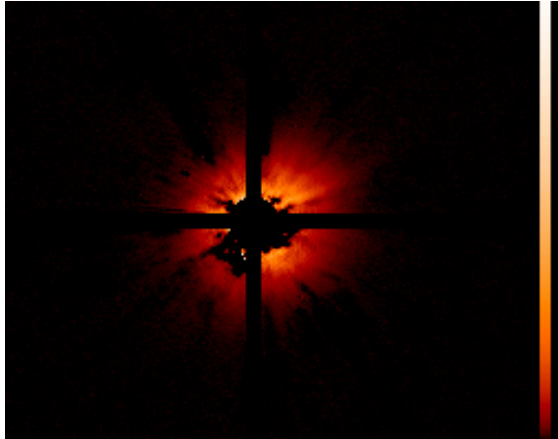


Figure 3.4: This 'face-on disk' around HD 160691 (J-band) was caused by variations in the PSF shape due to atmospheric fluctuations as described in (3.2.4d). The intensity is displayed logarithmically. In the software mask the circular part's diameter is $\sim 1.0''$.

could no longer be revealed by PSF subtraction. The corresponding values are given as $\text{mag}/\text{arcsec}^2$ in Table 3.3. Since both the disk radius and I_0 were modified, this allows also to conclude on the detectability of disks with other inclinations than face-on. The upper limits determined for an edge-on disk would depend strongly on its orientation and it was not our goal to determine limits for a special, most-favourable case. Realistic disk radii between 25 AU and 100 AU have been chosen for the older and closer stars (11 - 37 pc) of the runs in April and October 2001. Radii up to 1000 AU were used for the young stars observed in June 2000, which are located at larger distances around 70 - 600 pc. For HD 4208, HD 33636 and HD 217107 a more detailed analysis of the radial dependence is shown, and the brightness difference of the star and the disk's limit of detectability is plotted in Fig. 3.5 as function of angular separation.

3.2.5 Discussion

As can be recognised from Table 3.3 the detection of circumstellar material with coronagraphy and PSF subtraction still is quite insensitive close to the star, but improves with larger distance. For those targets, where a resolved circumstellar disk is known, we compared the published surface fluxes with the limiting magnitudes from Table 3.3 and the appropriate disk radii. For HD 141569 ($R_{\text{disk}} \sim 500$ AU) Augereau et al. (1999b) report an H-band surface flux two magnitudes below our detection limit. A difference in brightness applies similar for the K_s -band when comparing our values with observations from Boccaletti et al. (2003). Our detection limit for HR 4796 ($R_{\text{disk}} < 100$ AU) is one magnitude brighter than the flux given by Augereau et al. (1999a) for the corresponding separation. A detection of these known disks was marginally missed, but would have been feasible with more integration time.

In order to check whether the atmospheric fluctuations can be identified as the primary cause for the reduced image quality, we now examine the influence of scattered light –

Table 3.3: Integration times and disk magnitude limits. The latter ones were determined with artificial disks of the sizes shown in this table. No disk was found down to the given surface brightness. The reduction routine has a lower performance for stars in clusters and a determination of brightness limits was sometimes not possible. These cases are indicated with '-'. Estimated errors for the given magnitudes are ± 0.2 mag. The disk brightness limit as a function of disk radius was studied in more detail for the targets HD 4208, HD 33636 and HD 217107 with further radii 1.0, 1.8, 2.5, 3.3, 4.0 and 4.8'' (cf. Fig. 3.5). Disks with radii $> 5.0''$ are too big for a detection with our software (since they would cover large parts of the detector, which makes them unphysical anyway). The S/N-ratio is the S/N per pixel and was calculated as described in Sect. 3.2.5.

- (1) The distances of HD 319139 and SAO 185668 are unknown.
- (2) A faint object at 4.7'' distance to HR 4796 turned out to be a background star, which was also identified by Mouillet et al. (1997).

Star	Filter	t_{exp} [min]	R_{disk} [AU]	Sep. [']	Limit [mag/'' ²]	S/N
HD 142	J	5	50	2.5	14.2	4.1
			75	3.7	16.7	4.3
			100	4.9	15.0	3.5
	H	5	50	2.5	14.9	3.5
			75	3.7	17.1	3.5
			100	4.9	16.4	2.5
HD 1237 (= GJ 3021)	J	5	50	2.9	16.0	3.6
			75	4.3	16.7	2.7
	H	7	50	2.9	14.6	4.0
HD 4208	H	8	75	4.3	15.6	3.1
			34	1.0	13.1	
			50	1.5	14.6	2.5
			59	1.8	15.6	
			75	2.2	15.9	2.7
			85	2.5	16.4	
HD 23079	J	5	100	3.0	16.4	2.1
			110	3.3	17.1	
			136	4.0	17.1	
			161	4.8	17.7	
			50	1.5	13.5	2.3
			75	2.2	15.2	2.6
HD 33636	J	5	100	2.9	16.0	2.4
			29	1.0	13.5	
			50	1.8	15.0	2.6
			72	2.5	16.7	
			75	2.6	16.7	3.1
			93	3.3	17.5	
HD 52265	J	10	100	3.5	17.5	2.6
			115	4.0	17.5	
			136	4.8	17.5	
			50	1.8	14.2	2.6
			75	2.7	16.0	2.6
			100	3.6	16.0	2.3

Table 3.3 (continued)

Star	Filter	t_{exp} [min]	R_{disk} [AU]	Sep. [$''$]	Limit [mag/ $''^2$]	S/N
HD 82943	H	2	25	0.9	11.9	1.6
			50	1.8	14.6	4.0
			75	2.7	16.3	6.0
HD 102647 (= β Leo)	H	2	25	2.3	13.1	3.6
			50	4.5	14.6	5.1
HD 134987	J	2	25	1.0	13.2	1.8
			50	2.0	15.9	3.8
			75	3.0	15.9	4.9
	H	2	25	1.0	12.3	1.8
			50	2.0	13.8	3.2
			75	3.0	15.3	3.7
HD 139664	J	3	25	1.5	13.6	2.8
			50	2.9	15.1	6.6
			75	4.3	15.9	9.1
HD 141569	H	5	500	5.0	14.8	5.2
			1000	10.0	15.5	3.7
	K_s	5	500	5.0	14.5	4.3
			1000	10.0	15.3	2.5
HD 155448	H	10	1000	2.0	-	-
HD 158643 (= 51 Oph)	H	5	500	3.9	13.7	-
			1000	8.0	16.2	-
	J	2	25	1.7	12.9	2.8
HD 160691	H	3	50	3.3	15.1	5.1
			75	4.9	15.1	5.1
			25	1.7	13.1	2.8
	H	3	50	3.3	14.6	5.8
			75	4.9	14.6	6.5
			500	4.1	15.5	3.1
HD 163296	H	6	1000	8.0	16.2	-
			25	1.0	12.6	2.0
HD 179949	H	1	50	1.9	15.3	3.8
			75	2.8	16.3	5.5
			25	1.6	12.9	6.5
HD 207129	J	3	50	3.2	14.4	6.5
			75	4.8	15.1	7.8
			25	1.6	12.9	6.5
HD 217107	J	5	37	1.0	12.3	
			50	1.4	13.8	2.4
			65	1.8	15.2	
			75	2.1	15.2	3.0
			93	2.5	16.7	
			100	2.7	16.7	3.4
			120	3.3	16.7	
			148	4.0	17.5	
HD 319139	H	5	* ⁽¹⁾	5.0	18.0	2.9
			* ⁽¹⁾	10.0	17.3	2.7

Table 3.3 (continued)

Star	Filter	t_{exp} [min]	R_{disk} [AU]	Sep. [']	Limit [mag/'' ²]	S/N
HR 4796 ⁽²⁾	H	5	100	1.5	12.6	1.0
			500	7.5	17.3	2.4
	K _s	1	100	1.5	11.5	1.4
			500	7.5	16.5	2.0
HT Lup	H	5	500	3.1	16.4	2.6
			1000	6.0	17.6	1.9
	K _s	5	500	3.1	15.3	2.6
			1000	6.0	16.5	2.3
SAO 185668	H	10	* ⁽¹⁾	1.0	-	-
			* ⁽¹⁾	5.0	-	-

both by the atmosphere and the telescope – on our simulated disks. According to Roddier & Roddier (1997) the amount of stellar light scattered by atmospheric turbulence (speckle noise) decreases with the radius r from a star like $r^{-11/3}$. For distances larger than $\sim 3''$ scattering by the optical surface roughness of the telescope mirror becomes dominant, which approximately decreases like r^{-2} . Our signal S within the simulated disks consists of the radial dependent stellar flux and the model disk with a constant surface brightness:

$$S = F_*(r) + F_{\text{disk}} \quad (3.2)$$

The photon noise N is defined by the halo flux of the star at distance r :

$$N = \sqrt{F_*(r)} \quad (3.3)$$

We would expect to have a radial dependence in the S/N-ratio going with r^2 in case of scattering by the atmosphere and with r in case of scattering by optical surface roughness. The S/N in Table 3.3 is the S/N per pixel, calculated within a box of 10×10 pixel at the given radius and averaged over measurements at four position angles which were free of any artefacts. These values are shown in Fig. 3.6 sorted according to observing run and averaged for each radius over observations in all filters. Results for different runs were not merged in order to account for long-time weather variability between the seasons. From the three plots in Fig. 3.6 no conclusive results can be seen whether the S/N-ratio behaves like r or r^2 . In the runs of both June 2000 and May 2001 different slopes appear for small resp. larger distances from the star. We speculate that the inner slope could rather be interpreted as a dependence similar to r^2 as expected in case of scattering by the atmosphere, while the slope to larger distances shows a rather linear contribution as expected for scattering by the optical surface roughness of the telescope mirror.

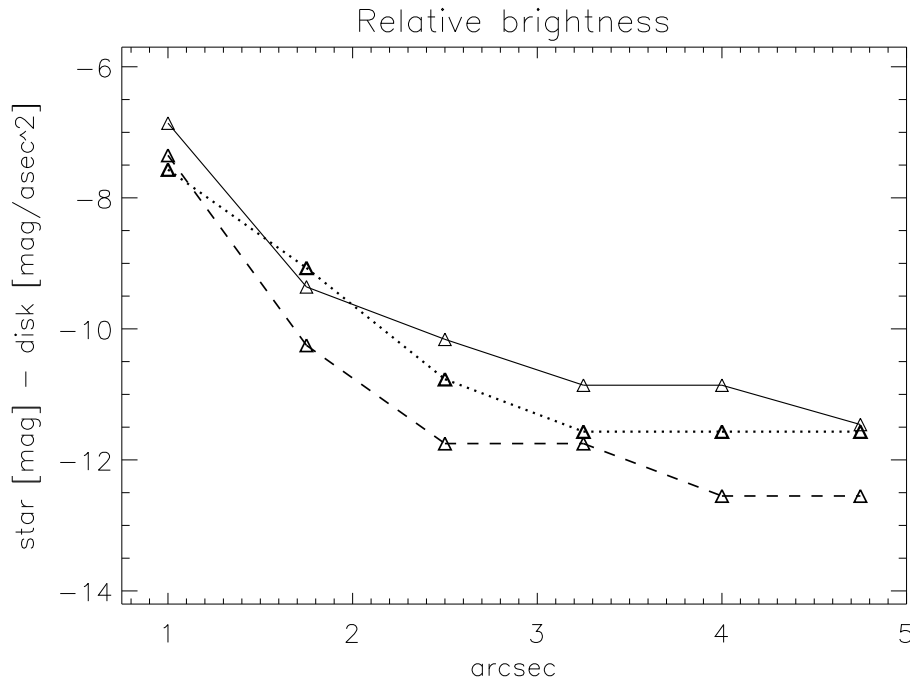


Figure 3.5: Brightness difference of the star and the disk’s detectability limit as function of angular separation. Examples are shown for three targets from Table 3.3. The dashed line represents HD 217107 (J-band), the dotted line HD 33636 (J-band) and the solid curve is HD 4208 (H-band).

We finish the discussion with an outline of more recent disk surveys around exoplanet host stars. Saffe & Gómez (2004) assembled optical to mid-IR spectral energy distributions for 61 exoplanet host stars and collected optical polarisation data for 26 of these. The authors conclude that some objects have a similar mid-IR excess and optical polarisation as found for Vega-type stars. It must be denoted, however, that in many cases IRAS upper limits were taken. Greaves et al. (2004) examined eight nearby stars with known giant planets at sub-mm wavelengths, but found no significant emission.

In a follow-up observation of HD 155448 with the mid-IR camera TIMMI2 (Sect. 4.1) we find an unexpectedly large resolved structure, possibly originating from an extended PAH shell. This is supported by PAH spectral features around $11.2 \mu\text{m}$. Due to bad weather these TIMMI2 observations must be repeated and we cannot present details yet within this work.

3.2.6 Conclusion

In our data taken with the SHARPII+/ADONIS system we did not find any clear circumstellar disk. For the known disks the non-detections were caused by insuffi-

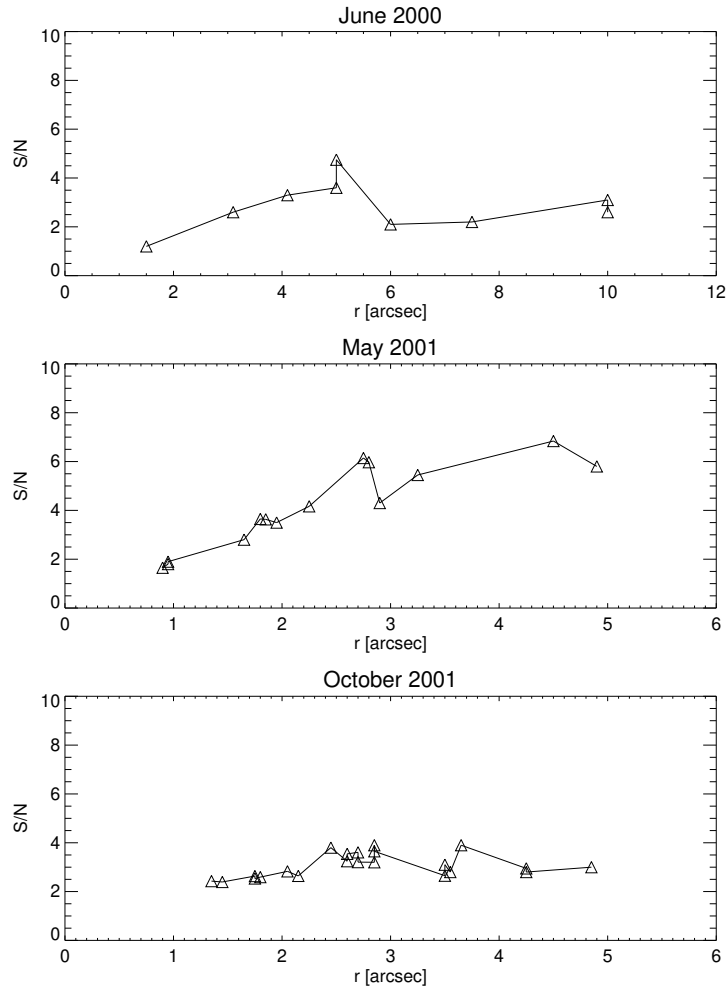


Figure 3.6: The S/N of the simulated disk detections averaged for each radius over observations in all filters.

cient sensitivity and the intrinsic limitations of ground-based AO systems described in Sect. 3.2.4.

Many searches for circumstellar material are carried out with AO and coronagraphy. This requires a very stable PSF plus a really high Strehl ratio ($> 80\%$, see Sivaramakrishnan 2001), but from any ground-based optical system the PSF stability is limited by atmospheric speckle noise or variations in the width of the PSF caused by atmospheric instabilities. In the latter case, subtracting the PSF of a reference star taken at different atmospheric conditions some minutes before or after the target star, can mimic the existence of a face-on disk. Also, the required Strehl ratio $> 80\%$ is not reached with current telescope-instrument configurations.

Dual-imaging techniques like differential polarimetric imaging avoid these problems (Kuhn et al. 2001, Apai et al. 2004): the light from a circumstellar disk is linearly

polarised while star light scattered in the earth atmosphere is unpolarised. Two orthogonal polarisation states will be observed simultaneously with a Wollaston prism. Since the atmospherically scattered speckle patterns are unpolarised, the difference image from these two orthogonal polarisations will contain only the polarised light of the real circumstellar disk. Subtraction of a reference PSF – with all the artefacts that may be induced by this – is not required.

Coronagraphy of circumstellar disks repeatedly has led to false disk detections in the literature. These disk detections should always be followed by observations at other wavelengths (mid-IR, mm) or by spectroscopy.

3.3 Polarimetric Differential Imaging with NACO

3.3.1 Introduction

The technique of Polarimetric Differential Imaging (PDI) was first described by Kuhn et al. (2001) as a possibility to trace the scattered, i.e. polarised, light from a circumstellar disk very close towards the central star. The basic idea is to subtract two simultaneously acquired, orthogonally polarised images of a target. A Wollaston polariser splits the light into an ordinary and extra-ordinary beam with a phase difference of 90° . The star's signal as well as light scattered in the earth-atmosphere – known as speckle noise – are unpolarised and thus efficiently removed by taking the difference of both beams. This method may become important to study the inner regions of circumstellar disks, as the contrast between the disk and the central star is enhanced with regard to common or coronagraphic imaging.

The Wollaston prism is typically rotated to polarisation angles of 0° , 45° , 90° and 135° . To construct an image from the polarisation maps, data must at least be obtained at polarisation angles of 0° and 45° or, respectively, at 90° and 135° . However, to eliminate also the polarisation induced by the instrument optics (approx. 1-2%), data should be acquired at all four polarisation angles.

A subtraction of the two orthogonally polarised beams in each exposure gives the Stokes Q and Stokes U vectors, which are projections of the polarisation vector. Prior to the correction of instrumental polarisation we denote these vectors as Q' , Q'' , U' and U'' :

$$0^\circ : Q' = I^0 - I^{90} \quad (3.4a)$$

$$45^\circ : U' = I^{45} - I^{135} \quad (3.4b)$$

$$90^\circ : -Q'' = I^{90} - I^0 \quad (3.4c)$$

$$135^\circ : -U'' = I^{135} - I^{45} \quad (3.4d)$$

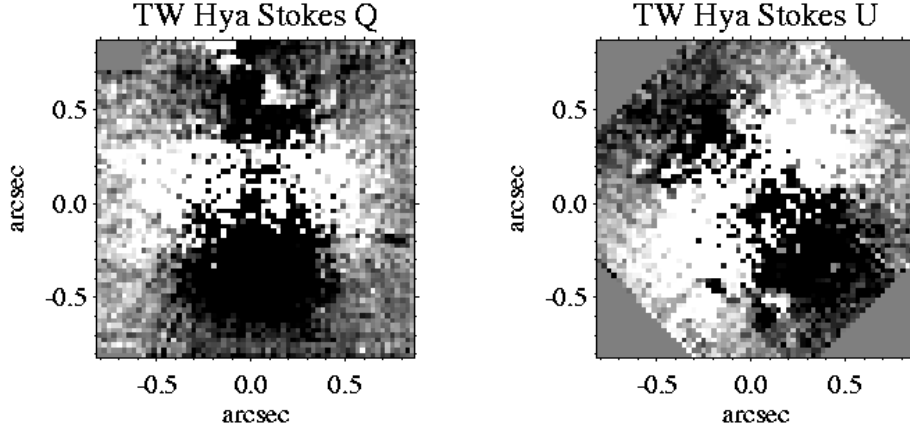


Figure 3.7: Stokes Q and U measurements of TW Hya as obtained with NACO at the VLT (Apai et al. 2004). The polarisation pattern from this extended, almost face-on circumstellar disk is clearly visible and can be traced close to the central star.

With the Stokes vectors obtained at all four polarisation angles the instrumental polarisation can be corrected:

$$Q = \frac{Q' - Q''}{2} \quad (3.5a)$$

$$U = \frac{U' - U''}{2} . \quad (3.5b)$$

Thereof the polarised intensity is obtained:

$$PI = \sqrt{\frac{Q^2 + U^2}{2}} . \quad (3.6)$$

During the subtraction of the ordinary and extra-ordinary beam (cf. Eqs. 3.4a – 3.4d), both images must be centered with sub-pixel accuracy relative to each other to avoid any artificial polarimetric features. The same applies for the simple co-addition of exposures taken at different detector positions during a jittering sequence. Since the separation of the ordinary and extra-ordinary beam shows a chromatic behaviour, their exact centering becomes difficult if broadband filters are used. In Sect. 3.3.2 we explain how these problems were solved for our data.

Finally, it must be noted that Polarimetric Differential Imaging still is away from being completely understood. Applications of this method to a larger sample of circumstellar disks have just begun. It is therefore a priori still not clear which disks will show a prominent polarisation feature (cf. Sect. 3.3.4).

3.3.2 Observation and data reduction

Selected targets

HD 113766 and MP Mus (alias PDS 66) were selected due to promising discoveries at mid-IR wavelengths (cf. Sects. 4.3 and 4.4), where we found previously unknown disks. Kalas et al. (2004) recently detected a disk around the 9.9 pc close star AU Mic (alias HD 197481, alias GJ 803) using coronagraphy in the R-band, which we intended to confirm. HD 149914 shows both a strong far-IR excess as well as a polarisation of more than 2.54% already at visual wavelengths (Bhatt & Manoj 2000). A circumstellar disk is thus likely, however, the nature of HD 149914 is still not clear: Malfait et al. (1998a) considered it as a Vega-like star, but most authors quote it now as a Herbig Ae star in agreement with the age of 0.5 - 1 Myr given by Habart et al. (2003).

Observation

The observations with NACO at Paranal were carried out during two nights at the begin of May 2004. Because of the chromatic behaviour in the Wollaston's beam separation and as our sources are quite bright, we performed the data acquisition with the narrow band (NB) resp. intermediate band (IB) filters NB 1.64, IB 2.06 and NB 2.12 (the number specifies the wavelength in micron). For the brightest target, AU Mic, the neutral density filter ND_{short} had to be used in addition, which blocks a wavelength-independent fraction of the source flux. The pixel sampling is 0''.013/pixel in all images. Details of the targets are shown in Table 3.4 together with the integration times and the atmospheric seeing. Unpolarised standard stars were observed for comparison.

A problem of the PDI method is the relatively low S/N-ratio. Since the signal is separated into the ordinary / extra-ordinary beam and since each observation must be repeated at all four polarisation angles, this would require eight times more observing time than standard imaging to reach a comparable S/N. It is therefore common in PDI observations to saturate the central region close to the star to keep the observing time reasonable. Here, we only saturated very moderately at the central pixel, as a goal of the observations was to trace the disk very close towards the star.

The requested jittering offsets, sent to the telescope control, can not be used to co-add a jittering data sequence. Due to the required sub-pixel accuracy the real offsets have to be determined from the acquired data. The alignment gets even more difficult with saturations in the signal peak. Therefore, at each detector position and before moving to the next jitter position, a short-time exposure was made followed subsequently by the long-time integration. Jittering offsets are later deduced from the short-time exposures and applied to co-add the long-time integrations.

Due to the special procedure in this data acquisition, the available Observing Blocks to control the telescope could not be used and the telescope instead was operated interactively.

Table 3.4: Targets observed with NACO polarimetric differential imaging. The spectral types and V-band magnitudes are taken from SIMBAD – unless the cited papers provide more accurate information. K-band magnitudes were measured by 2MASS. **Stellar ages** are from (1) Meyer et al. (2001, estimation from evolutionary tracks), (2) Habart et al. (2003, comparison with evolutionary tracks), (3) Zuckerman et al. (2001) estimate 8 Myr while Barrado y Navascués et al. (1999, isochrone fitting) determine 20 Myr, (4) Mamajek et al. (2002, spectral characteristics and isochrones). **The distances** are given by (5) Meyer et al. (2001), (6) Habart et al. (2003), (7) Perryman et al. (1997), (8) Mamajek et al. (2002). The integration time for each filter lists the time per polarisation angle.

Object	Spectral Type	V [mag]	K [mag]	Age [Myr]	Ref.	d [pc]	Ref.	t (NB 1.64) [s]	t (IB 2.06) [s]	t (NB 2.12) [s]	Seeing [$''$]
HD 113766	F3/F5 V	7.56	6.49	10 – 20	(1)	130	(5)	600	–	–	0.7 – 0.8
HD 149914	B9.5 IV	6.75	5.69	0.5 – 1	(2)	165	(6)	720	–	480	0.5 – 0.6
AU Mic	M1 Ve	8.81	4.53	8 – 20	(3)	9.9	(7)	720	792	–	0.4 – 0.8
MP Mus	K1 IV	10.32	7.29	8	(4)	86	(8)	480	480	–	0.7 – 1.7

Data reduction

Basic data reduction: All individual frames were inspected for unexpected features (irregular electrical noise, read-out errors, etc.). With the ESO ECLIPSE package⁵ we performed the dark, flatfield and sky corrections.

Image co-addition was achieved with the program *Jitter*, which is part of the ECLIPSE package. As sub-pixel accuracy is required to co-add the polarimetric images, we first determined from the short-time exposures the accurate jittering offsets and consecutively applied these to co-add the long-time exposures. We are not sure whether we should recommend ECLIPSE's *Jitter* routine for *polarimetric* data, since due to an internal numerical problem in the software (only affecting polarimetry data) the co-addition of some frames occasionally fails. On the other side, in most cases the affected frames were just those where Strehl ratio variations had occurred, and these images should not be co-added anyway.

The **Stokes vectors** were determined using an IDL routine which subtracts with sub-pixel accuracy the ordinary and extra-ordinary beam of the final, co-added image.

3.3.3 Results

Detector artefacts

For completeness, we summarise some detector artefacts of which none was critical.

- Two ghosts caused by the ND_short filter: Even under low illumination levels all data acquired with the neutral density filter ND_short show a ghost at a distance $d = 1.3''$ from the source at position angle $\text{posang} = 51^\circ$ (measured from North via East for 0° polarisation angle). Interestingly, for AU Mic this ghost appears in the same distance where a possible planetary companion is suspected (Liu et al. 2004). By turning the instrument this becomes recognisable as artefact. A less prominent ghost is seen at $\text{posang} = 166^\circ$ and $d = 6.5''$.
- Any moderate saturation creates 6 further ghosts, five of these are dependent from the source position on the detector.
- Even moderate saturation can leave remanence effects on the detector.

Problems induced by the AO correction

- **Waffle pattern:** Under special atmospheric conditions – not necessarily only during bad seeing – NAOS fails to produce a clean PSF. Instead, the AO correction creates a PSF consisting of five point sources (the real one being closely

⁵<http://www.eso.org/eclipse>

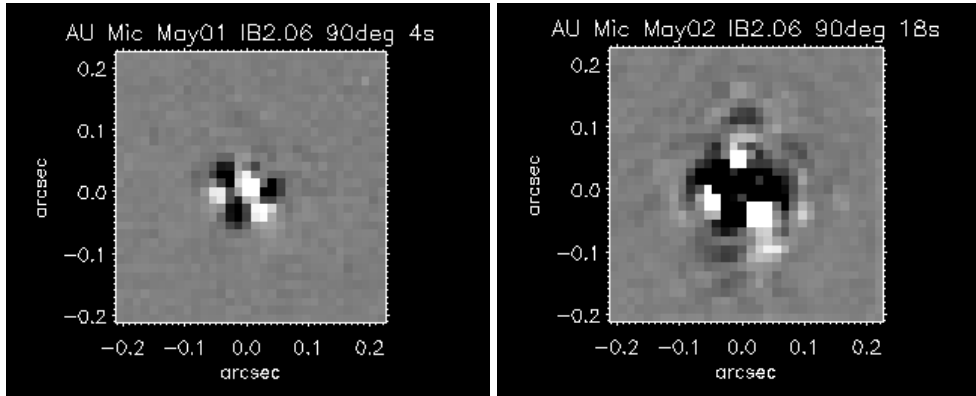


Figure 3.8: Two examples of the NACO 'triangle effect' with different exposure times (4s resp. 18s, cf. image headers).

surrounded by four copies in the form of a square) and 'corrects' the science targets in this respect. The impact of this feature on the final image quality is not comprehensively known and may depend on the targets' intrinsic polarisation. In our data no persisting artefacts remained.

- **Triangle effect:** At the distance of the first Airy ring around a source, the light is enhanced at three positions forming a triangle. This pattern does not change with a rotation of the CONICA camera and is known as a fairly stable feature. It likely originates from an artefact created by NAOS due to a false correction of the triangular coma, which is a higher order wavefront distortion in Adaptive Optics. Possibly, this order of distortion is overcorrected by NAOS, although the actual origin of this feature is not yet firmly known. The triangle effect persists after image processing and constitutes in our data a dominant signal (cf. Fig. 3.8), also because of the non-detection of real polarised emission from the stars.

Stokes vectors

No clear polarisation pattern is seen in the Stokes images for any target. The observed features remain also unchanged with varying polarisation angle and no difference is recognised between the targets and the unpolarised standard stars. The 'triangle effect' and variations thereof (changing with the quality of the AO correction) is the only feature seen.

3.3.4 Discussion

As the PDI method was proven to work for HD 169142 (Kuhn et al. 2001) and TW Hya (Apai et al. 2004) we discuss possible reasons for our non-detection:

Since there is no coronagraphic mask for the NACO polarimetry mode, the stellar brightness certainly limits the maximum integration time in each individual exposure (detector integration time, DIT) and thus also limits the disk detection sensitivity. All our targets are brighter in the K-band than TW Hya, besides MP Mus which has a similar magnitude. Adjusting the number of co-added images consequently, would result in unreasonably long observing times. The sensitivity can alternatively be increased by saturating the detector around the position of the star. However, a massive saturation is not permitted at Paranal and was neither our goal, as we intended to trace the emission relatively close towards the star. A new detector with a much better dynamical range, which would facilitate this kind of observation, has been installed into CONICA *after* our observing run.

On the other side, the disks around TW Hya (age = 8 Myr, Webb et al. 1999) and HD 169142 (with likely an even younger age) may be regarded as a most favourable case, given their ages and especially their face-on projection. It must also be stated that Kuhn et al. (2001) from a sample of 10 promising targets only detected a disk around HD 169142. Unfortunately, they do not mention their non-detections.

Huélamo et al. (personal communication) recently observed with PDI eleven sources in the TW Hya and ρ Oph association, consisting of known disks (HR 4796, HD 98800, TW Hya) and disk candidate objects. They detected three objects thereof and conclude that **PDI never works for sources without a prominent near-IR excess**. If an excess exists, the detectability of polarimetric features still depends on physical parameters yet to be determined, however, a very young age of the source (possibly within the pre-main sequence) seems to be an important factor. It would be interesting to study whether there is a direct correlation of disk detectability with the stellar ages or the amount of near-IR excess. However, final results of the above cited work were not yet available at the time of writing this section. Within our target sample MP Mus and HD 149914 show a near-IR excess, while it is absent for AU Mic and HD 113766. No difference in our data is seen whether or not the source has an excess, also because our data have not sufficient sensitivity. Finally, it should not be forgotten that the disks around TW Hya and HD 169142 are both seen face-on.

Chapter 4

Mid-infrared observations

4.1 Technical introduction

4.1.1 Observing in the mid-infrared

At mid-IR wavelengths (about 5 - 30 μm) the emission from the sky background is strong and can rapidly vary with the ambient conditions, especially with the humidity and temperature. Thus, chopping and nodding becomes necessary to perform the observations.

Chopping is done by small displacements of the telescope's secondary mirror (M2) at frequencies between 0.5 and 10 Hz: the telescope beam then is alternatively pointing at the astronomical target and the sky background. A typical chopping throw is about 10 - 40'', while the maximal possible throw with TIMMI2 is 100''. A subtraction of the images from the respective telescope beams eliminates the sky background emission. For most mid-IR cameras both the selection of the chopping frequency and the subtraction of the corresponding beams is automatically processed. A small chopping throw ($\sim 10''$) is generally recommended for point sources, while for an extended target a throw should be selected that avoids overlapping of the source in both beams.

An essential part of this technique is to combine the chopping with telescope *nodding*: the chopped images still contain a constant thermal emission from the telescope and the dome. With an additional telescope offset during the observing sequence this can be completely eliminated. The telescope performs offsets in the direction perpendicular or parallel to that of the chop, while the resulting images from both nod positions (already being chop-subtracted by the camera pre-processor) are later subtracted as well. During this procedure also residuals of the chopping correction are eliminated, which were caused by different optical paths in the two chopping beams. A nodding throw is typically 10 - 30''. Two methods exist to align chopping with the nodding offsets:

- Triangular chopping, i.e. nodding along the chopping direction. In this case the nod throw must have exactly the same value as for the chop and must be set opposite to the chopping direction (cf. Fig. 4.1).

Imaging and Spectroscopy

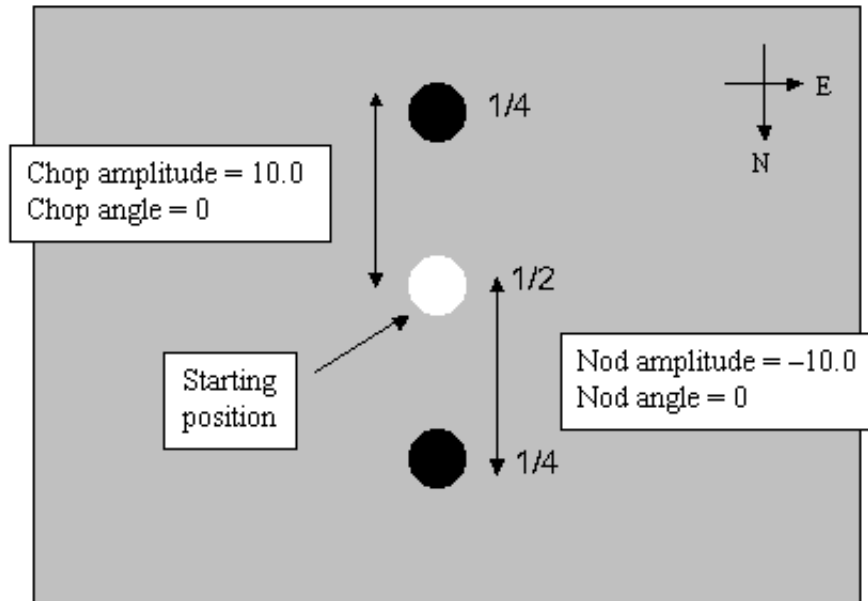


Figure 4.1: The triangular chopping-nodding combination: the nod amplitude is the same as for the chop, but the telescope is nodding opposite to the chopping direction. After combining the corresponding images, the positive signal in the mid (*white*) contains half of the total source flux, while each top/bottom negative image (*black*) contains a quarter of the flux. To estimate the total photometry, one needs to measure all three source positions. (Image credit: La Silla Observatory)

- A quadratic pattern of the source, i.e. the nodding is perpendicular to the chopping direction (cf. Fig. 4.2).

The triangular chop-nod combination is mandatory for spectroscopic observations and recommended for faint imaging exposures as well. Currently, for *imaging* with TIMMI2 this setup is discouraged, since with the faster M2 chopping frequency – introduced during the TIMMI2 upgrade in October 2002 – the alignment of the two positive beams into the middle signal does not work well for all settings. Spectroscopy is not a problem due to the lower M2 chopping frequency in this mode.

4.1.2 The TIMMI2 camera

The Thermal Infrared Multi-Mode Instrument (TIMMI2) covers the 3.5 - 24 μm wavelength range. Available observing modes are summarised in Table 4.1 and include imaging, spectroscopy and polarimetry in both cases. The 320×240 pixel Raytheon

Small Source Imaging

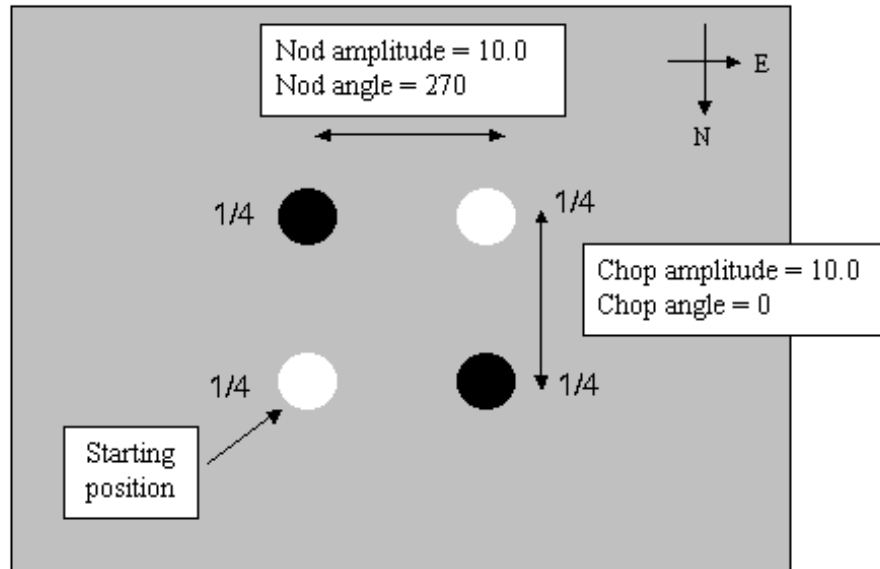


Figure 4.2: Quadratic chopping-nodding pattern. The nodding is perpendicular to the chopping direction. After data processing, each of the positive and negative images contains a quarter of the source flux. (Image credit: La Silla Observatory)

detector is sensitive between 2 - 28 μm . For details about filters, sensitivities and ongoing projects we refer to the TIMMI2 webpage¹.

The following gratings and slits are available for spectroscopy:

- Low-resolution grism (0.02 $\mu\text{m}/\text{pixel}$, $\lambda/\delta\lambda = 160$) covering the wavelength range 7.5 - 13.9 μm .
- Low-resolution grism (0.03 $\mu\text{m}/\text{pixel}$, $\lambda/\delta\lambda = 130$) covering the wavelength range 14.5 - 23.9 μm .
- 3'' \times 70'' long-slit
- 1.2'' \times 70'' long-slit

The acquisition of a source brighter than ~ 0.5 Jy can be started directly. For faint objects, especially in case of spectroscopy, it is required to take first a short-time image to determine the exact position of the target on the detector. Once the source is detected, it can be centered into the slit using telescope offsets.

A limit exists for extremely bright objects: any target brighter than ~ 1000 Jy will produce strong residual artefacts on the detector around the source's position. However, such strong emitters are rare and quite uncommon as science targets.

¹<http://www.la.silla.eso.org/lasilla/sciops/3p6/timmi/>

Table 4.1: Available imaging and spectroscopy modes with the corresponding fields of view.

Mode	Nominal scale	Full field of view
L-band imaging	0'3 / pixel	100 x 76 arcsec ²
M-band imaging	0'3 / pixel	100 x 76 arcsec ²
N-band imaging	0'2 / pixel	64 x 48 arcsec ²
N-band imaging	0'3 / pixel	96 x 72 arcsec ²
Q-band imaging	0'2 / pixel	64 x 48 arcsec ²
N-band spectro	0'45 / pixel	
Q-band spectro	0'6 / pixel	

The instrument, detector and telescope are controlled by Observing Blocks (OBs), which are scripts based on the Tcl language. The observer prepares these prior to the run via a graphical interface called P2PP².

4.1.3 The reduction pipeline for TIMMI2

The following parameters define the readout of the TIMMI2 detector:

1. DIT: detector integration time. This is a short single exposure time. Due to the bright sky emission in the mid-IR, typical values of a DIT are around some dozens ms.
2. NCREAD: number of reads during one half chopping cycle. This is similar (but not identical) to the NDIT parameter of other ESO instruments.
3. NCDUMMY: as the chopper needs to stabilise at the beginning of each exposure, a number of DITs are discarded. These are called 'dummy reads'.
4. NCYCLE: the number of chopping cycles.

Above read parameters are not user defined. They are internally set to optimal values to avoid unreasonably large overheads and background saturation (assuming average weather conditions, i.e. no clouds).

Pre-processing

To readout the TIMMI2 detector and for data pre-processing, the ESO IRACE acquisition system is used. It co-adds the individual DITs and builds a difference image from the chopping half cycles. Several chop cycle images are then averaged to a single frame delivered as a FITS file – called video frame. The number of counts therein is normalised to a DIT (but the information about the integration time is preserved).

Hence, the total elapsed time for one video frame amounts to

²<http://www.eso.org/observing/p2pp/P2PP-tool.html>

$$T_{\text{elapsed}} = 2 * \text{DIT} * (\text{NCREAD} + \text{NCDUMMY}) * \text{NCYCLE}, \quad (4.1)$$

while the effective exposure time is

$$T_{\text{exposure}} = 2 * \text{DIT} * \text{NCREAD} * \text{NCYCLE}. \quad (4.2)$$

On-line pipeline

The number of video frames (NVIDEO) per nod position depends on the observing mode and the time spent on each nodding position (the latter one is a parameter defined by the user). During average weather conditions not more than three minutes should be spent on the same nodding position because of variations in the sky. The number of nodding cycles (each consisting of two nod positions) may be increased arbitrarily, according to the total integration time the observer desires.

An on-line pipeline, written in MIDAS³, co-adds all incoming FITS files (i.e. the video frames) and applies the subtraction of corresponding nod positions. Each observing sequence thus results in a final processed FITS frame. The signal therein is co-averaged and corresponds to a DIT. A photometric analysis, however, must consider the total integration time, which is

$$T_{\text{integrated}} = 2 * \text{DIT} * \text{NCREAD} * \text{NCYCLE} * \text{NVIDEO}. \quad (4.3)$$

The required variables in Eq. (4.3) can be obtained from the keywords in the FITS header. No explicit bad pixel correction is performed by the pipeline, but the nodding correction is quite efficient in reducing artefacts and residues. See Appendix A for a discussion on the flatfielding of mid-IR data. As for all ESO instruments, the pipeline can not (yet) co-add polarimetric data, due to their higher complexity. Despite of the high quality of the TIMMI2 pipeline, users may want to repeat the co-adding of the observing data prior to a scientific analysis. Especially for fast-moving targets, like comets or asteroids, this is recommended.

4.1.4 Calibration of mid-IR data

The most prominent features in IR spectra are the telluric lines. Many of these do not scale linearly with airmass, thus it is necessary to observe a standard at the same airmass and with the identical instrument set-up as used for the science target. Furthermore, the strength of a telluric line can change with time, as the atmospheric absorption in the mid-IR varies with the water vapour's column density and the airmass. Therefore it is also necessary to observe the standard star close in time to the science target. On an average La Silla night, mid-IR standard stars should be observed each 2-3 hours.

³<http://www.eso.org/midas>

The spectrum of the telluric standard is divided directly into that of the science target. Ideally, the spectrum of the telluric standard should be known, so that features intrinsic to it can be removed. Stars of spectral type M (and later) are not suited because of their spectral peculiarities. Information about appropriate standard stars for the mid-IR, compiled from the ISO list of standards, is provided at the TIMMI2 webpage together with synthetic model spectra⁴.

For absolute flux calibration, slit losses have to be estimated, e.g. by taking the photometry in a narrow band filter and comparing this to the spectral flux folded with a corresponding filter function. However, at 10 μm the image quality is diffraction limited with TIMMI2 at the 3.6 m telescope ($\sim 0''.7$) for seeing in the visual below 1.5'' (note that the seeing decreases as a function of wavelength). Slit losses, even with the 1.2'' slit, are thus negligible under average La Silla conditions.

4.2 Correcting the chromatic and airmass dependent extinction for TIMMI2 spectra

We present a method to correct the chromatic and airmass dependent extinction for N-band spectra taken with the TIMMI2 instrument at the ESO/La Silla observatory. Usually, the target and calibrator star have to be observed at similar airmass in order to obtain reliable spectrophotometric fluxes. Our method allows to correct the atmospheric extinction and substantially improves the spectrophotometric flux calibration, when the standard stars were observed at a very different airmass than the targets. Hundreds of standard star measurements in several passbands (N1, N8.9, N10.4, N11.9) were used to derive mid-IR extinction coefficients. We demonstrate that applying our correction of the differential extinction to test data results in a spectrophotometric accuracy up to 2% within the literature flux.

4.2.1 The influence of atmospheric extinction in the mid-IR

For spectroscopy a target star and its corresponding calibrator should generally be observed at a comparable airmass to avoid a varying extinction between the two objects. Different to near-IR observations, in the mid-IR a good calibrator at the same airmass is often difficult to find and the theoretical behaviour of the extinction with airmass and wavelength is not really known up to now. Some authors claimed there would be no clear dependence and thus for photometry no airmass correction needs to be applied. However these authors used dozens of standard star observations, while we apply several hundred measurements.

In mid-IR spectroscopy the influence of extinction is more evident than for photometry. No good spectral flux calibrations are possible unless the target and calibrator star are observed close in time and very close in airmass (≤ 0.1 airmass distance). Therefore,

⁴<http://www.ls.eso.org/lasilla/sciops/3p6/timmi/html/stand.html>

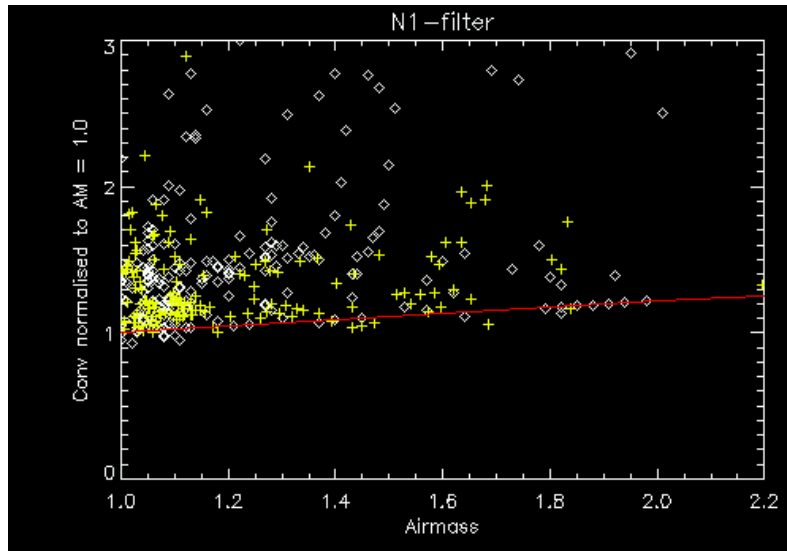


Figure 4.3: Conversion factors as a function of airmass are displayed for the N1 passband. White squares are standard star measurements obtained since the TIMMI2 upgrade in October 2002, yellow crosses symbolise data taken before this time. Especially watch the well defined rise of points between AM = 1.8 and AM = 2. The red line represents the fit from which Eq. (4.4a) is derived.

some observers often use additional photometric measurements to correct the spectral fluxes. Since the extinction as a function of wavelength varies significantly within the N-band, also the spectral slope needs to be corrected, if the target and calibrator had been taken at different airmass.

Our goal is to explain the extinction in the mid-IR as a function of airmass. We further demonstrate that the extinction has a non-linear wavelength dependence in the N-band.

4.2.2 Data analysis

All observations of standard stars obtained with TIMMI2 are archived from the beginning of operations in 2001 until present. The conversion factors between measured counts and known fluxes depend on the filter and lens scale used as well as the airmass (all systematically), but also vary with the sky conditions (statistically). A decreasing count rate as a function of rising airmass corresponds to an increasing conversion factor towards larger airmass.

We first separate all standard star measurements according to the filter and lens scale used. Data obtained before the TIMMI2 upgrade in October 2002 are treated separately because of different electronical gains in the previous readout system, but after a normalisation with the conversion factor for airmass AM = 1.0 both results are comparable.

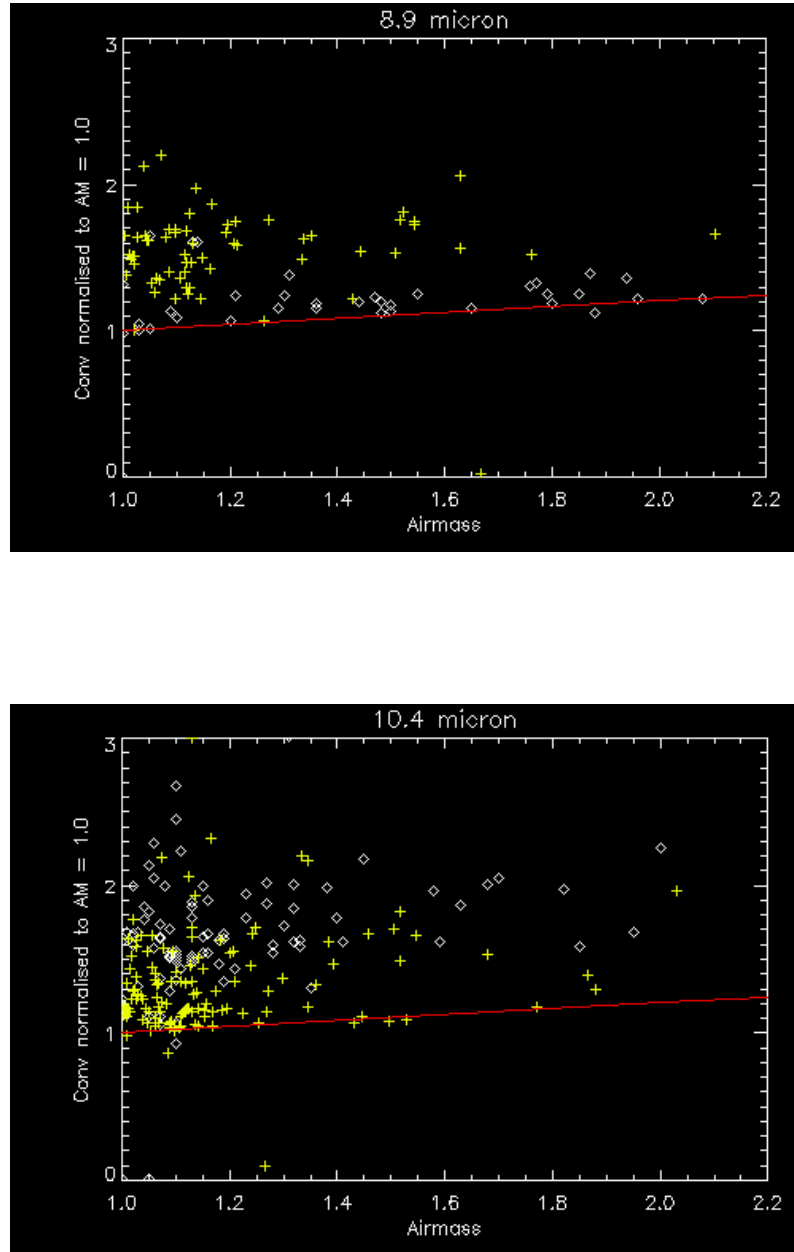


Figure 4.4: Conversion factors as a function of airmass for the N8.9 and N10.4 filters. See Fig. 4.3 for further information.

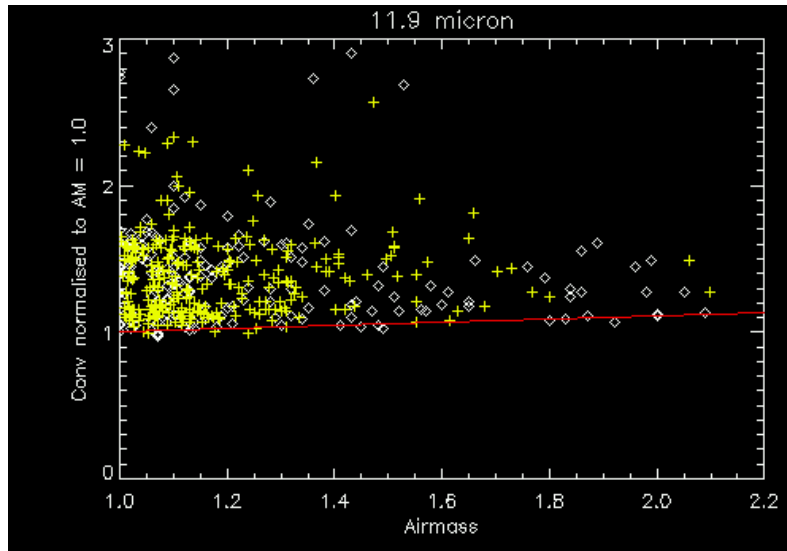


Figure 4.5: Conversion factors as a function of airmass for the N11.9 passband.

In Figs. 4.3 - 4.5 we show for several N-band filters the conversion factors (hereafter called Conv) as a function of airmass. Note that in all plots a clear trend for Conv increasing with airmass can be seen, especially if you look towards the lower margin of the distribution.

Why can we constrain our analyse to the lower margin ? For a given detector and instrument configuration there exists a well defined optimal sensitivity for a star, i.e. the least extinguished count rate achieved for best weather conditions. This corresponds to a minimum in the conversion factor. On the other side, the sensitivity deteriorates arbitrarily with worse sky conditions and there is no clear maximum for the conversion factor. This is the reason why the distribution of points in Figs. 4.3 - 4.5 seems to be confined in lower y-direction but spreads towards higher y.

Since we need measurements obtained under identical weather conditions, it is sufficient to make a fit only with the lower-value points. We normalise for each filter the conversion factors by the value for $AM = 1.0$, in order to make comparable the measurements obtained before and after the TIMMI2 upgrade as well as to make these results comparable to other instruments.

4.2.3 Results

Differential extinction as function of airmass

We present relations, deduced as explained in the previous subsection, which describe the dependence of the atmospheric extinction with airmass (AM). Equation (4.4a), for example, signifies that at this wavelength the (spectral) flux must be corrected by 22%

to account for the extinction between $AM = 1.0$ and $AM = 2.0$. For mid-IR filters not given below the number of standard star measurements was not sufficient to calculate a firm result. Since the TIMMI2 archival of standard stars is an ongoing effort, we can add results for these passbands at a later stage.

In Eqs. (4.4a - 4.4d) AM represents the airmass of observation and $Corr$ is the factor to correct the targets' flux into measurements at airmass 1.0. Note that the TIMMI2 filters are not always named according to their central wavelength λ_0 .

$$N1 (\lambda_0 = 8.6 \mu\text{m}) : \quad Corr(AM) = 1 + 0.220 * (AM - 1) \quad (4.4a)$$

$$N8.9 (\lambda_0 = 8.7 \mu\text{m}) : \quad Corr(AM) = 1 + 0.208 * (AM - 1) \quad (4.4b)$$

$$N10.4 (\lambda_0 = 10.3 \mu\text{m}) : \quad Corr(AM) = 1 + 0.212 * (AM - 1) \quad (4.4c)$$

$$N11.9 (\lambda_0 = 11.6 \mu\text{m}) : \quad Corr(AM) = 1 + 0.116 * (AM - 1) \quad (4.4d)$$

For spectroscopy, both the target and calibrator must be flux corrected before their division. Therefore the wavelength dependence of $Corr$ has to be taken into account. In a first approach, we use a linear interpolation between $Corr$ for N1 and N11.9, since most observations and therefore the best fits are achieved in these passbands. Due to their lower statistical weight, $Corr$ for N8.9 and N10.4 will be considered in a near future when the TIMMI2 database contains more observations for these filters. The good results shown in Table 4.3, Table 4.4 and Fig. 4.6 justify this first approach a posteriori.

$$Corr(\lambda, AM) = 1 + [0.220 - (0.220 - 0.116)/3 * (\lambda - 8.6 \mu\text{m})] * (AM - 1) \quad (4.5)$$

The factor '3' in Eq. (4.5) expresses the difference in wavelength between N1 and N11.9. Finally, $Corr(\lambda, AM)$ is multiplied with the uncorrected spectral flux $F(\lambda, AM)$:

$$F_{\text{real}}(\lambda) = F(\lambda, AM) * Corr(\lambda, AM) \quad (4.6)$$

In any data reduction script which also extracts the airmass from the file headers, Eqs. (4.5) and (4.6) can be conveniently included. With this approximation already a significant improvement of the spectral fluxes is seen in Fig. 4.6, especially for large distances in airmass. At a later stage, when we can include further correction factors for other N-band filters, the flux correction can be improved to an even higher perfection.

N-band extinction coefficients

From the relative increase of atmospheric extinction between $AM = 1.0$ and $AM = 2.0$ we can, in principle, calculate the extinction coefficients K for La Silla (usually given in mag/AM). These values depend on the observatory site, especially on the altitude and climatic conditions.

Table 4.2: Median N-band extinction coefficients for La Silla.

Filter	K [mag/AM]
N1	0.22
N8.9	0.21
N10.4	0.21
N11.9	0.12

Table 4.2 summarises the median N-band extinction coefficients. Thereof an unextincted photometry with magnitudes m_{real} can be obtained via the relation

$$m_{\text{obs}}(\text{AM}) = m_{\text{real}} + K * \text{AM}. \quad (4.7)$$

The wavelength dependence of our extinction coefficients shows some similarity to data for Mauna Kea, while the absolute values differ because of the other altitude.

4.2.4 Application to spectroscopic data

Equations (4.5) and (4.6) were tested with a cross-calibration of different standard stars taken from the same night. We used test data obtained both in December 2002 and September 2003. A calibrator at low airmass is taken while the objects were observed at higher airmass (see the headers of Fig. 4.6 for the actual airmass value).

Spectra shown in Fig. 4.6 were obtained in December 2002 when the detector had a dead column between approximately 9.0 μm and 9.8 μm . By intention we did not correct spectral line features in order to show how these may develop with increasing airmass between target and calibrator. Look especially to the CO_2 absorption features at 11.73 μm and 12.55 μm .

Further we derive spectrophotometric fluxes for the N11.9 filter and compare these with literature values. As shown in Tables 4.3 and 4.4 our airmass correction improves the flux calibration both for targets observed at low and high airmass and reaches an accuracy up to 2% within the literature flux.

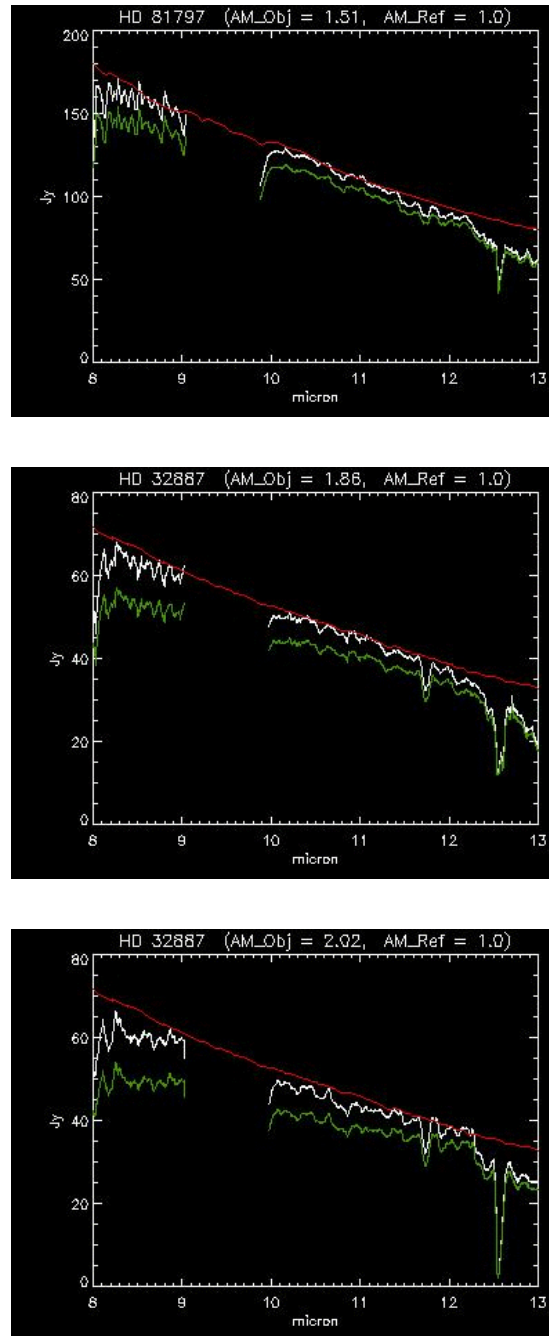


Figure 4.6: Illustrations of our airmass correction using a calibrator at airmass $AM = 1.0$ and targets up to $AM = 2.0$. The flux-calibrated target spectrum is shown without airmass correction (*green profile*) and corrected (*white curve*). A literature profile is overplotted (*red*). The quality of this airmass correction may be even further improved, when we can also apply correction factors from the other N-band filters.

Table 4.3: Test of the airmass correction (AMC) with data taken on December 15th, 2002. The spectrophotometry in the N11.9 filter is shown with and without our airmass correction (AMC) for target and calibrator stars at varying airmass.

Object	AM(obj)	F(11.9 μm) [Jy]	Calibrator	AM(cal)	no AMC [Jy]	with AMC [Jy]
HD 32887	1.03	41.50	HD 81797	1.51	45.58	43.14
			HD 32887	1.86	47.82	43.59
			HD 32887	2.02	48.46	43.43
HD 32887	2.02	41.50	HD 32887	1.03	35.67	39.79
			HD 81797	1.44	37.63	40.09
			HD 81797	1.51	39.09	41.27
			HD 32887	1.86	41.02	41.71

Table 4.4: Test of the airmass correction (AMC) with data obtained on September 13th, 2003.

Object	AM(obj)	F(11.9 μm) [Jy]	Calibrator	AM(cal)	no AMC [Jy]	with AMC [Jy]
HD 187642	1.27	24.28	HD 4128	1.52	25.03	24.35
			HD 169916	1.85	26.26	24.76
HD 169916	1.85	22.35	HD 187642	1.27	20.64	21.89
			HD 196171	1.28	20.74	21.96
			HD 4128	1.52	21.31	21.98

4.3 Disks around pre-main sequence stars

We present new N-band photometry and spectroscopy for a sample of eight pre-main sequence stars including T Tauri, Herbig Ae/Be stars and FU Ori objects using the ESO TIMMI2 camera at the La Silla observatory (Chile). For some objects this is their first N-band spectroscopic observation ever. The FU Ori stars V 346 Nor, V 883 Ori and Z CMa show a broad absorption band which we attribute to silicates, while for BBW 76 we find silicate emission. A comparison with ISO-SWS spectra of V 346 Nor and Z CMa taken in 1996/1997 reveals no differences in spectral shape. All T Tauri and Herbig Ae/Be stars possess N-band emission features. We model the emission spectra with a mixture of silicates consisting of different grain sizes and composition. The Herbig Ae star HD 34282 shows strong features of PAHs but none of silicate, while the emission spectrum of the Herbig Ae star HD 72106 resembles those of solar-system comets and known Herbig sources of evolved dust. We demonstrate that HD 72106 is host to highly processed silicates and find evidence for enstatite, which is not common in young objects. Evolved dust is also seen in the T Tauri stars HD 98800 and MP Mus. We further detected MP Mus at 1200 μm with the bolometer array SIMBA at the SEST in La Silla. The findings of our analysis are given in the context of previous dust studies of young stellar objects.

4.3.1 Introduction

Near-IR studies of circumstellar (CS) disks measure the scattered light from dust in the inner disk region, which may strongly depend on the disk structure. At longer wavelengths dust dominates the emission. However, imaging disk searches in the mid-IR are difficult with current ground-based instruments due to limited sensitivity and spatial resolution. The existence of CS matter can more easily, although indirectly, be revealed with photometry and spectroscopy.

In this section we present a search and analysis of CS matter for a sample of pre-main sequence objects whose IR appearances have not yet been well characterised in the literature. Our goal is to obtain insight into the dust properties by modelling the N-band silicate features, and to compare the result with those of other sources.

Cohen & Witteborn (1985) performed 10 μm spectrophotometry of 32 T Tauri or related young stars and concluded that the CS matter has a disk-like geometry. N-band spectroscopy of 23 young stars was shown by Hanner et al. (1998); their sample includes four members of the FU Ori class (FUOR). A new way of modelling the silicate dust features was presented by Bouwman et al. (2001, henceforth B2001) for a sample of 14 Herbig Ae/Be stars (HAeBe). This technique was also used by Meeus et al. (2003) for a group of three T Tauri stars (TTS). In both cases large differences in the amount of dust processing were found in an otherwise fairly homogeneous sample. A correlation between the strength of the silicate feature and its shape, which is interpreted as evidence of grain processing in CS disks, was found by van Boekel et al. (2003). Przygodda et al. (2003) performed a similar analysis for 14 T Tauri stars and found the same correlation. Meeus et al. (2001, henceforth M2001) analysed 2 - 45 μm

ISO-SWS spectra and spectral energy distributions of 14 HAeBes and explained their differences in terms of a different disk geometry. Acke & van den Ancker (2004b) extended this sample, investigating ISO-SWS spectra of 46 HAeBe stars in total. As well as an analysis of the silicate bands around 10 μm , they focus on the PAH emission and relate its presence to the disk geometry of the objects.

Half of our targets are FU Ori objects. This is a class of low-mass pre-main sequence stars, whose variability is characterised by a dramatic outburst in optical light followed by a fading phase which lasts decades. The origin of this phenomenon is not clear but it is often associated with enhanced accretion (Hartmann & Kenyon 1996). Herbig et al. (2003), however, proposed a very different interpretation. Recently, the effect of these optical outbursts upon the object's appearance in the infrared has been investigated (Andrews et al. 2004, Ábrahám et al. 2004).

The structure of this section is as follows: in Sect. 4.3.2 we introduce our targets and in Sect. 4.3.3 we describe the observations and data reduction. Modelling and analysis of the N-band spectra are presented in Sect. 4.3.4. We discuss the dust composition of the individual targets in Sect. 4.3.5 and finish with a summary and conclusions in Sect. 4.3.6. In Sect. 4.4 a different sample of older stars is analysed in a similar way, consisting of Vega-type and post-main sequence targets.

4.3.2 Observed sources

Our targets are heterogeneous in spectral type and fraction of IR excess, but all objects are still on the pre-main sequence. The sample includes four FU Ori, two T Tauri and two Herbig Ae stars. Their stellar parameters and both IRAS and mm fluxes are given in Table 4.5. We note that for many of our targets - besides IRAS photometry - this is their first observation in the mid-IR. For those cases where more mid-IR data have already been published we give references. In the following, the sources are described individually:

- The Herbig Ae star **HD 34282** was shown by Sylvester et al. (1996) to have a strong infrared excess towards far-IR wavelengths. Mannings & Sargent (2000) obtained unresolved mm-measurements with the Owens Valley Radio Observatory. A large, massive Keplerian disk ($R_{\text{out}} = 835 \pm 20$ AU) was confirmed by Piétu et al. (2003) using the IRAM Plateau de Bure Interferometer. They also point out that the Hipparcos distance to HD 34282 has been underestimated. N-band spectra were published in Sylvester & Mannings (2000) and Acke & van den Ancker (2004b), but their quality is not sufficient to allow a detailed dust analysis.
- Not much is known about **HD 72106**. It is a binary with $0''.78$ separation (Fabricius & Makarov 2000). Optical spectroscopy characterised its southern component as a HAeBe candidate (Vieira et al. 2003).
- **HD 98800** (alias TWA 4) represents a visual binary with $0''.8$ projected separation, whose components each consist of a spectroscopic binary. Gehrz et al. (1999) showed that the large mid-infrared excess is entirely associated with the

Table 4.5: Stellar parameters and known fluxes for our target sample. V-band magnitudes and the IRAS 12 μm fluxes (except for V 346 Nor) are taken from the SIMBAD database. T_{adopted} and $(\log g)_{\text{adopted}}$ list the temperature and gravity which we used to select the appropriate Kurucz atmosphere model for the HAeBe and T Tauri stars (for completeness these values are also shown for the FUOR sources). **The mm-fluxes** have been measured by (1) Piétu et al. (2003), (2) Stern et al. (1994), (3) This work (at 1200 μm), (4) Reipurth et al. (1993) and (5) Sandell & Weintraub (2001, given as flux/beam). **Stellar ages:** (6) From Fig. 4 in Piétu et al. (2003) we roughly estimate the given age. Other values were determined by (7) Prato et al. (2001, PMS evolutionary tracks), (8) Mamajek et al. (2002, spectral characteristics and isochrones), (9) Van den Ancker et al. (2004, comparison with PMS evolutionary tracks). **The distances** are from (10) Piétu et al. (2003), (11) The Hipparcos Catalogue, (12) Prato et al. (2001), (13) Mamajek et al. (2002), (14) Graham & Frogel (1985), (15) Sandell & Weintraub (2001), (16) Ibragimov & Shevchenko (1990) and (17) Reipurth et al. (2002). **The extinction A_V** is taken from (18) Acke & van den Ancker (2004b), (19) Vieira et al. (2003), (20) Sylvester et al. (1996), (21) Mamajek et al. (2002), (22) Gredel (1994), (23) Value taken from Van den Ancker et al. (2004), but adapted to our photometry, (24) Reipurth et al. (2002).

Object	Class	Spectral Type	T_{adopted} [K]	$(\log g)_{\text{adopted}}$	V [mag]	$F_{12\mu\text{m}}$ [Jy]	$F_{1300\mu\text{m}}$ [mJy]	Ref.	Age [Myr]	Ref.	d [pc]	Ref.	A_V [mag]	Ref.
HD 34282	HAeBe	A0 e	10000	4.5	9.85	0.70	110 ± 10	(1)	5–10	(6)	400	(10)	0.28	(18)
HD 72106	HAeBe	A0 IV	9500	4.5	8.50	2.22	–	–	–	–	290	(11)	0.0	(19)
HD 98800	TTS	K5 / K7 / M1 V	4000	4.5	9.11	1.98	36 ± 7	(2)	7-10	(7)	47.6	(12)	0.31	(20)
MP Mus	TTS	K1 IV	4250	4.5	10.32	0.88	224 ± 8	(3)	8	(8)	86	(13)	0.17	(21)
V 346 Nor	FUOR	–	5500	4.5	16.3	7.50	273 ± 15	(4)	–	–	700	(14)	2.7	(22)
V 883 Ori	FUOR	–	5500	4.5	~ 15	52.5	549 ± 23	(4)	–	–	460	(15)	–	–
Z CMa	FUOR	–	30000	4.5	9–11	126.6	446 ± 16	(4)	0.3	(9)	930	(16)	3.8	(23)
BBW 76	FUOR	G0 – G2 I	5500	4.5	~ 12	1.02	13.3 ± 2.4	(5)	–	–	1800	(17)	2.1	(24)

Table 4.6: Results from TIMMI2 photometry and spectroscopy are merged in this table. The airmass and TIMMI2 integration time refer to N-band spectroscopy. Mid-IR photometry was obtained either in the N1 ($\lambda_0 = 8.6 \mu\text{m}$) or the N11.9 ($\lambda_0 = 11.6 \mu\text{m}$) passband. Errors represent the accuracy of this aperture photometry and do not necessarily include the uncertainty which measurements on different nights may introduce due to atmospheric fluctuations (errors caused by the latter one might amount up to 10% for the *fainter* sources).

Object	Time of Observation	Airmass (N-spec)	t_{int} (N-spec) [min]	F_{N1} [Jy]	$F_{\text{N11.9}}$ [Jy]
HD 34282	Dec 2002	1.2 – 1.4	67	–	0.60 ± 0.02
HD 72106	Mar 2004	1.3	25	–	2.89 ± 0.15
HD 98800	Jun 2002	1.1	16	0.83 ± 0.09	–
MP Mus	Dec 2002	1.5 – 1.7	49	–	0.73 ± 0.03
V 346 Nor	Sep 2003	1.2	12	–	7.29 ± 0.07
V 883 Ori	Mar 2004	1.4	6	–	52.5 ± 2.6
Z CMa	Mar 2004	1.2	6	–	183.8 ± 8.9
BBW 76	Mar 2004	1.2	28	–	0.82 ± 0.05

binary system HD 98800 B, which was later confirmed by Koerner et al. (2000). Prato et al. (2001) explained the excess by a circumbinary disk which is tidally truncated to an outer radius of 10–15 AU, and calculated a blackbody temperature of 150 K for the dust. In the following sections we always refer to the northern component B when talking about HD 98800. Infrared spectra covering the region around $10 \mu\text{m}$ were already published by Sylvester et al. (1996) and Sitko et al. (2000), but both spectra did not have adequate quality to discuss the mineralogy in detail.

- **MP Mus** (alias PDS 66) shows both strong H_α emission and K-band excess, indicative of accretion. It is the only classical TTS among a PMS population of 110 members in an OB association (Mamajek et al. 2002).
- **V 346 Nor** is considered as a FUOR. Prusti et al. (1993) gave corrected IRAS fluxes for V 346 Nor, since the values shown in the IRAS point source catalogue are contaminated by the close object Re 13.
- **V 883 Ori** is also classified as FUOR, based upon the similarity of its optical spectrum with that of FU Ori itself (Strom & Strom 1993). CO near-IR absorption bands support this assumption (Reipurth & Aspin 1997).
- The FUOR **Z CMa** is a well-studied source. Koresko et al. (1991) revealed the binarity of Z CMa with a separation of $0''.1$. The system probably consists of a B0 IIIe primary and a FUOR-type secondary. Both components have an estimated age of $\sim 3 \times 10^5$ yr (Van den Ancker et al. 2004). Mid-IR spectra were already presented by Cohen & Witteborn (1985) and Acke & van den Ancker (2004b). Because of the time-variant nature of FUORs, further spectra would be

helpful to investigate the spectral evolution of these objects in their fading and erupting phase.

- A review of the FUOR **BBW 76** (alias Bran 76) and its variability at optical and near-IR wavelengths was presented by Reipurth et al. (2002). The object illuminates its surrounding cloud in an extensive reflection nebula.

4.3.3 Observations and data reduction

The mid-IR observations were carried out during runs in June 2002, December 2002, September 2003 and March 2004 with the ESO TIMMI2 camera at La Silla observatory. Weather conditions did not permit Q-band imaging and we concentrated the photometry mainly on the N11.9 filter (central wavelength 11.6 μm). N-band spectra were obtained between 8 - 13 μm applying a standard chopping and nodding technique along the 3'' slit with a throw of 10''. For spectra, the airmass and on-source integration times are shown in Table 4.6. Standard stars for telluric correction and flux calibration had been selected from a list of mid-IR standard stars given on the TIMMI2 webpage⁵ and were observed close in time and airmass (< 0.2 relative to the targets' airmass). We apply the airmass correction described in Sect. 4.2 and furthermore correlate the spectrophotometric calibration with the obtained photometry. The wavelength calibration is optimised using the atmospheric absorption features of ozone (9.58 μm) and CO₂ (11.73 μm , 12.55 μm) in addition to the given wavelength calibration table. During the observations in 2002 the instrument was set up with a backup detector showing a low and varying response in one detector column. The corresponding area between approximately 9.0 and 9.7 μm is removed from the spectra presented in Sect. 4.3.4. In the run of September 2003, full spectral coverage was available again, but atmospheric conditions were instable and sometimes left uncorrectable ozone features around 9.5 μm . By comparing data from different nights and applying various standard stars for comparison, the exact position of the remnant feature is identified and removed from the spectra. Depending on the atmospheric quality, this leaves gaps of different sizes up to a maximum range between 9.4 and 9.7 μm . In total, the estimated average accuracy of the spectra (with regard to the noise) is better than 3% for V 346 Nor, V 883 Ori and Z CMa, around 5% for HD 34282 and HD 72106, 10 - 15% for HD 98800 and MP Mus, while for BBW 76 the accuracy is within 20%.

We also observed MP Mus at 1.2 mm with the bolometer array SIMBA at the SEST in La Silla. Details of these observations are given in Sect. 4.4.3. The object was detected with a flux density of 224 ± 8 mJy.

4.3.4 Analysis and modelling results

Apart from the mid-IR and mm photometry shown in Table 4.6, we collected fluxes from the literature in the passbands UBVRJ, JHK (2MASS), 12, 25, 60 and 100 μm (IRAS) as well as ISO and (sub-)millimeter data – where available. In Figs. 4.7 and 4.8 the resulting optical to mm spectral energy distributions (SED) are shown as an aid for

⁵<http://www.ls.eso.org/lasilla/sciops/3p6/timmi/html/stand.html>

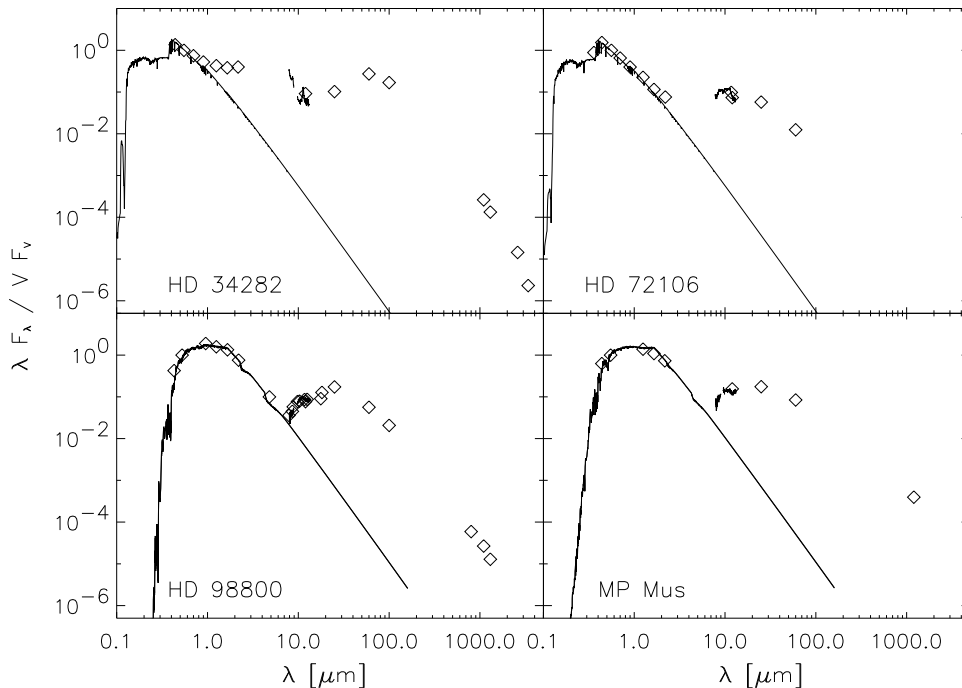


Figure 4.7: Optical to millimeter SED for the Herbig Ae and T Tauri stars in our sample, obtained through our observations or collected in the literature. For each source a suitable Kurucz model is overplotted to emphasise the contrast between the photospheric and the CS flux. The position of the TIMMI2 N-band spectra is indicated between 8 and 13 μm : the agreement with the photometry is excellent. We show the spectra in detail in Figs. 4.9 and 4.10.

interpreting the TIMMI2 N-band spectra. To emphasise the non-stellar contribution to the SED, we plotted a reddened Kurucz atmosphere model (Kurucz 1994) for the HAeBe and T Tauri stars, using the stellar parameters in Table 4.5. For the FUOR objects we did not plot a Kurucz model, since in these cases the V-band flux most likely arises from the star plus the hot inner part of the outbursting disk. The disk may be the dominant source and probably has a radial temperature distribution, rather than a single blackbody temperature, thus a single Kurucz model may not be sufficient to describe the contribution of the central source at all wavelengths. Nevertheless, from Figs. 4.7 and 4.8 it is recognisable that the excess emission of the FUORs is much larger than those of the HAeBes and TTS, suggesting that the FUORs have a larger amount of CS material.

In the interstellar medium (ISM) the dominant feature at 10 μm is caused by small, amorphous silicate grains (Kemper et al. 2004). When stars are formed out of their parental cloud, the material in their disks is assumed to have a similar composition as that found in the ISM. Changes in the size and composition are expected to occur during the subsequent evolution of the object, eventually leading to a planetary system. More precisely, grains start to grow and become crystalline through a process called thermal annealing. Laboratory experiments have shown that, due to thermal annealing,

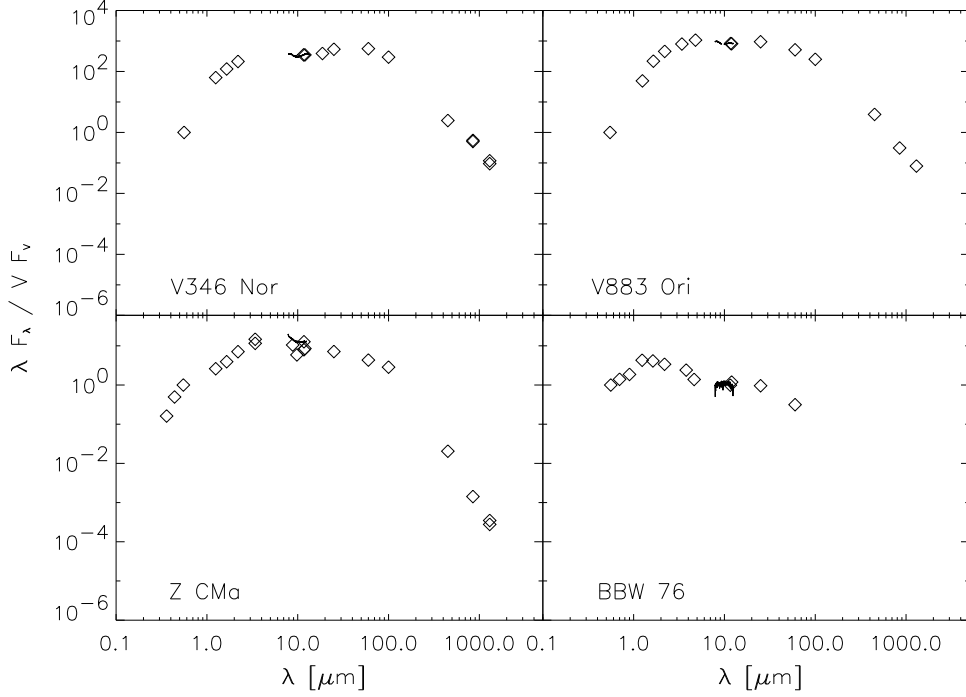


Figure 4.8: SEDs for the FUOR objects. No Kurucz model is plotted here as explained in the text.

amorphous silicates gradually turn into crystalline forsterite and silica (e.g. Rietmeijer 1989, Hallenbeck & Nuth 1997, Fabian et al. 2000). B2001 found a correlation between the amount of forsterite and silica in the disks of HAeBe, showing that thermal annealing indeed takes place in these objects. All the above-mentioned species emit in the N band, making this an excellent window to study dust evolution in the inner parts ($r < 10$ AU) of a protoplanetary disk.

The $10 \mu\text{m}$ silicate emission is thought to originate from a surface layer of the inner disk (Chiang & Goldreich 1997), which needs to be located close to the star as it is too large to be transiently heated, while PAH emission can originate from molecules located further away in the surface layer (also called 'atmosphere'), since these are excited by UV photons.

In Figs. 4.9 and 4.10 we show N-band spectra for our target sample and see that large differences exist between the sources. To quantify these differences and to determine the composition of their CS dust, we adopt the same procedure which was described by B2001 and Meeus et al. (2003) for interpreting mid-IR spectra of PMS stars. We first determine and subtract a local continuum to our TIMMI2 spectra by fitting a blackbody to the $8 - 13 \mu\text{m}$ region. Given the small wavelength range, this fit is not a unique solution but the absolute flux of the features after subtraction is correct within 10%. This uncertainty, however, has only a negligible effect on the derivation of the dust composition. Subsequently, we fit the continuum-subtracted spectra with a linear combination

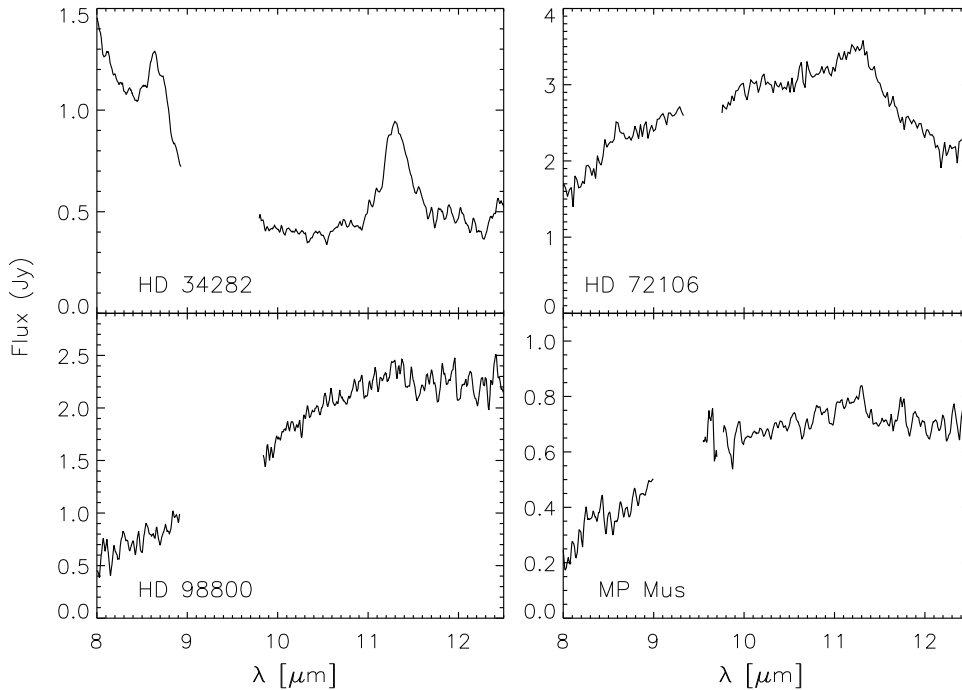


Figure 4.9: TIMMI2 spectra of the Herbig Ae and T Tauri stars. See the text for a discussion of the individual targets. For some objects, the data between approximately 9.0 and 9.7 μm has been removed, as there was a detector problem in 2002. Smaller gaps appear between approximately 9.4 and 9.7 μm , where we cut out uncorrectable atmospheric ozone features (cf. text).

of emission features from the following (dust) species which are commonly found in disks of PMS stars:

- Polycyclic Aromatic Hydrocarbons (PAHs)
- Amorphous olivine ($[\text{Mg,Fe}]_2\text{SiO}_4$) with grain sizes of 0.1 and 2.0 μm , which we will refer to as 'small' and 'large' silicate grains. We used absorption coefficients of spherical grains by Dorschner et al. (1995).
- Crystalline silicates: magnesium forsterite (Mg_2SiO_4) and enstatite (MgSiO_3). We assumed a continuous distribution of ellipsoids (CDE) for their shape. Coefficients for forsterite are from Servoin & Piriou (1973), for enstatite from Jaeger et al. (1998).
- Silica (SiO_2) coefficients, again adopting CDE, were taken from Spitzer & Kleinman (1961).

We took the absorption coefficients directly from B2001 and refer for a discussion on the influence of the grain shape on the spectroscopic signature to that article. Fig. 4.11 illustrates the wavelength dependence of the above-mentioned emission features. Modelling results for the emission spectra, together with the separate contribu-

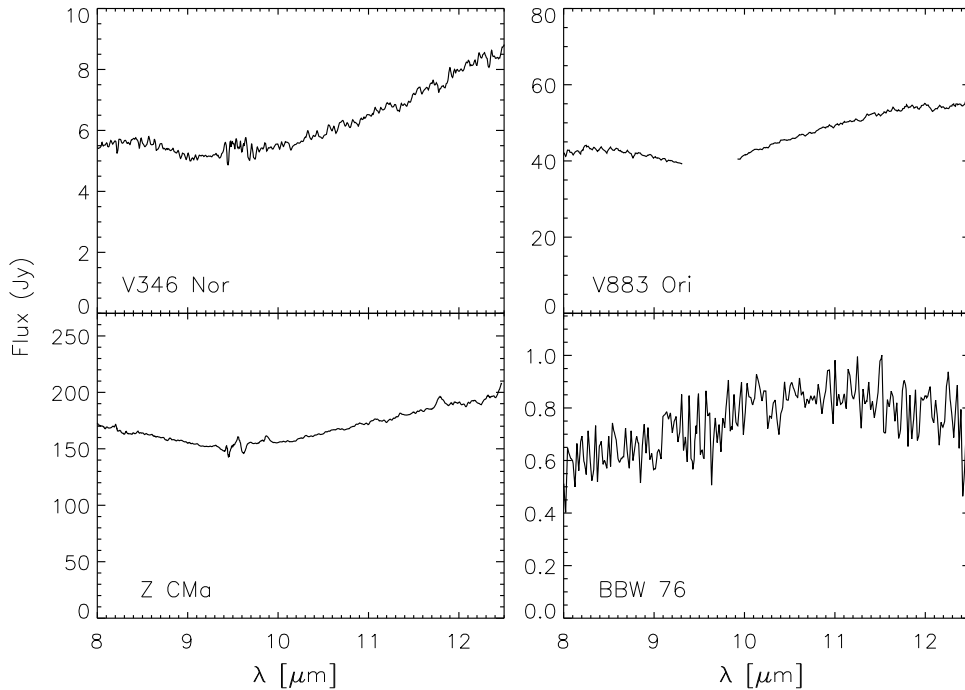


Figure 4.10: TIMMI2 spectra for the FUOR targets. See the caption of Fig. 4.9 for further details. The objects V 346 Nor, V 883 Ori and Z CMa show an absorption feature, pointing to optically thick material, while BBW 76 shows an emission feature, pointing to optically thin material in the line of sight.

tion of each dust component are shown in Fig. 4.12. When deriving in which amounts the different dust species are present, the linear coefficients of the fit – which are proportional to the radiating surface of the grains – need to be converted to mass. However, it is not possible to determine the absolute amount of mass of each species present, as we have no spatially resolved data to derive the particles’ size, density or temperature distribution as a function of radius within the disk. Therefore, we derived mass ratios of the different species under the assumption that (1) the particles are spherical and (2) the particles have the same density. The mass ratios are meaningful to compare the objects in our sample and to establish the amount of processed dust we observe at 10 μm . In Table 4.7 we list the derived mass ratios. Apart from $m_{2.0}/m_{0.1}$, which gives the mass ratio between large and small amorphous grains, the mass ratios always compare the mass of a particular species (forsterite, SiO_2 or enstatite) with the total mass in amorphous silicates (both small and large). Please note that for a given mass, small particles have a larger total emitting surface than large ones. Inversely, a similar amount of observed radiation will result in a much smaller mass when caused by small grains than if it was caused by larger grains.

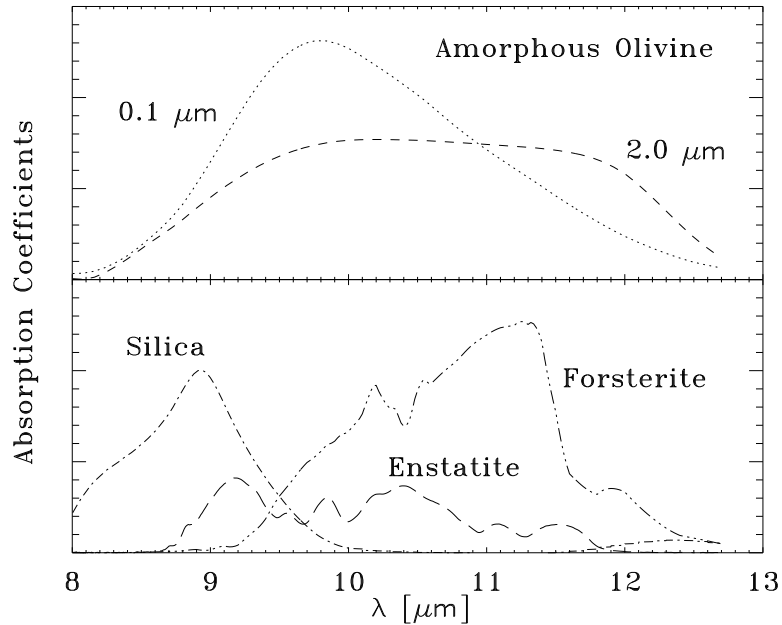


Figure 4.11: Emission features of the modelled silicate dust grains. The relative absorption coefficients are plotted against wavelength. **Top panel:** Absorption coefficients for large (*dashed curve*) and small (*dotted*) amorphous olivine. **Bottom panel:** Silica (SiO_2 - *dash-dotted*), crystalline forsterite (*dash plus three dots*) and enstatite (*long dashes*).

4.3.5 Discussion

Below we discuss for each object the result of our spectral decomposition and what could be derived from the appearance of its SED. It is important to repeat that our spectral results are *only valid for the warm dust*, which is located in the inner parts of the disk ($r < 10$ AU).

The HAeBe and T Tauri stars

- **HD 34282** shows very strong PAH features located at 8.7 and 11.2 μm . The peak at 8.7 μm is part of the 7-9 μm complex. There is an indication that the spectrum rises shortward of the displayed wavelength range towards the 7.7 μm PAH feature. Contrary to what is observed in other young sources (Hony et al. 2001), the 11.2 μm line is fairly symmetric.

We do not observe a silicate feature for this young HAe star, which can be explained if the silicate grains located in the inner parts of the disk are either (1) too cold or (2) too large to emit at 10 μm , as was shown for the HAe star HD 100453 (Meeus et al. 2002). Acke et al. (2004a) calculated a relatively shallow mm spectral index n of 3.36 (where $\lambda F_\lambda \propto \lambda^{-n}$, and $n = 3$ for a blackbody), which indicates the presence of larger, cold grains in the outer disk. This result

Table 4.7: Mass ratios derived from the model fits of the N-band spectra: large to small amorphous silicates ($m_{2.0}/m_{0.1}$), forsterite to amorphous silicates ($m_{\text{forst}}/m_{\text{sil}}$), SiO_2 to silicates ($m_{\text{SiO}_2}/m_{\text{sil}}$) and enstatite to silicates ($m_{\text{enst}}/m_{\text{sil}}$).

Object	$m_{2.0}/m_{0.1}$	$m_{\text{forst}}/m_{\text{sil}}$	$m_{\text{SiO}_2}/m_{\text{sil}}$	$m_{\text{enst}}/m_{\text{sil}}$
HD 72106	only large	1.03	0.33	0.48
HD 98800	12.0	0.38	0.04	–
MP Mus	5.3	0.26	0.11	–

is confirmed by Natta et al. (2004), who derive maximum grain sizes up to a few mm, based on mm observations. However, this reveals no information about the size distribution of the warm dust grains. Nevertheless, we suggest that also those grains have grown substantially: as shown above, the alternative to large grains would be grains with a too low temperature to radiate at $10\ \mu\text{m}$. A lack of warm silicate grains could only occur if these grains were shielded from the stellar radiation, e.g. by an inner puffed-up region as suggested by Dullemond et al. (2001). However, as is further discussed towards the end of this subsection, prominent PAH emission is not observed in such self-shielded disks. Thus, we conclude that the small silicate grains in the inner disk region must be strongly depleted, which was also the outcome of passive disk modelling by Dominik et al. (2003).

- The spectrum of **HD 72106** is devoid of small, amorphous silicate grains and is dominated by the crystalline silicates forsterite and enstatite. Also large amorphous silicates and SiO_2 are present. All these species are the result of dust processing within the CS disk. Until now, such a large fraction of processed dust has only been observed in the Herbig Be stars HD 100546 and HD 179218, making this object an important one for future studies in the context of planet searches.

Malfait et al. (1998b) were the first to compare the spectra of the HAeBe star HD 100546 with that of comet Hale-Bopp, finding a strong similarity. They suggested that both objects would have similar dust characteristics. In the upper panel of Fig. 4.13 we compare HD 72106 with a linear combination of the spectra for two solar-system comets: Hale-Bopp (Crovisier et al. 1997) and Halley (Bregman et al. 1987). The resemblance is remarkable, while the remaining deviation at 8.7 and $11.2\ \mu\text{m}$ might be due to the presence of PAHs in HD 72106. This similarity suggests that its inner disk is filled by comet debris, similar to those found in our own solar system. In the lower panel of Fig. 4.13 we compare HD 72106 with the Herbig Be object HD 179218, the only star for which the presence of enstatite is robustly derived (B2001). Interestingly, a high mass ratio of enstatite in comet Halley was also derived by the same authors. Enstatite can form when forsterite and silica are being annealed (Rietmeijer 1989). It is not clear why this process does not seem to occur in other objects. B2001 suggest that the presence of enstatite might be due to the high luminosity of

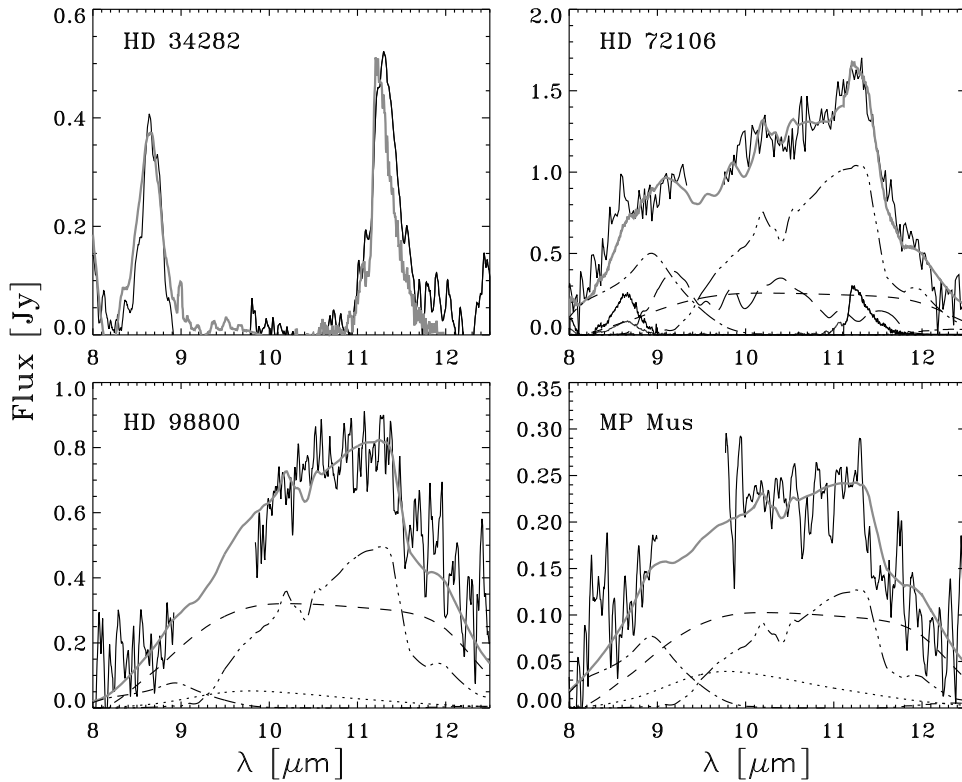


Figure 4.12: Continuum subtracted spectra of the PMS stars. **Upper left panel:** Comparison of HD 34282 (*thin black curve*) with the PAH features of BD+30 3639 (*thick grey curve*), a well-known source of PAHs (Hony et al. 2001). The PAH features at 8.7 and 11.2 μm are clearly visible and agree in position. **Other panels:** Decomposition of the 10 μm feature as described in the text. Same linestyles are used for the silicate components as in Fig. 4.11.

HD 179218 which gives rise to rapid dispersal of the gas. Interestingly, the SIMBAD database only states a luminosity class IV for HD 72106.

- The 10 μm spectrum of **HD 98800** was already shown by Sylvester et al. (1996) and later by Sitko et al. (2000), but both spectra did not have adequate quality to discuss the mineralogy in detail. Sylvester et al. (1996), however, noticed that the spectrum peaks longwards of 10 μm , which is typical for larger silicate grains. Our decomposition of the silicate feature indicates highly processed dust, dominated by both large amorphous olivine and crystalline forsterite. Small silicates have almost disappeared and we found no indication for the presence of enstatite.
- **MP Mus:** Grains have grown also in this disk and both large amorphous olivine as well as crystalline forsterite are found, while small olivine grains and SiO_2 are present in smaller amounts. Our mm observation suggests grain growth, but we need more mm data points to confirm this.

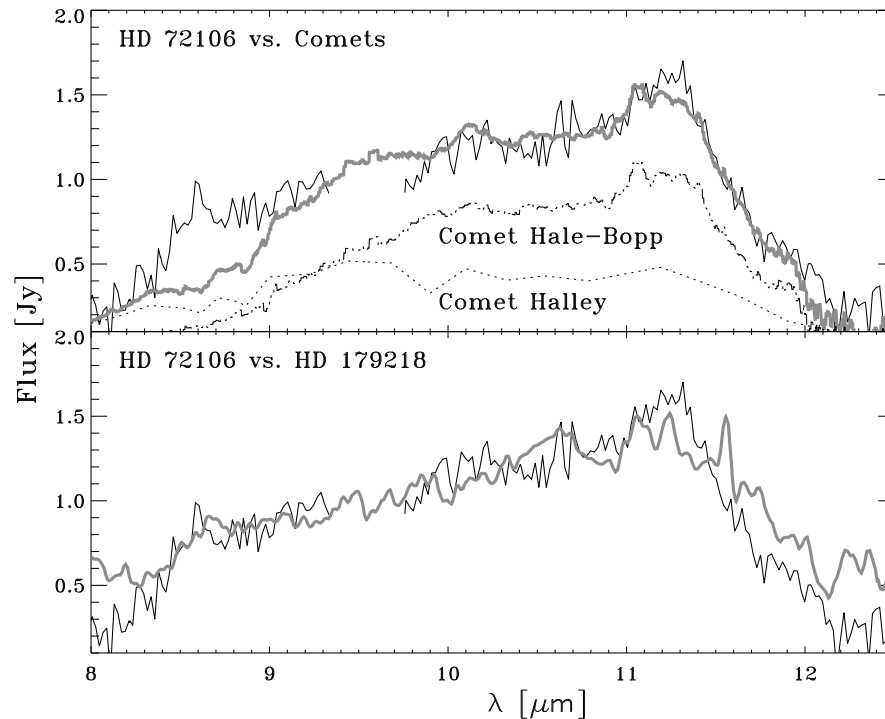


Figure 4.13: **Top panel:** Comparison of the Herbig Ae star HD 72106 (*solid black curve*) with a combination of the comets Halley and Hale-Bopp (*thick grey line*, scaled intensity). The resemblance is remarkable and has, among PMS objects, only been found for the Herbig Be star HD 100546. **Bottom panel:** Comparison with the Herbig Be star HD 179218. This object was – until now – the only known stellar host of enstatites.

The Herbig Ae stars HD 34282 and HD 72106 both are spectral type A0 and should have a similar level of UV flux. However, the strength of their PAH features is much stronger for HD 34282. Following M2001 and Acke & van den Ancker (2004b), we can relate this difference to their disk geometry. M2001 classified the HAeBes into two groups, based upon the shape of their SED. *Group I* objects have a rising mid-IR SED, which can be fitted with a power-law and a blackbody continuum and is attributed to a flared disk geometry. *Group II* objects show a smaller mid-IR excess, their SED can be explained with a power-law and is related to a flat disk geometry. This geometrical model was later confirmed by Dullemond (2002), who made a self-consistent model and showed that Group I sources have flared disks, while representatives of Group II possess flat self-shadowed disks. M2001 noted that the strongest PAH emission occurs in Group I sources, while it is much weaker or even absent in Group II. This was confirmed by Acke & van den Ancker (2004b) for a larger sample of 46 HAeBes. In the flared disks, PAHs residing in the disk atmosphere are easily hit by UV photons, while in a self-shadowed disk the thick inner disk rim might intercept those UV photons, giving rise to weaker or even absent PAH emission. Indeed, HD 34282 is a member of Group I, while HD 72106 is a member of Group II, what can explain the differences in PAH strength.

The FU Ori sources

FU Ori objects are most likely still in a – non-steady – accreting phase and embedded in (part of their) parental cloud. Therefore, we expect to see absorption features rather than emission in the infrared, although Hanner et al. (1998) already found FUORs with silicate emission. Given the large variability of FUORs in the optical, attributed to accretion events, studies of these variations in the infrared have meanwhile begun (Ábrahám et al. 2004).

- The SEDs of **V 346 Nor**, **V 883 Ori** and **Z CMa** show a large infrared to millimeter excess, pointing to the presence of a circumstellar envelope enshrouding these objects. Superimposed on the dust continuum emission, the 10 μm silicate feature appears in absorption. In Fig. 4.14 we compare the absorption features of these targets with a source of amorphous silicates, the interstellar medium. For this purpose, we use the observed absorption of the ISM in the direction of the galactic centre (Sgr A*) and follow the method by Kemper et al. (2004) to convert the absorption feature into optical depth. The spectrum of V 346 Nor agrees well with that of the ISM, while for the other two FUORs we see larger differences. V 883 Ori seems to have extra emission on top of its absorption, while Z CMa appears to have larger silicates than seen in the ISM.

In Fig. 4.15 we compare the spectral shapes of V 346 Nor and Z CMa obtained with TIMMI2 to ISO-SWS data from August 1996 (V 346 Nor) and November 1997 (Z CMa). The ISO spectrum of V 346 Nor was obtained from the ISO data archive and has not been published before. We had to shift the TIMMI2 spectrum of Z CMa downwards by 75 Jy to match the ISO-SWS spectrum, most likely due to the variability of this target. Within the errors, the spectral shapes agree. We further compare this steady behaviour in the N-band with optical photometry of Z CMa by van den Ancker et al. (2004). As therein no data for 2004 is included yet, we refer to the year 2003. After a period of slow fading, the object became brighter in 1999 during a six month period, after which it faded again to its previous brightness. Between the two spectral observations, it increased by a few tenths of a magnitude, but no large eruption has been observed. For V 346 Nor we did not find optical data in the required timespan, while during the period 1980-1998 the object became brighter in the K-band (Ábrahám et al. 2004). We thus do not dispose of enough material yet to draw any conclusions concerning the optical variability in correlation with the IR spectral variability.

- **BBW 76:** Contrary to the three other FUORs, this object shows a smaller fraction of IR excess, suggesting that it is less embedded than the other three. Also the absence of an absorption feature, caused by optically thick material, confirms this suspicion. Is this object in a different (accretion) stage than the other FUORs? It may be an interesting target for further studies, but not unique, as Hanner et al. (1998) already found FUORs with silicate emission. We did not model the spectrum, as it has a low quality, but its shape suggests that PAHs and crystalline features are not present.

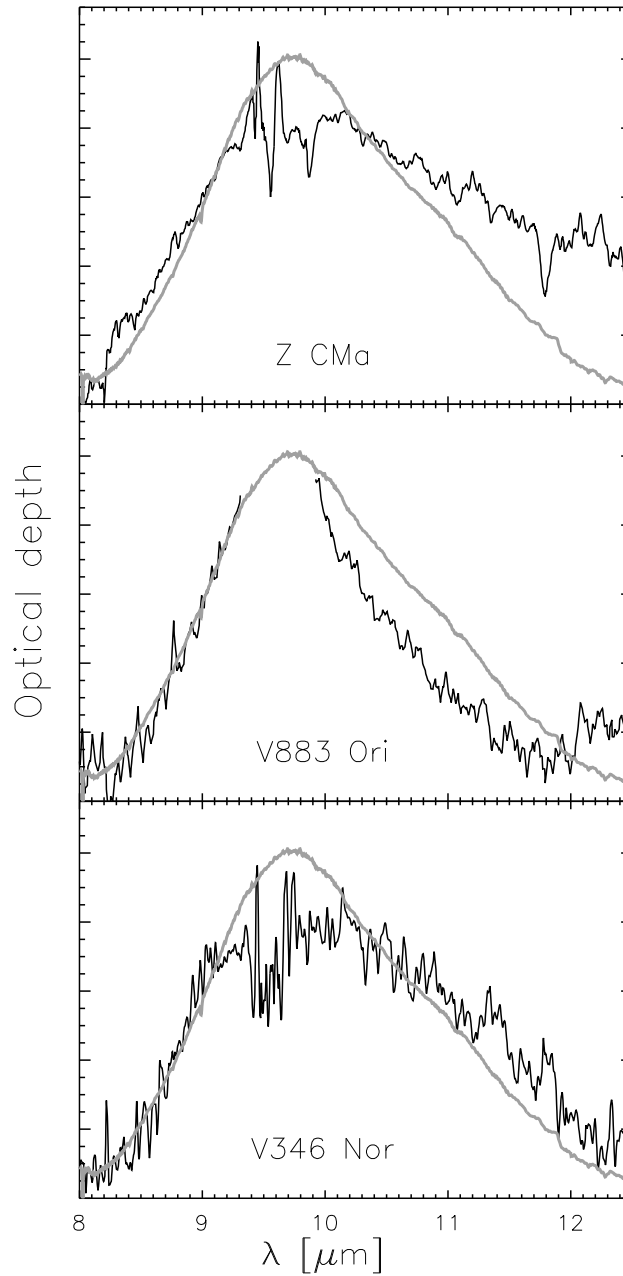


Figure 4.14: The optical depth towards V 346 Nor, V 883 Ori and Z CMa is compared with the optical depth towards the galactic center (*grey curve*). For further details, see the text. The features around 9.5 μm were caused by variable ozone emission.

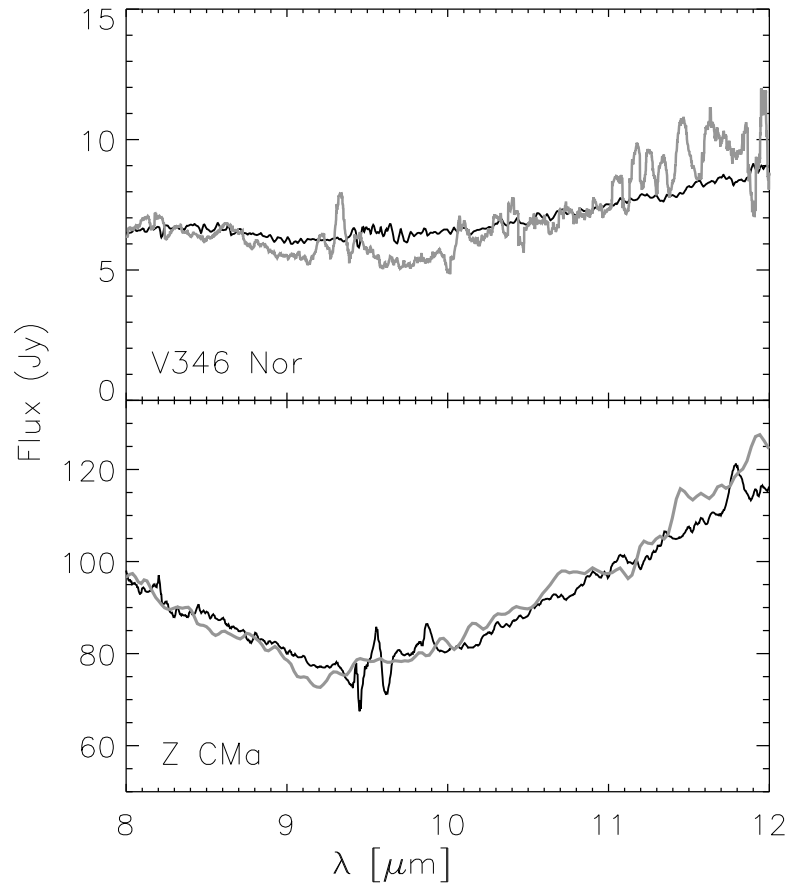


Figure 4.15: Comparison of the spectral shapes for V 346 Nor and Z CMa at different epochs. *Dark line:* data from this work. *Grey line:* ISO-SWS data are taken on August 31st, 1996 (V 346 Nor) and November 7th, 1997 (Z CMa). The spectral shapes although taken at different epochs agree with each other.

A follow-up study, observing these objects at several different epochs, together with simultaneous optical photometry is necessary to establish the cause of the FUOR phenomenon.

Comparison with previous studies

The method we used to interpret our 10 μm spectra was – to our knowledge – only used by B2001 (who developed the method), Meeus et al. (2003), Przygodda et al. (2003) and Honda et al. (2003). We will refer mainly to those studies to compare our results.

B2001 analysed the 10 μm spectra of 14 optically visible HAeBes and found large differences between the objects: some were dominated by amorphous silicate grains

(e.g. AB Aur), others were rich sources of crystalline silicates (e.g. HD 100546). Of the two HAeBes in our sample, only HD 72106 shows a silicate emission feature. This source is dominated by large and crystalline grains and is similar to HD 179218 and HD 100546, which also stood out in the study of B2001. HD 72106 is thus a source of highly processed dust, which is not often observed in the group of known HAeBes, and can be considered as a very interesting object in the framework of dust evolution. It is the second known source of enstatite (after HD 179218). The presence of this dust species might be related to a high luminosity of the central sources. M2001 found in their sample of 14 HAeBes four objects which did not show silicate emission, Acke & van den Ancker (2004b) report a non-detection of this feature for 16 of their 46 sources. We can conclude that the absence of the feature in HD 34282 is not uncommon for a Herbig star.

Meeus et al. (2003) analysed three T Tauri stars in Cha I (age ~ 1 Myr) and found a similar variety among those objects: CR Cha is dominated by amorphous silicates, while VW Cha is a source of large, crystalline silicates. The anti-correlation between silicate grain size and strength of the emission band, as found by van Boekel et al. (2003) for a sample of HAeBes, was confirmed by Meeus et al. (2003), a result that was repeated for a larger sample of 16 TTS by Przygodda et al. (2003). Meeus et al. (2003) also found a correlation between the amounts of silica and forsterite, as observed by B2001 for their sample of HAeBes. It was concluded that the dust properties of TTS are very similar to those observed in HAeBes. Honda et al. (2003) studied the 1 - 10 Myr old TTS Hen3-600 and showed that its dust emission consists mainly of large and crystalline silicates. Our two TTS are also dominated by large and crystalline silicates and possess more evolved dust than the Cha I sample. It is tempting, based upon the findings of this section and the above-mentioned TTS studies, to attribute the presence of highly evolved dust to a higher age (7 - 10 Myr), but the sample is still too small to derive a firm conclusion. A larger number of TTS with known ages need to be studied for this purpose. Also, a relation between the amount of dust processing and age has not been established for HAeBe stars.

4.3.6 Summary and conclusions

We presented spectral energy distributions and N-band spectra of eight PMS stars surrounded by a circumstellar disk, and analysed the dust composition of the spectral emission sources by fitting the observed spectra with known spectral features of different dust species and PAHs. Our sample is too small and heterogeneous to look for a correlation between the dust properties and the objects' properties, therefore we concentrated on each source individually.

The T Tauri and Herbig stars show a SED and emission features in qualitative agreement with the model of a flared or self-shadowing disk surrounded by an optically thin, hot surface layer from which the emission features originate (Chiang & Goldreich 1997, Dullemond 2002). Strong PAH features are found for HD 34282 but no silicate emission, which indicates that small silicates are strongly depleted in this disk. No clear features of PAH are detected in HD 72106, what we attribute to the geometry of the disk which is probably self-shadowed. The most important result of this section

is the dust composition of HD 72106, a host of highly processed silicates, similar to those seen in solar-system comets. We also detected enstatite in HD 72106, which is a rare finding in CS disks and might point to rapid gas dispersal due to a higher luminosity of the central star. This target may be a good candidate for extra-solar planet searches, given its similarity to spectra of solar-system comets. Processed dust is also found around the relatively old T Tauri stars (7 - 10 Myr) HD 98800 and MP Mus, but no enstatite was seen in these objects.

For the FU Ori targets, we observe absorption features in three of the four cases, which is expected for objects embedded in optically thick material. One of the targets – BBW 76 – shows the silicate feature in emission and is likely less embedded. Multi-epoch simultaneous observations from the optical to the mid-IR are required to study their disk structure and the mechanisms driving their variability.

4.4 Disks around Vega-type and post-main sequence stars

We present spectral energy distributions and new N-band photometry and spectroscopy for a sample of six main sequence stars and one post-MS object using the ESO TIMMI2 camera at La Silla observatory (Chile). All objects are thought to possess circumstellar material and for the majority of the targets this is their first N-band spectroscopic observation. The emission spectra (observed in three cases), modelled with a mixture of silicates consisting of different grain sizes and composition, confirm the suspected presence of disks around these targets. The most important discovery is that HD 113766, a young Vega-type star, is host to highly processed dust which is probably second generation. It is the first time a Vega-type star with such highly evolved dust has been observed. Silicate emission of basically unevolved dust is seen in case of the post-MS object HD 41511 and the Vega-type star HD 172555. In addition, to study the cold dust, we observed a subsample at 1200 μm with the bolometer array SIMBA at the SEST in La Silla but we only got upper limits for those five objects. This shows that these Vega-type stars have a smaller amount of dust than their precursors, the T Tauri and Herbig Ae/Be stars.

4.4.1 Introduction

Circumstellar (CS) disks are expected and observed to gradually disappear. The disk evolution is witnessed in the spectral energy distribution by a transition from a dust-dominated to a star-dominated appearance. In the pre-main sequence phase, when the stars are optically visible, the presence of these disks causes an excess that stretches from the near-IR to the millimeter (mm) regime. In a following stage, the near-IR excess disappears first, which is often attributed to clearing of the inner disk, thus creating a gap around the central star (e.g. Malfait et al. 1998a).

As these disks further evolve, their gas content diminishes and the dust is also gradually removed. Observations have shown that by an age of roughly 15 Myr most of the disk mass has disappeared, as searches for molecular gas around older objects result in non-detections (e.g. Greaves et al. 2000, Zuckerman et al. 1995). From the theoretical point of view, numerical simulations for the formation of giant planets by Pollack et al. (1996) predict that these are formed during the first 10 - 16 million years. Thus, formation of gas giants – if taking place – must be completed by that time, as after the gas dispersal not enough material will be left to still form them. It is thus important to study those transition systems where the disk is evolving but which still have enough material to form planets. These objects have an age of roughly 10 to 20 Myr.

It was a surprising discovery of IRAS (Aumann et al. 1984) that several much older main sequence stars, such as Vega (350 Myr), still possess a far-IR excess. These objects are now classified as *Vega-type* and their infrared excess is attributed to the thermal re-emission of dust particles at a temperature between 50 and 125 K (Backman & Paresce 1993; Laureijs et al. 2002).

Once the gas is cleared out in a protoplanetary disk, which may occur at timescales as short as 10 Myr, the dust is not coupled anymore and smaller particles will be removed through various processes (e.g. Poynting-Robertson drag, particle collision, radiation pressure; see Backman & Paresce 1993 for an overview). The grain removal timescales are shortest in the inner regions of the disk and may be as short as a few 10^5 yr for an A0 type star. If dust is still observed to be present, it must be replenished, as otherwise the inner boundaries would rapidly move outwards. An important source of dust replenishment is thought to be the collision of planetesimal-sized bodies within the CS disk (Backman & Paresce 1993). As these reservoirs become smaller and the age of the sources increases, it is expected that the inner boundary of the disk moves outwards, resulting observationally in a gradual disappearance of first the mid-IR and later also the far-IR excess until the excess becomes undetectable. Habing et al. (2001) have investigated the incidence and survival of remnant disks around main-sequence (MS) stars from observations with ISOPHOT and found that at least 15% of the nearby field stars of spectral type A to K have CS dust. Greaves & Wyatt (2003) find a much higher detection rate of debris towards MS A-type than to G-type stars, even within a similar age-bin. The time dependency of Vega-like excesses was further studied by Decin et al. (2003) who reviewed previous results from other authors and cannot confirm a global power law for the amount of dust seen in debris disks as a function of time. About the properties – composition and size distribution – of the warm dust encircling Vega-type objects, little is known so far. Some N-band spectra of Vega-like stars were shown by Sylvester et al. (1996) and Sylvester & Mannings (2000), however, most of the objects in their sample were Herbig Ae/Be stars which are close to the zero-age main sequence.

In Sect. 4.3 we have analysed the mid-IR emission of eight pre-main sequence stars (two T Tauri, two Herbig Ae/Be stars and four FU Ori type objects). Here we present a search and analysis of CS matter for a sample of Vega-type stars and disk candidate objects. Our final goal is to prove the existence of CS matter and to get insight into the dust composition from modelling the N-band silicate emission features – where present. In Sect. 4.4.2 we introduce our targets and describe in Sect. 4.4.3 the obser-

vations and data reduction. The spectral energy distributions (SED) are discussed in Sect. 4.4.4, while the spectra are analysed in Sect. 4.4.5. We derive upper limits for dust masses in Sect. 4.4.6.

4.4.2 Observed sources

Most objects in our sample are classified as disk candidates in the literature and show excess emission towards longer wavelengths. With one exception, HD 41511 – a post-main sequence star with dust outflow, all sources are main sequence stars. A summary of our targets and their stellar parameters together with known IRAS and mm fluxes is given in Table 4.8. We note that for many of our sources this is their first observation in the mid-IR, apart from IRAS, and give references in those cases where further mid-IR data have been published.

- **HD 10647** (alias η Eri) is a Vega-type source with 60 μm excess detected from ISOPHOT data (Decin et al. 2000). A planet (2.10 AU semi-major half axis, $M = 0.91 M_{\text{Jup}}$) was recently discovered (Mayor 2003).
- **HD 38678** (alias ζ Lep) shows excess emission around 25 μm (Laureijs et al. 2002) and 60 μm (Habing et al. 2001) measured with ISOPHOT. Based on photometry and a marginally resolved emission at 17.9 μm , obtained with the Keck I telescope, Chen & Jura (2001) conclude that the dust may reside within 6 AU distance to the star and is likely being replenished by collisions of larger bodies.
- **HD 40932** (alias μ Ori) is a spectroscopic quadruple system whose members might still possess a remnant debris disk. The amount of IR excess is controversial. Since the object was mentioned in a list of IR excess stars by Oudmaijer et al. (1992), its Vega-type status is a matter of speculation, although Oudmaijer et al. (1992) had clarified that the IRAS fluxes given for this source were upper limits. No IRAS measurements are displayed in SIMBAD.
- The binary system **HD 41511** (alias SS Lep) consists of an A-type star with an M-type companion. For many years the primary was considered a Herbig Ae/Be (HAeBe) candidate, while now both components appear to lie beyond the main sequence (e.g. Jura et al. 2001). Based on an analysis of the sub-mm to mm SED, Jura et al. (2001) suggest that the stellar outflow forms a circumbinary disk in which larger grains are formed by coagulation. Indications of a possible 10 μm emission feature seen in IRAS low-resolution spectra is discussed by Fajardo-Acosta & Knacke (1995).
- Mannings & Barlow (1998) confirmed **HD 113766** as a Vega-like source. The unresolved excess flux was found to originate from the primary star of this binary system (Meyer et al. 2001) with a separation of $1''.335$ (Fabricius & Makarov 2000). Hints of spectral features can be seen in (unpublished) ISOPHOT data, obtained from the ISO Data Archive⁶.

⁶<http://www.iso.vilspa.esa.es/ida/>

Table 4.8: Stellar parameters and known fluxes of our target sample. V-band magnitudes and the IRAS 12 μm fluxes are taken from the SIMBAD database. T_{adopted} and $(\log g)_{\text{adopted}}$ list the temperature and surface acceleration which we used for the Kurucz atmosphere models. The mm-flux of HD 41511 was measured in Jura et al. (2001). **Stellar ages:** (1) Zuckerman & Song (2004) quote 300 Myr with a caveat (methods used: X-ray emission and lithium age). Decin et al. (2000) give 3500 Myr as an upper range (isochrones). (2) Song et al. (2001, evolutionary tracks), (3) Song et al. (2001, evolutionary tracks), (4) Meyer et al. (2001, estimation from evolutionary tracks), (5) Zuckerman & Song (2004), (6) Lachaume et al. (1999, isochrones and Ca lines). **The distances** are taken from (7) Decin et al. (2000), (8) Chen & Jura (2001), (9) Fekel et al. (2002), (10) Jura et al. (2001), (11) Meyer et al. (2001), (12) Zuckerman et al. (2001), (13) Jourdain de Muizon et al. (1999).

Object	Class	Spectral Type	T_{adopted} [K]	$(\log g)_{\text{adopted}}$	V [mag]	$F_{12\mu\text{m}}$ [Jy]	$F_{1350\mu\text{m}}$ [mJy]	Age [Myr]	Ref.	d [pc]	Ref.
HD 10647	Vega-type	F8 V	6000	4.5	5.52	0.82	–	300–3500	(1)	17.4	(7)
HD 38678	Vega-type	A2 Vann	9000	4.5	3.55	2.18	–	231	(2)	21.5	(8)
HD 40932	MS	A5/F5 V	7500	4.5	4.13	–	–	693	(3)	47.5	(9)
HD 41511	post-MS	Apsh	9000	4.5	4.97	143.5	25.4 ± 2.4	–	–	330	(10)
HD 113766	Vega-type	F3/F5 V	6750	4.5	7.56	1.59	–	10–20	(4)	130	(11)
HD 172555	Vega-type	A5 IV-V	7500	4.5	4.78	1.47	–	12	(5)	29.2	(12)
HD 207129	Vega-type	G0 V	6000	4.5	5.58	0.81	–	6000	(6)	15.6	(13)

Table 4.9: Results from TIMMI2 photometry and spectroscopy as well as SIMBA observations are merged in this table. The airmass and TIMMI2 integration time refer to N-band spectroscopy. Mid-IR photometry was obtained in the N11.9 passband ($\lambda_0 = 11.6 \mu\text{m}$). Errors represent the accuracy of this aperture photometry and do not necessarily include the uncertainty which measurements on different nights may introduce due to atmospheric fluctuations (errors caused by the latter one might amount up to 10% for the *fainter* sources).

Object	Airmass (N-spec)	t_{int} (N-spec) [min]	$F_{\text{N11.9}}$ [Jy]	t_{int} (1200 μm) [min]	$F_{1200\mu\text{m}}$ [mJy]
HD 10647	1.1	31	0.55 ± 0.03	248	< 17
HD 38678	1.4	37	1.62 ± 0.04	–	–
HD 40932	1.3	31	1.05 ± 0.02	45	< 24
HD 41511	1.1	4	117.0 ± 0.1	–	–
HD 113766	1.6	25	2.12 ± 0.02	83	< 18
HD 172555	1.3 – 1.4	40	1.20 ± 0.04	83	< 26
HD 207129	1.1	37	0.70 ± 0.05	178	< 15

- **HD 172555** was identified as Vega-type by Mannings & Barlow (1998) by cross-correlating the Michigan Catalog of Two-dimensional Spectral Types for the HD Stars with the IRAS Faint Source Survey Catalog.
- **HD 207129** is surrounded by a cold, ring-like debris disk, as concluded from ISO photometry by Jourdain de Muizon et al. (1999). In contrast to the independent methods by which Lachaume et al. (1999) derived a solar-like age, Zuckerman & Webb (2000) estimate an age of only 40 Myr, relying on space motion and location in space. This object demonstrates that for some sources the age determination done with different methods is not always consistent.

4.4.3 Observation and data reduction

The mid-IR observations were carried out during runs in December 2002 and September 2003 with the ESO TIMMI2 camera at La Silla observatory. In Sect. 4.3.3 we describe the observations and data reduction in detail.

For those targets in our sample which have never been studied longward of the infrared, additional observations were obtained in November 2002 and July 2003 with the 37-channel bolometer array SIMBA at the SEST in La Silla (cf. Sect. 5.1.2). We used the fast scanning mode at 250 GHz ($\lambda = 1200 \mu\text{m}$). Corresponding integration times are listed in Table 4.9. The data reduction with MOPSI⁷ includes despiking, baseline fitting, suppression of the correlated sky noise, opacity and gain-elevation correction as well as co-adding the single maps to a final one (cf. the Appendix in Chini et al. 2003 for a short introduction to MOPSI). Uranus was used as flux calibrator.

⁷MOPSI has been developed and is maintained by R. Zylka (IRAM, Grenoble, France)

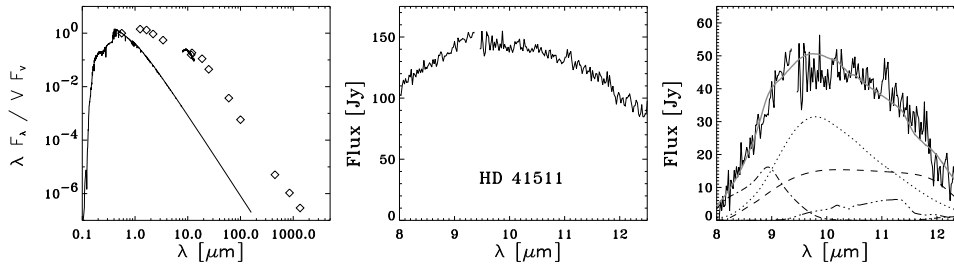


Figure 4.16: **Left panel:** Spectral energy distribution for the post-MS star HD 41511. **Mid panel:** The corresponding TIMMI2 N-band spectrum. **Right panel:** Decomposition of the dust emission. The different linestyles represent small amorphous olivine (*dotted*), large amorphous olivine (*dashed*), silica (SiO_2 , *dash-dotted*) and crystalline forsterite (*dash-three dots*).

4.4.4 Spectral Energy Distributions

We used the TIMMI2 and SIMBA photometry in Table 4.9 to construct a spectral energy distribution (SED) for the targets, together with additional fluxes from the literature in the passbands UBVR, JHK (2MASS), 12, 25, 60 and 100 μm (IRAS) as well as ISOPHOT data – when available. For HD 41511 (sub-)mm data already existed. In Figs. 4.16 and 4.17 the resulting optical to mm spectral energy distributions are displayed, with an indication of the TIMMI2 N-band spectra to show their agreement with the photometry. To emphasise the non-stellar contribution to the SED, we plotted a Kurucz atmosphere model (Kurucz 1994) with the stellar parameters in Table 4.8. We applied no reddening correction for the Vega-type sources as their relatively cold CS material is unlikely to cause a significant extinction – also reflected in their observed [B-V]. For HD 41511, however, we reddened the Kurucz model with an $A_V = 0.8$ mag (Malfait et al. 1998a).

The SED of the quadruple system HD 40932 can be entirely explained by stellar emission (its given photometry includes all four components). For HD 10647, HD 38678, HD 172555 and HD 207129 a moderate excess emission begins longward of 8 μm or even further. HD 113766 shows substantial excess starting around 8 μm , but none in the near-IR. This can be explained by the absence of hot CS material located close to the star, suggesting that an inner hole in the disk was created.

The post-main sequence object HD 41511 has the largest excess in the sample, ranging from the J-band to the mm region, that has been attributed to a circumbinary disk (Jura et al. 2001). Its SED shows resemblance to that of the binary post-AGB star HR 4049. Dominik & Dullemond (2003) proposed a model for HR 4049, in which a massive circumbinary disk is highly optically thick and possesses a very hot inner disk rim that causes the near-IR excess. Since – unlike HR 4049 – we also see 10 μm emission, an optically thin layer surrounding the optically thick disk is further required, in which warm silicate grains reside and re-radiate the absorbed UV and optical photons.

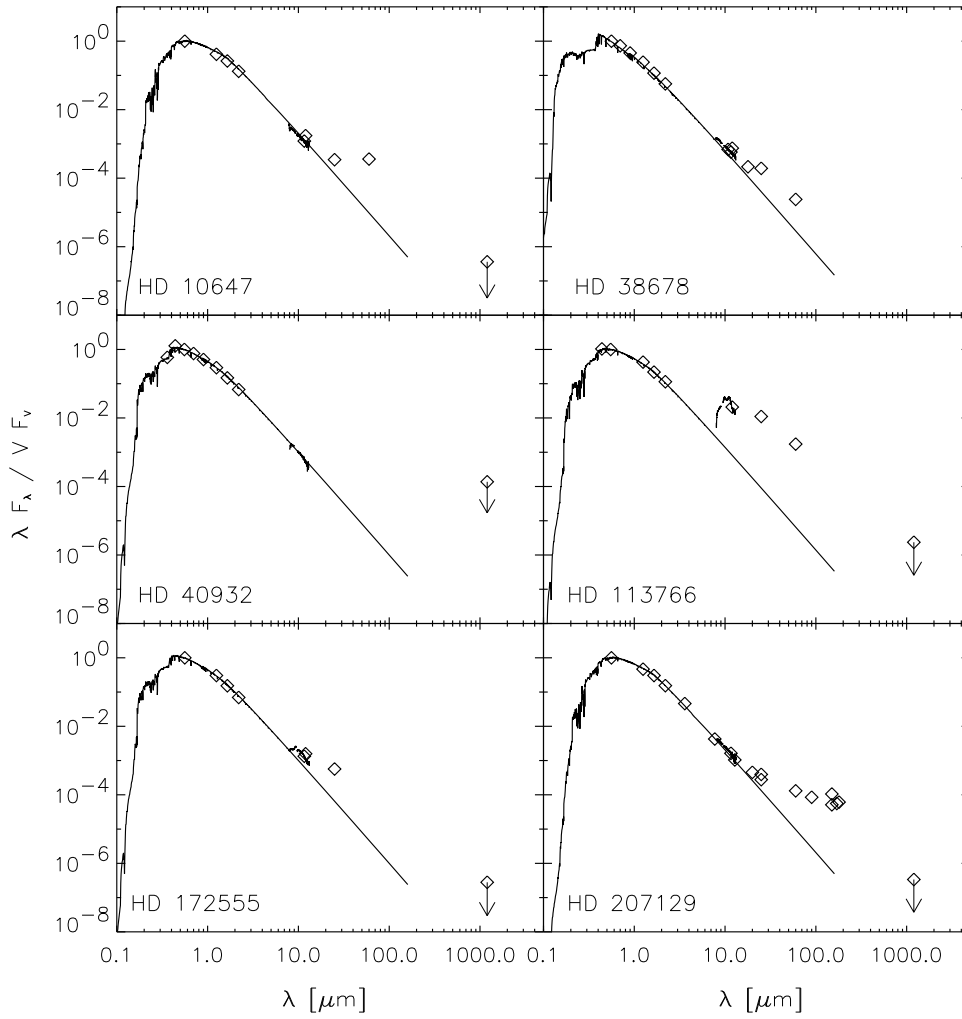


Figure 4.17: Spectral energy distributions for our Vega-type sources. A Kurucz model is overplotted to represent the stellar contribution to the SED. The mm-fluxes are upper limits, as indicated by the arrow.

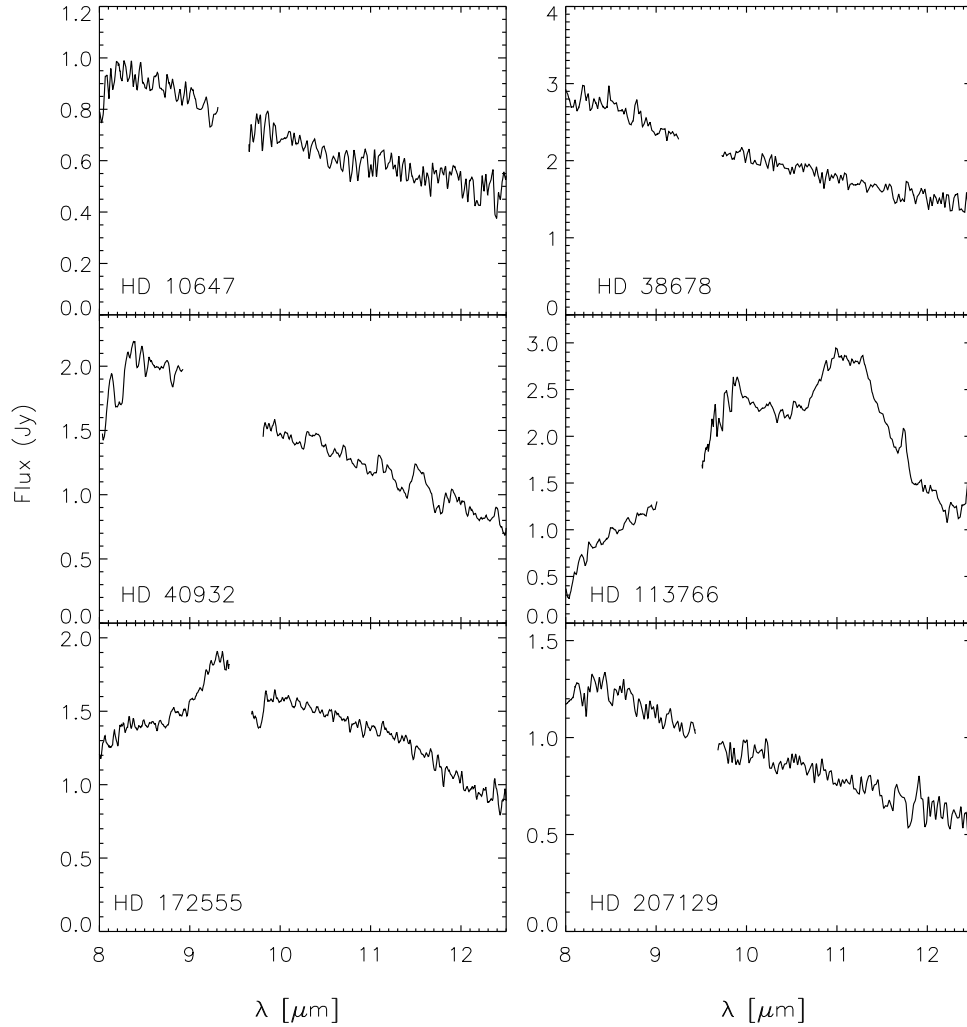


Figure 4.18: TIMMI2 spectra of the Vega-type stars. For some objects the data between approximately 9.0 and 9.7 μm is removed, as there was a detector problem in the 2002 run. Smaller gaps between about 9.4 and 9.7 μm occur where we cut out uncorrectable atmospheric ozone features.

4.4.5 Mid-IR spectral features

In Figs. 4.16 and 4.18 we show the N-band spectra for all targets. To quantify the differences between these sources and to determine the composition of CS dust, we adopt the same procedure as described in Sect. 4.3.4.

Meeus et al. (2003) concluded that dust around HAeBe stars and T Tauri stars has very similar characteristics. Therefore, we model our current sample of Vega-type stars with the same dust species as those found in young stellar objects, as their evolutionary predecessors are most likely Herbig and T Tauri stars.

To determine the composition of the CS dust, we first determine and subtract a local continuum to our TIMMI2 spectra by fitting a blackbody to the 8 - 13 μm region. Subsequently, we model the continuum-subtracted spectra with a linear combination of emission features from the dust species characterised in Sect. 4.3.4.

We applied the absorption coefficients from Bouwman et al. (2001). PAHs were not included in the fit, as we did not detect any PAH features in our spectra. Modelling results for the emission spectra, together with the separate contribution of each dust component are shown in Figs. 4.16 and 4.19. The mass ratios of the dust components are meaningful to compare the objects in our sample and to establish the amount of processed dust we observe at 10 μm . In Table 4.10 we list the derived mass ratios. Apart from $m_{2.0}/m_{0.1}$, which gives the mass ratio between large and small amorphous grains, the mass ratios always compare the mass of a particular species (forsterite or SiO_2) with the total mass in amorphous silicates (both small and large). Please note the caveats which we already addressed in Sect. 4.3.4 about how to interpret the mass ratios. It is also important to point out again that our results are only valid for the warm dust, which is located in the inner part of the disk ($r < 10$ AU) and radiates in the 10 μm region.

Vega-type stars

- **HD 10647** and **HD 38678**: The spectra we observe are stellar, excess emission is only found longward of 25 μm resp. 18 μm . The far-IR excess of these objects can be explained by a remnant, low-mass debris disk around these rather old (≤ 3500 and 231 Myr) main-sequence stars. Absence of an IR excess at shorter wavelengths could be a result of the clearing of large inner disk parts, possibly due to planets orbiting these stars. Indeed, a planet around HD 10647 has been reported (cf. Sect. 4.4.2).
- **HD 40932**: No indication of CS material is seen in the SED, so we conclude that this source is not a Vega-type candidate.
- The spectrum of **HD 113766** is dominated by crystalline silicate (forsterite) and large, amorphous silicates. Small grains and SiO_2 are quasi absent. In Fig. 4.20, upper panel, we show the similarity of HD 113766 with the solar-system comet Hale-Bopp, while in the mid panel it is compared to the Herbig Be star HD 100546. Both comparison objects have very similar spectral fea-

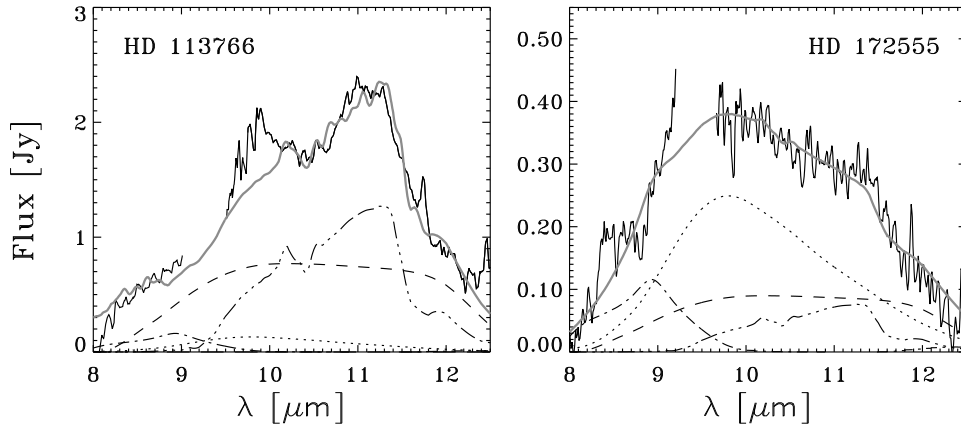


Figure 4.19: Left panel: Decomposition into dust components for HD 113766. Right panel: Similar analysis for HD 172555. The different linestyles represent small amorphous olivine (dotted), large amorphous olivine (dashed), silica (SiO_2 , dash-dotted) and crystalline forsterite (dash-three dots).

tures (Malfait et al. 1998b), just like those observed in HD 113766. Bouwman et al. (2001) analysed their spectra and concluded that both reference objects were sources of highly processed dust, given their high mass-ratios of forsterite. However, contrary to the forsterite- SiO_2 correlation they generally found for HAeBe stars (an increasing amount of forsterite is accompanied by an increasing amount of SiO_2 , which follows naturally from the thermal annealing process), these two objects seem to lack SiO_2 , that we also observe in HD 113766. It is thus unlikely that thermal annealing caused the observed crystalline silicates in these objects. As an explanation, Bouwman et al. (2001) suggested that the crystalline silicates were rather 'second generation' dust from the destruction of highly differentiated large parent bodies. Probably, HD 113766 is also host to such 'second generation' material, which might point to the presence of a planet orbiting this star, causing planetesimal-sized bodies to collide. HD 113766 may thus be a promising target for exoplanet searches.

In Fig. 4.20, lower panel, we also compare HD 113766 with the HAe star AB Aur, which has a very small amount of processed silicates. The peak around $10 \mu\text{m}$ is caused by *amorphous* silicates, while the emission from *evolved* silicate grains (upper and mid panel) is most prominent around $11.3 \mu\text{m}$ (cf. Sect. 4.3 and Bouwman et al. 2001). The spectral behaviour of other HAeBe stars lies between these two extremes.

- The SED of **HD 172555** appears stellar until $8 \mu\text{m}$, where the excess emission starts. A decomposition of the spectrum shows that small amorphous olivine grains are dominant, but larger sized olivine together with a smaller amount of SiO_2 and crystalline forsterite are present as well. The dust around this object appears quite young, i.e. unprocessed, when compared to HD 113766 which has a similar age. Although the unknown emission around $9.3 \mu\text{m}$ was seen in data

Table 4.10: Mass ratios derived from the model fits to the N-band spectra: large to small amorphous olivine ($m_{2.0}/m_{0.1}$), crystalline to amorphous silicates ($m_{\text{forst}}/m_{\text{sil}}$) and SiO_2 to silicates ($m_{\text{SiO}_2}/m_{\text{sil}}$).

Object	$m_{2.0}/m_{0.1}$	$m_{\text{forst}}/m_{\text{sil}}$	$m_{\text{SiO}_2}/m_{\text{sil}}$
HD 113766	12.0	0.39	0.03
HD 41511	1.0	0.05	0.09
HD 172555	0.7	0.09	0.09

from different runs and obtained under good observing conditions, we do not claim it as a new dust feature here due to its proximity to atmospheric bands. Observations with space-based instruments should be able to clarify this issue.

- **HD 207129** shows a stellar spectrum between 8 - 13 μm . Excess emission starts around 20 μm .

Post-main sequence objects

- In the CS dust of **HD 41511** both small and large amorphous silicates dominate, while there is a smaller amount of SiO_2 and crystalline silicates. The CS dust composition is actually quite similar to that of the much younger object HD 172555. However, as HD 41511 is in its post-MS stage, the dust was probably condensed from outflows of the central star and subsequently processed.

4.4.6 SIMBA measurements

At millimeter wavelengths, the emission from our Vega-type candidates can safely be assumed as optically thin and therefore proportional to the total disk mass. The mm measurements are therefore an excellent tool to derive the disk masses. For optically thin dust emission, the following expression can be used:

$$M = \frac{F_\nu d^2}{\kappa_\lambda B_\nu(T)}, \quad (4.8)$$

with F_ν and d as the mm flux and the target's distance, respectively. $B_\nu(T)$ represents the blackbody intensity which in the Rayleigh-Jeans limit equals $\frac{2kT}{\lambda^2}$. The assumed opacity κ_λ is the main uncertainty when deriving the disk mass. For consistency with previous works we use a mass absorption coefficient of $\kappa_0 = 1.7 \text{ cm}^2\text{g}^{-1}$ at 850 μm (e.g. Sylvester et al. 2001). This scales into $\kappa_\lambda = 1.2 \text{ cm}^2\text{g}^{-1}$ at 1200 μm using

$$\kappa_\lambda = \kappa_0 \left(\frac{\lambda_0}{\lambda} \right)^\beta \quad (4.9)$$

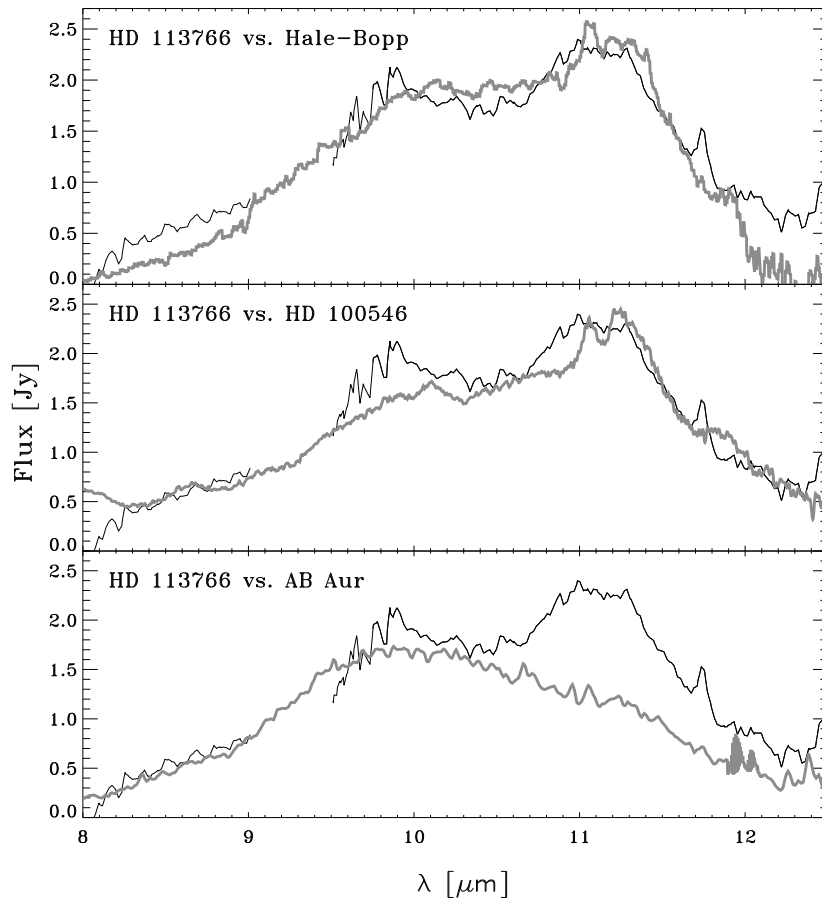


Figure 4.20: Comparison of HD 113766 (*thin curve*) with comet Hale-Bopp and the Herbig Be star HD 100546 (both scaled in *y-direction*). The resemblance is remarkable and demonstrates that HD 113766 has similar dust characteristics as those objects. In contrast, AB Aur, a young H Ae star with very little processed dust is shown in the bottom panel.

and an opacity index $\beta = 1$ following Mannings (1994) and Sylvester et al. (2001). This mass estimate is only a measure of the mass contained in grains radiating at mm wavelengths, while larger particles and large-sized bodies are invisible.

Another uncertainty in Eq. (4.8) is the mm dust temperature of Vega-type disks. Sylvester et al. (2001) applied a value of 30 K, while the four prototype Vega-like disks (β Pic, Fomalhaut, Vega and ϵ Eri) appear to have dust temperatures between 70 and 100 K (e.g. Sheret et al. 2004). If our objects were detected at various sub-mm and mm wavelengths, the dust temperature profile as a function of the distance to the star could be obtained from numerical modelling. Zuckerman & Song (2004) derived temperatures from IRAS data for some of our targets, but these may not correspond to the grains emitting at mm wavelengths. Therefore we will assume a mm dust temperature of 50 K and, for comparison, re-calculate the disk mass of the four prototype Vega-disks with this value. For their actual temperatures and dust masses see Sheret et al. (2004).

Table 4.11: (1) Upper limits for circumstellar dust masses obtained from our measurements at 1200 μm and assuming a $T_{\text{dust}} = 50$ K. HD 40932 was not considered, since the TIMMI2 spectra together with the SED had shown the non-existence of CS matter. (2) Reference dust masses re-calculated with $T_{\text{dust}} = 50$ K. See Sheret et al. (2004) for their actual masses.

Object	M_{moon} (50 K)	Ref.
HD 10647	< 6	(1)
HD 113766	< 345	(1)
HD 172555	< 25	(1)
HD 207129	< 4.5	(1)
β Pic	15.5	(2)
Fomalhaut	2.5	(2)
Vega	1.1	(2)
ϵ Eri	0.15	(2)

Since the mm-fluxes in Table 4.9 are all upper limits, we can only derive an upper limit for the disk masses of our sources. The disks in this subsample are still spatially unresolved, so the parameters grain size, disk radius and mass cannot be obtained simultaneously from modelling the far-IR to mm SED. Even our grain size estimation from fitting the mid-IR spectra is not helpful in this respect, since grains of different size may dominate the emission at those wavelengths.

The derived dust mass limits are shown in Table 4.11 together with re-calculated masses of the four prototype Vega-disks. All values are given in lunar masses with $M_{\text{moon}} = 3.7 \times 10^{-8} M_{\odot} = 7.3 \times 10^{22}$ kg. Sylvester et al. (2001) note that mm dust masses for T Tauri stars lie in the range of $1 - 40 \times 10^{-5} M_{\odot}$ ($\approx 0.3 - 11 \times 10^3 M_{\text{moon}}$) and Herbig Ae stars between $5 - 30 \times 10^{-5} M_{\odot}$ ($\approx 1.4 - 8 \times 10^3 M_{\text{moon}}$, although some lower-mass HAe disks are also known). From the derived upper limits we infer dust masses for our targets below $350 M_{\text{moon}}$, while for most of these objects the mass lies substantially below this value. The observed dust mass limits are thus in agreement with their Vega-type status.

4.4.7 Summary and conclusions

We studied N-band spectra of seven stars, known or suspected to have a circumstellar disk, and analysed their dust composition by fitting the observed spectra with known emission features from different dust species which are commonly found in CS disks. The Vega-type nature of HD 10647, HD 38678, HD 113766, HD 172555 and HD 207129 was confirmed, but we did not find any CS material around HD 40932 and reject it as a Vega-type candidate.

In our sample of five Vega-type stars only the youngest ones show an excess at 10 μm . For the other sources, the excess starts at longer wavelengths, which can be best explained by clearing of the inner disk as expected by theory (cf. Sect. 4.4.1). HD 113766

and HD 172555 are thus the only two stars in our sample which are transitional objects between the young (age < 10 Myr) stars – where planet formation could still be on-going and which still possess a lot of warm dust – and the older (age > 50 Myr) Vega-type stars that only show cold dust and thus a far-IR excess.

The biggest surprise in our sample is HD 113766, since such a feature-rich spectrum was never observed before for a Vega-type object. The analysis of its dust composition reveals highly processed dust similar to that in comet Hale-Bopp and the Herbig Be star HD 100546. It is – to our knowledge – the first time that such highly processed dust was found around a main-sequence object. The lack of SiO₂ suggests that the dust may be second generation, which might further hint at the presence of a planet disturbing the orbits of smaller bodies, causing them to collide with each other. The large resemblance of the dust around HD 113766 to that found in comets and interplanetary dust particles in our own solar system (IDP; Bradley 2003) suggests that we might see the early stages of our solar system by observing this object.

In contrast, small amorphous grains dominate the disk of HD 172555 (which is of comparable age to HD 113766), suggesting that the dust around HD 172555 is probably still first generation. This is further supported by the presence of a small amount of SiO₂ *and* forsterite, pointing to thermal annealing in the disk of this object. Around the post-MS star HD 41511 only a small amount of processed dust is found, which is expected if the dust is being condensed in the outflow of this evolved object.

We wonder why for HD 113766 and HD 172555, despite their prominent mid-IR features (revealing a substantial amount of warm dust), no significant excess at longer wavelengths was detected (including IRAS far-IR photometry). This means that these objects may possess only a very small amount of cold dust or a truncated disk. According to their age (between 10 and 20 Myr), these targets constitute a class of stars where the formation of planet(esimal)s – if they would take place – should just be finished. Is it possible that, besides the inner clearing, the cold dust in the outer regions is also removed? In case of HD 113766, one option is that the disk was truncated by its companion. In both objects, it might eventually also be a giant planet, located in the outer regions of the disk, which plays a role in causing the cold dust to disappear. A larger sample of stars with ages around 10 - 50 Myr should be examined with more sensitive telescopes and higher spatial resolving power to answer these questions.

Chapter 5

Millimeter observations

5.1 Technical introduction

5.1.1 The SEST

We carried out the mm observations at the Swedish-ESO Submillimeter Telescope (SEST), a 15 m radio dish operating in the frequency range of 70 - 365 GHz. It was constructed in 1987 at La Silla Observatory on behalf of the Swedish Research Council and the European Southern Observatory (ESO). Operation of the telescope ended in August 2003. Different from the previous cameras described in this work, observations with radio telescopes can be carried out during night and day.

5.1.2 Observing with SIMBA

SIMBA (SEST IMaging Bolometer Array) is a 37-channel hexagonal bolometer array operating at 1.2 mm wavelength. The telescope's half power beam width (HPBW) at this wavelength is about $24''$, indicating the smallest possible spatial resolution.

The following acquisition and calibration modi of SIMBA must be distinguished:

- Pointing measurements are necessary to determine the appropriate offset correction to the given telescope coordinates. These misalignments are caused by the influence of the ambient conditions on the dish, like irradiation by the Sun or the air temperature. About once a month a regular pointing run is scheduled to check the telescope alignment. Each observer should perform additional pointing corrections after sunset and sunrise by referring to bright pointing sources with known coordinates to correct for the change in the day/night ambient conditions.
- Focusing is required to (1) achieve the best spatial resolution and (2) to provide the highest possible signal-to-noise ratio at the source's center. This is achieved by moving the position of the secondary sub-reflector by typically less

than 1 mm. The telescope focus should be checked several times per night, at least after sunset and sunrise.

- With skydip measurements the obtained data can be corrected for atmospheric extinction. In fact, not the sky extinction but its emission is measured, implying a blackbody behaviour (emission = absorption). The observer can select an azimuth position for the telescope pointing, while the skydip measurements are performed at six positions on the sky with different elevations corresponding to a linear increase in airmass. The sky absorption (resp. emission) as a function of airmass can be described by

$$S = S_0 \exp\left(-\frac{\tau_0}{\sin h}\right), \quad (5.1)$$

where S_0 is the unextinguished flux, S the measured flux, τ_0 the zenith opacity and $\frac{1}{\sin h}$ the airmass at the elevation h . The unknown opacity τ_0 can thus be derived from a fit to the skydip measurements. This value is later used during the data reduction when the source fluxes are corrected for atmospheric extinction. Opacities at the SEST typically range between $\tau_0 = 0.1$ and 0.4 for $\lambda = 1.2$ mm. To consider for atmospheric variations, skydips should at least be performed each two hours.

- On-off measurements are scientific exposures and constitute an alternating series of integrations on the source and the sky background. Both signals are subtracted from each other to remove the sky emission. At the SEST no chopping of the secondary sub-reflector is done, instead the offsets are performed by nodding the telescope.
- With SIMBA a new imaging mode was introduced: fast mapping. SIMBA allows a variety of map sizes and scan speeds, although a speed of $80''/s$ is most frequently used. Scan length is the extend in scanning direction, which is azimuth, while the map width is perpendicular to this. The software calculates the number of necessary scans according to the scan separation, which is set to $8''$ by default (approx. one third of the telescope's HPBW). To allow a good coverage of the 37 bolometer channels, map sizes for a point-like source may not be smaller than $480'' \times 240''$, corresponding to 4.5 minutes of observing time. Standard map settings use scan lengths in azimuth between $600''$ to $1600''$ (this value may, in principle, be increased arbitrarily). The typical root mean square (rms) noise in one map is about 40 mJy. During excellent weather conditions this may improve to 30 mJy. Each map is automatically centered around the target's position and the telescope starts the scan at the map's lower left corner. To increase the integration time, several maps can be performed consecutively and co-added. The field of view (FOV) rotates during long observations due to the horizontal mounting of the telescope and the scans in azimuthal direction.

5.1.3 Concept of data reduction

Data obtained with SIMBA are stored in the FITS data format but need to be converted with a program called *Simbaread* prior to be reduced with data analysing programs. The data flow from SIMBA is typically 1 MB per minute of integration time.

This is the concept of reducing SIMBA bolometer data:

1. Conversion: The raw FITS file of a map must be converted before being reduced with any reduction software. *Simbaread* has been developed for this purpose.
2. Baseline fitting: This can be described as setting all detector signals of the bolometer array to a comparable zero point offset.
3. Despiking: Spikes may originate from cosmic rays or electronic discharges and must be eliminated as they can cause artificial noise levels, mimic a real emission feature or modify the actually measured flux of a source.
4. Deconvolution: The electronics of the pre-amplifier and the bolometer behave like an electric oscillator. As a result, the fast scanning mode creates signal shapes with a negative dip (see Fig. 5.1). These must be deconvolved with a filter function matching the electronic design.
5. Sky noise reduction: Atmospheric fluctuations contribute largely to the noise. Since the majority of the bolometer channels should experience the same changes in the flux, this correlated noise can be eliminated from the data, leading to an increase of the signal-to-noise ratio.
6. Gain elevation correction: The telescope dish experiences deformation from the optimal shape by gravitational influence, depending of the elevation it points at. This can change the actually measured intensity and must be corrected for.
7. Opacity correction: The measured source flux is largely affected by the atmospheric extinction which depends (1) on the airmass the signal had passed through the atmosphere and (2) the zenith opacity τ_0 as an indication of the overall atmospheric extinction. The latter one is obtained from the skydips described above. According to Eq. (5.1) and the airmass of observation, the intrinsic source flux can be restored.
8. Map creation: Finally, a map is created from the individual channel signals and consecutive maps can be co-added. The coordinate system is transformed from horizontal to equatorial. A final, co-added map of a point source is shown in Fig. 5.2.
9. Calibration: The counts must be transformed into physical units. To obtain the conversion factor, planet maps (e.g. Uranus, Mars) are frequently used, since their intensities are easy to obtain. However, secondary calibrators like quasars are also common, although their flux may be variable. The planets' intrinsic emission is fairly stable and a function of the surface temperature. Uranus is the most reliable source for mm flux calibrations. Jupiter has a peculiar strong emission, while the rings of Saturn may alternate its flux according to their in-

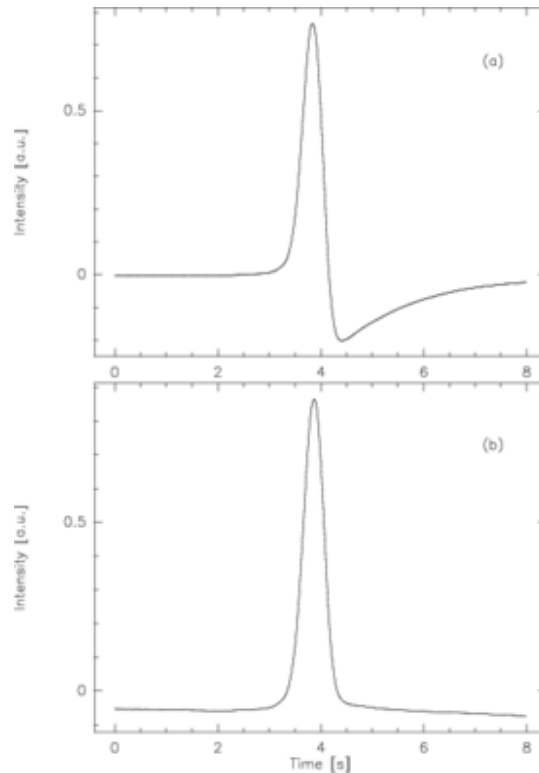


Figure 5.1: A signal measured by an individual detector channel is displayed: the bolometer electronics create a band pass which modifies the actual signal (a). The deconvolution restores its original shape (b). (Image credit: Reichertz et al. 2001)

clination. Mars is also frequently used, however, a global sandstorm may lead to wrong flux estimates. The subprogram *Planet* in MOPSI provides the planet surface temperature and derives the flux by applying models for the various planetary atmospheres. The user has to insert only the topocentric distance in AU to the planet, as the variable distance changes the signal intensity. All further parameters are obtained from the FITS file currently loaded in MOPSI. Calibrator maps on their part must be reduced in a slightly different way: no despiking and no skynoise reduction should be applied for these bright sources (cf. below).

The actual reduction steps – especially the despiking and skynoise reduction – will depend whether the source is compact or extended, faint or a rather strong emitter. Despiking can clip off the peak of a strong signal. For extended or very strong sources an improper search radius to correlate the channels in the skynoise reduction can reduce the intensity of the source.

Our SIMBA data were reduced with MOPSI, a software developed and maintained by R. Zylka (IRAM Grenoble). For a short introduction to MOPSI please see the Appendix in Chini et al. (2003). Most of the reduction steps described above can be performed by a single MOPSI script.

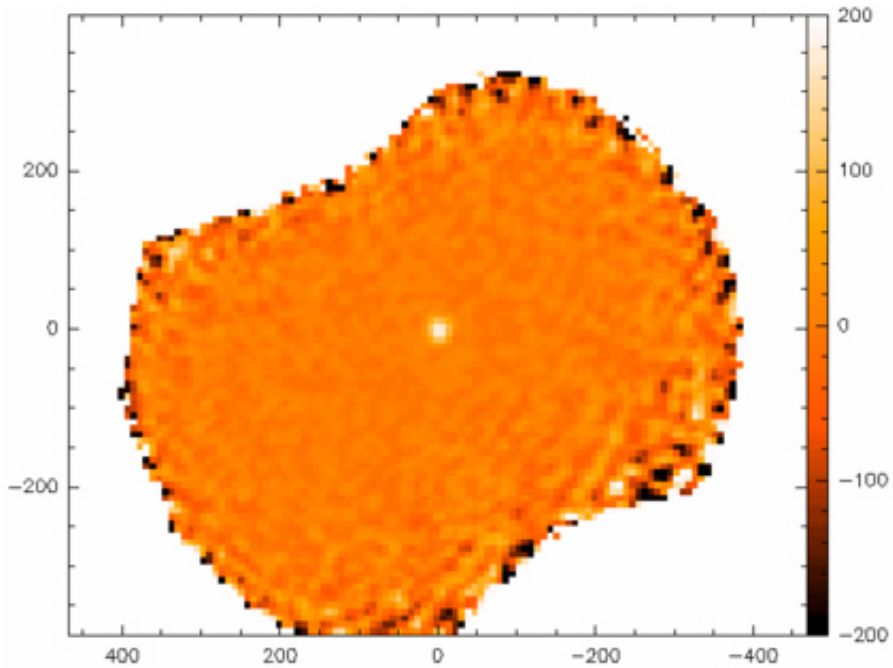


Figure 5.2: A typical SIMBA map of a point source (here: MP Mus) as example. Since several individual maps taken at different times were co-added, a rotation of the field of view can be seen. In such a case the noise naturally increases towards the margins of the map, as is recognisable here.

5.2 SIMBA's view of the ϵ Eri disk

We present the first observational confirmation for an extended circumstellar dust disk around ϵ Eri. The observations were obtained with the bolometer array SIMBA at the 15 m radio telescope SEST in Chile and measure the dust continuum at 1.2 mm. The emission, with a total flux of 21.4 mJy and a rms of 2.2 mJy/beam, is resolved to a deconvolved size of $27''.4$ which corresponds to 88 AU. No clear indication for a ring-like disk structure is seen, possibly also due to the telescope's large beam width of $24''$. Models of the object's spectral energy distribution from IR to mm-wavelengths show that the emission can also be explained by a simple disk model. We further demonstrate the strong influence of noise and propose to be cautious with interpretations of the ring substructure.

5.2.1 Introduction

Photometric measurements with the IRAS satellite (Aumann 1988) provided first hints for dust around the ~ 800 Myr old star ϵ Eri, a K2V dwarf at 3.22 pc distance to the Sun. From varying sub-mm flux densities in single-beam observations with different beam sizes (Chini et al. 1990, Chini et al. 1991, Zuckerman & Becklin 1993), an ex-

Table 5.1: Fluxes of ϵ Eri used in this work. The mid-IR IRAS fluxes contain also contributions from the stellar continuum. In the model SEDs in Fig. 5.3 this is separated from the dust emission.

Wavelength [μm]	Flux [mJy]	Error	Reference
12	9520	4 %	IRAS
25	2650	6 %	IRAS
60	1660	8 %	IRAS
100	1890	9 %	IRAS
450	185	103 mJy	Greaves (1998)
850	40	3 mJy	Greaves (1998)
1200	21.4	5.1 mJy	this work

tended – possibly ring-like – disk structure was assumed. In SCUBA observations at 850 μm Greaves et al. (1998) found the dust emission peaking in a ring-like distribution between 35 - 75 AU distance from the star. The central cleared region and an asymmetrical substructure in the ring were explained by the influence of orbiting planets. Now a planet with a semi-major half axis of 3.4 AU is known (Hatzes et al. 2000), which for more than a decade was controversial because of the star’s high chromospheric activity. Quillen & Thorndike (2002) explained the ring substructure with a further hypothetical planet at 40 AU distance. CO line observations at the Swedish-ESO Submillimeter Telescope (SEST) concluded that the disk of ϵ Eri is likely devoid of any gas (Liseau 1999). With ISO no features from dust were found in mid-IR spectra between 6 and 12 μm , and in maps at 60 and 90 μm no resolved emission was seen (Walker & Heinrichsen 2000). A partially resolved region in IRAS data, quoted by some authors, was thus not confirmed. Several attempts to reveal the disk (in scattered light) with coronagraphic imaging at near-IR and optical wavelengths have been tried without success, including HST observations. Recently, Li et al. (2003) calculated a disk model from the IR to sub-mm spectral energy distribution (SED) of ϵ Eri, but different disk and grain parameters were used than in our simulations. Furthermore, our calculations now also include observations at 1.2 mm. An overview of the fluxes used in this work is given in Table 5.1.

We present the first observational confirmation of an extended dust disk around ϵ Eri found with the SEST Imaging Bolometer Array (SIMBA). With results from numerical simulations for the target’s SED we set constraints on dust properties and discuss whether a continuous disk with an inner radius given by the dust sublimation temperature could be considered alternatively.

5.2.2 Observation

The observations of ϵ Eri were obtained in July 2003 with the 37-channel bolometer array SIMBA at the SEST in La Silla (Chile) using the fast scanning mode at 250 GHz ($\lambda = 1.2$ mm). Skydips were taken every 2 to 3 hours to correct for the atmospheric

zenith opacity, which was between $\tau_0 \approx 0.23$ and $\tau_0 \approx 0.37$. We followed the SEST pointing model (rms $\sim 2''.5$) and checked the telescope pointing regularly. No significant deviation from the pointing model was seen. The flux calibration is based on observations of Uranus. In total, 180 maps of ϵ Eri were integrated which correspond to a total on-source time of ~ 15 hours.

Data reduction was performed with MOPSI and included despiking, baseline fitting, suppression of the correlated sky noise, opacity and gain-elevation correction as well as co-adding the 180 single maps to a final one, which is shown in Fig. 5.4. The residual root mean square error (rms) amounts to 2.2 mJy/beam.

Observing at 1.2 mm with the 15 m dish of the SEST results in a nominal beam size of $24''$. This value can slightly vary with the elevation and other authors occasionally report $23''$ or $25''$. In principle, the beam size can be derived from a point source like, e.g., the planet Uranus. Averaging over various telescope positions we obtained a beam width of $24''.2 \pm 0''.2$. The resolved emission of ϵ Eri can be fitted by an extended, circular Gaussian intensity distribution with a full width half maximum (FWHM) of $36''.4$. This fit and its centering is achieved with a routine in MOPSI. Relative to the beam width we resolve the dust emission around ϵ Eri consistent with a deconvolved total extent of $27''.4$, corresponding to 88 AU. An elliptical shape of the intensity distribution – indicating an inclination of the disk – cannot be excluded, but is not apparent from our measurements. Greaves et al. (1998) reported $i = 25^\circ$. At 1.2 mm, after subtracting a photosphere contribution of 0.9 mJy, the total disk flux amounts to 21.4 mJy with a peak flux of 9.7 mJy/beam and 2.2 mJy/beam noise. As can be seen in Fig. 5.4 (central panel), the peak of the Gaussian lies $7''$ southwest of the star. This is not necessarily a physical effect, since the accuracy of the centering routine is within $5''$ (corresponding to 2.5 pixel in this figure).

5.2.3 Numerical simulations

The disk model is derived from the target's SED with the fluxes shown in Table 5.1. Since especially the mid-IR fluxes contain a contribution from the stellar continuum, this is treated separately in the simulated SEDs.

We apply a model of an optically thin disk with the simple radial density profile $n(r) \sim r^{-1}$ (for the calculation of the dust temperature distribution see Wolf & Hillenbrand 2003, Eq. 5). The following stellar parameters are used for ϵ Eri: $T_\star = 4700$ K, $R_\star = 0.8 R_\odot$ and $L_\star = 0.33 L_\odot$ (e.g. Soderblom & Däppen 1989). We select a circular disk with an extension from $R_{\text{in}} \approx 0.025$ AU (corresponding to the radius given by the dust sublimation temperature) up to the observed $R_{\text{out}} = 88$ AU. Other choices for the inner disk radius and their consequences are discussed in the next chapter.

Spherical homogeneous dust grains were used with radii a according to a size distribution $n(a) \sim a^{-3.5}$. This describes the equilibrium size distribution resulting from a collisional cascade of dust (Tanaka et al. 1996) and has often been used for the interstellar medium (ISM) and modelling of circumstellar disks. The best approximation to the observed SED is obtained for a minimum grain size $a_{\text{min}} = 8 \mu\text{m}$ which is displayed in Fig. 5.3. SEDs for $a_{\text{min}} = 4 \mu\text{m}$ and $a_{\text{min}} = 16 \mu\text{m}$ are shown for comparison.

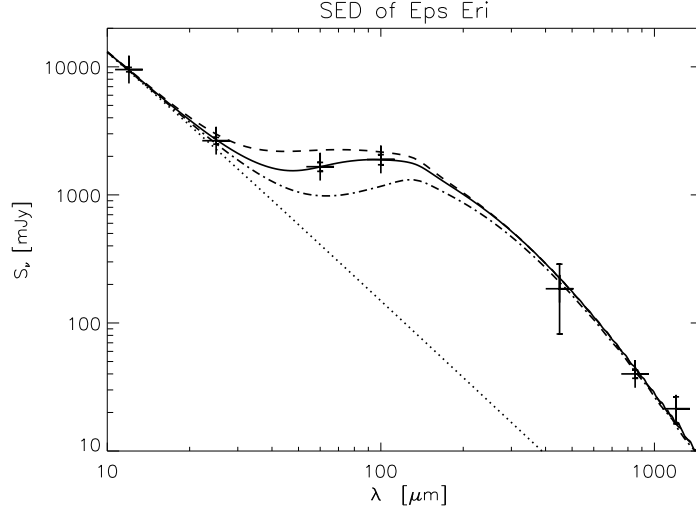


Figure 5.3: Modelled SED of ϵ Eri. The simulations were calculated with a grain size distribution and varying minimum grain size: $a_{\min} = 4 \mu\text{m}$ (*dashed line*), $a_{\min} = 16 \mu\text{m}$ (*dash-dotted*), $a_{\min} = 8 \mu\text{m}$ (*solid curve*, best fit). The stellar photosphere is shown as a dotted line.

We use an upper grain size of 1 mm. The disk mass, given in the next section, refers to this upper size limit, since we have no direct observational hints for cm-sized grains. Simulations are performed with a dust mixture deduced from the ISM: 62.5% silicate grains (according to Draine & Lee 1984 and Weingartner & Draine 2001), mixed with 37.5% graphite. The dust grain density amounts to $\rho(\text{silicate}) = 2.7 \text{ g cm}^{-3}$ and $\rho(\text{graphite}) = 2.24 \text{ g cm}^{-3}$.

5.2.4 Discussion

Disk temperature and dust mass

Submillimeter observations probe the cold dust towards the outer part of the disk. From a fit to the observed fluxes between far-IR and mm-wavelengths we determine for the cold dust component a temperature of 50 K using $\beta = 0$ and $\kappa(1.2 \text{ mm}) = 1.7 \text{ cm}^2 \text{ g}^{-1}$. With the numerical simulations described above we obtain a dust mass of $5.2 \times 10^{-9} M_{\odot} = 1.7 \times 10^{-3} M_{\oplus}$, which lies about a factor of three under the lower mass limit given in Greaves et al. (1998).

Dust ring or a continuous disk

We are able to explain the observed SED with a simple disk model, an inner disk radius given by the dust sublimation temperature and a minimum of free parameters, i.e. without further assumptions. However, we do not exclude other disk models. With the limited resolution of the SEST beam only a very sharp ring would have been de-

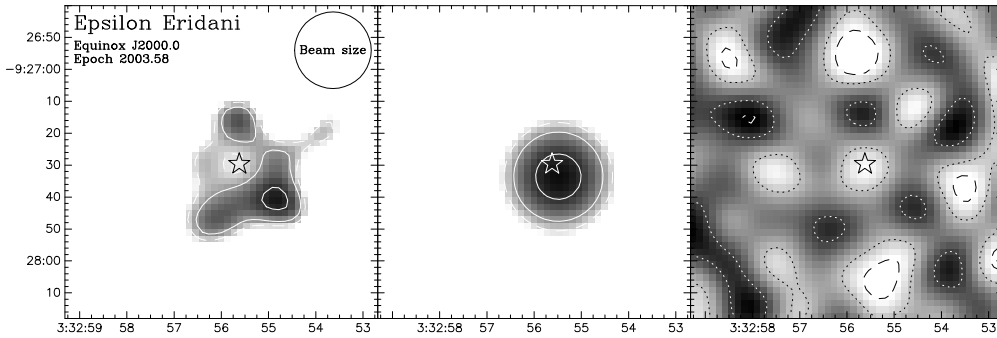


Figure 5.4: Similar to the SCUBA observation our image sampling is $2''$. We find a central cavity and the emission peaking in certain spots along a ring-like distribution (*left panel*). However, subtracting a circular Gaussian intensity distribution with a FWHM of $36''.4$ (*central panel*) only leaves residues of pure noise (*right panel*). Thus we conclude that the substructure in our map was likely caused by remnant noise. The star marks the location of ϵ Eri, corrected for its proper motion (-976.36×17.98 masec/year, cf. the SIMBAD database or Perryman et al. 1997). In the left and central panel the intensity is scaled logarithmically from 5 to 10 mJy, solid contours represent regions with an accuracy of 3 resp. 4σ ($\text{rms} = 2.2$ mJy/beam), while the dashed contour (which nearly coincides with the outer margin of the grey-scaled region) corresponds to 2.5σ . The right panel shows -2σ resp. $+2\sigma$ as dashed contours and $\pm 1.5\sigma$ are symbolised by dotted lines.

tectable. Even for SCUBA the reported central cavity is close to the resolution limit. From modelling the observed SED no statement can be made to which extent the inner disk region may be depopulated of dust. Due to the large parameter space in any dust disk model (disk density profile, dust grain radii, grain size distribution, dust mineralogy, grain shapes, etc.) several solutions may exist to interpret the observed SED. Li et al. (2003) find their model in good agreement with Greaves et al. (1998) for disk radii ≥ 28 AU, while an additional 'zodiacal' dust component would be required to explain the possible emission from the inner parts of the disk. This inner region was not clearly resolved by previous mid- and far-IR satellite cameras, but can be better studied with upcoming Spitzer observations (see Li et al. 2003 for a discussion on this). An alternative approach would be interferometric observations with the IRAM Plateau de Bure Interferometer operating at 1.3 mm wavelength with a resolution down to $1''$.

Influence of noise on the observed disk substructure

Fig. 5.4 (left panel) shows our final co-added map of ϵ Eri. The pixel sampling with $2''$ is justified because of SIMBA's image sampling of 15 ms in azimuthal scan direction. With $80''/\text{s}$ scanning speed this results in a spatial sampling of $1''.2$. In right ascension and declination we obtain a similar value due to the large coverage of maps taken at different phase angles. Our final image resembles a disk with a cleared central region and substructures in the ring. However, we can show that these details are most likely caused by remnant noise. The resolved emission of ϵ Eri can be fitted by an extended

Gaussian intensity distribution with a FWHM of $36''.4$ (central panel). A subtraction of this fit from the final map only results in pure residual noise, while a real central cavity should cause a clear negative peak after subtraction. The occurrence of a minimum exactly at the position of the star leaves speculations whether this is a contribution of a real gap. However, this minimum is even less prominent than the noise minima above and below the star's position. Similarly, the knots in the outer disk part can be explained by noise maxima. To verify this, we simulated a ring-like disk with artificial noise but without intrinsic ring substructures, and obtained a comparable result.

The knots in the SCUBA ring were attributed by some authors to be traps of dust due to orbital resonances of Jovian planets. However, most of these are smaller than the resolution of the SCUBA beam. We speculate that these structures may be explained similar to our observations.

5.2.5 Conclusions

Since several publications calculate planetary parameters from the knots in the ϵ Eri ring structure, we intended to perform the first confirmation of this disk shape. Our observation with the bolometer array SIMBA operating at 1.2 mm is the first verification of an extended disk around this star. However, these data do not provide clear indications for the previously reported ring substructure. In our case the knots can be explained with remnant noise effects. We are able to model the observed SED with a simple, gap-free disk, but do not rule out the existence of a possible central cavity.

Chapter 6

Summary and conclusion

We give here an overall summary of this work. For more detailed conclusions on the independent projects the reader is referred to Sect. 3.2.6, Sect. 3.3.4, Sect. 4.3.6, Sect. 4.4.7 and Sect. 5.2.5. The goal of this work was a multi-wavelength search for previously unknown circumstellar disks and an analysis of those disk candidate objects which were not characterised well in the literature. While our disk analysis was not constrained to certain stellar types and ages, most objects studied are old pre-main sequence stars and main-sequence objects.

1. **Coronagraphic imaging of circumstellar disks:** We aimed to discover new circumstellar disks with SHARPII+ / ADONIS focusing on a search around stars which were known to have planets. Our non-detections are in agreement with studies by other groups. No disk was ever detected in a known exoplanet system, although some false publications exist in the literature which are clarified now. Due to selection effects in the search for exoplanets, the parent stars are all solar-like with ages where any remnant disk already has disappeared. However, the opposite is true: some circumstellar disks were successfully searched for planets, e.g. in case of ϵ Eri (Hatzes et al. 2000) and HD 10647 (Mayor et al. 2003).

For the known disks in our sample the non-detections were caused by insufficient sensitivity and the intrinsic limitations of ground-based AO systems described in this work. We showed that for coronagraphy several instrumental features can mimic the existence of a disk. Indeed, some disk detections in the literature are premature publications (e.g. Trilling et al. 2000). Thus we propose that disk detections should always be followed by observations at other wavelengths (near-IR, mid-IR, mm) or using spectroscopy, before the disk is considered as real.

2. **A test of polarimetric differential imaging:** Dual-imaging techniques like polarimetric differential imaging (PDI) avoid many problems of coronagraphy. Two orthogonal polarisation states are observed simultaneously with a Wollaston prism. The difference image from these will contain only the polarised light of the real circumstellar disk. Although this method was shown to work for

HD 169142 (Kuhn et al. 2001) and TW Hya (Apai et al. 2004), we did not find a polarisation pattern in the four disks resp. disk candidate objects we observed. Possible explanations for this are discussed in Sect. 3.3.4. The detectability apparently depends on physical parameters still to be characterised, as other authors also report to see polarimetric features only for a minority of the sources within their promising target sample (Kuhn et al. 2001; Huéramo et al., personal communication). However, as details of PDI non-detections have not yet been published, we cannot relate this to our targets to conclude on the parameters which determine the detection feasibility. It seems that a prominent near-IR excess is the essential condition to find polarimetric emission. Also, unless saturation of the images is desired, the star-to-disk brightness ratio imposes limits on the detection sensitivity.

3. **Advances in mid-IR data reduction:** We presented a method to correct the chromatic and airmass dependent extinction for N-band spectra taken with the TIMMI2 camera. Our method allows to correct the atmospheric extinction and improves the spectrophotometric flux calibration to an unprecedented quality when the standard stars were observed at a very different airmass than the targets.

For ground-based mid-IR instruments no possibility of a reliable flatfield correction exists up to now. We show in Appendix A a method how TIMMI2 data, in principle, could be flatfielded. The resulting image is not always of better quality, depending on the meteorological conditions. No recommendation to observers is given at the moment to apply this technique.

4. **Mid-IR observations of circumstellar disks:** We discussed spectral energy distributions and N-band spectra of eight PMS stars (two Herbig stars, two T Tauri stars and four FU Ori sources) surrounded by a circumstellar disk, and analysed their dust composition by fitting the observed spectra with known spectral features of different dust species and PAHs. Strong PAH lines are found for HD 34282 but no silicate emission, which indicates that small silicates are strongly depleted in this disk. The most important result within this sample of PMS stars is the dust composition of HD 72106, a host of highly processed silicates, similar to those seen in solar-system comets. This target may thus be a good candidate for extra-solar planet searches. We also detected enstatite in HD 72106, which is a very rare finding in circumstellar disks and might point to rapid gas dispersal due to a higher luminosity of the central star. Processed dust is also found around the relatively old T Tauri stars (7 - 10 Myr) HD 98800 and MP Mus. For the FU Ori targets, we observe absorption features in three of the four cases, which is expected for objects embedded in optically thick material. One of the targets – BBW 76 – shows the silicate feature in emission and is likely less embedded.

Another sample of stars studied in the mid-IR consists of six main sequence stars and one post-main sequence object, all known or suspected to have a circumstellar disk. We analysed their dust composition in the same way as for the younger sample of PMS stars. The Vega-type nature of HD 10647, HD 38678, HD 113766, HD 172555 and HD 207129 was confirmed, but we did not find any circumstellar material around HD 40932 and reject it as a Vega-type candi-

date. The biggest surprise in this sample is HD 113766, since such a feature-rich spectrum was never observed before for a Vega-type object. Its dust appears to be second generation, which might hint at the presence of a planet disturbing the orbits of smaller bodies, causing them to collide with each other. The large resemblance of the dust around HD 113766 to that found in comets and interplanetary dust particles in our own solar system suggests that we might see the early stages of our solar system by observing this object. Small amorphous grains – probably still first generation – dominate the disk of HD 172555, although it is of a comparable age to HD 113766. Around the post-main sequence star HD 41511 a small amount of processed dust is found, which is likely condensed in the outflow of this evolved object.

It is tempting to consider the possibilities of mid-IR spectroscopy superior to the near-IR disk detection techniques, given our mid-IR findings for HD 113766, HD 155448 and MP Mus, whereas no insights in these objects were obtained by near-IR methods. However, the target samples for the near- and mid-IR overlap too marginally to permit a global comparison.

5. **Millimeter observations of ϵ Eri:** Several publications calculated planetary parameters from the knots seen in the ϵ Eri ring structure, considering these knots as dust being trapped in the resonance points of an orbiting planet. As the detection of these features had never been confirmed by independent observations, we studied this object with the bolometer array SIMBA at 1.2 mm and verified an extended disk around this star. However, we did not find the previously reported ring substructure. In our case these knots can be explained by remnant noise effects and we propose to not regard these as signatures of orbiting planets.

We consider it essential to verify astronomical observations prior to drawing fundamental conclusions thereof (see also Item 1). The new policy enforced at several large observatories to forbid the repetition of observations ('no duplication' policy) is not helpful in this regard.

Appendix A

Flatfield experiments with TIMMI2

A.1 Why are conventional flatfields not possible in the mid-IR ?

Different from the optical wavelength range and the near-IR (1 - 5 μm), no flatfields are made for observations at thermal wavelengths (10 - 20 μm). Techniques used to obtain flatfields at shorter wavelengths will fail in the mid-IR. A mid-IR 'dome flat' would saturate the detector because the screen is at room temperature. Simple sky frames in the mid-IR are dominated by fast fluctuations in the sky background and flatfields obtained from these will not be constant neither in time nor in spatial dimensions. Furthermore, data are not comparable if taken with different electronical read-out modes. Altogether, any possible TIMMI2 flatfield must comply with the following characteristics:

- be spatially close to the science object
- be very close in time to the science exposure
- taken with the same detector read-out mode
- of course, taken with the same filter settings

Therefore, for almost each science observation an individual flatfield would be required. In first tests, however, even within the shortest possible time between science object and calibration data, no good flats could be obtained.

A.2 The current observing situation with TIMMI2

All data at thermal wavelengths are obtained with chopping and nodding to eliminate the thermal background of the sky and telescope (see Sect. 4.1 for more information on this technique). As a result of this procedure, images reduced by the TIMMI2

pipeline or an equivalent observer's routine are already relatively flat. However, certain inhomogeneities persist. A point source often appears fainter in the lower half of the detector and the variations in the count rate over the detector array may amount up to 20%. These patterns show to some level a constant trend but are also variable in time, and therefore cannot be explained only by the individual pixels' response of the detector. Sky background variations and the atmospheric behaviour have a major impact on these features. This is the reason why the question of flatfielding mid-IR data up to now only has been solved for space based observations (Starck et al. 1999).

A.3 Basic ideas for creating a detector gain map

For optical detectors, variations along the detector array are mainly caused by dust on the detector or a remaining misalignment within the light beam, due to which the beam may hit the detector not exactly perpendicular. In the infrared, the different response of the detector array results from wide-range variations in the pixel sensitivity. Different from optical detectors each pixel is individually read out and the electronic is more difficult than in the optical. To determine the sensitivity of each single pixel, its response is typically measured in a sequence of images with different levels of illumination. For mid-IR observations this varying illumination can be achieved by the following ways:

- Observe the sky at different airmass. The background level increases with the distance from zenith when the telescope points at thicker atmospheric layers.
- Observation of varying, thin clouds. Their water content makes them 'hot', i.e. bright at thermal wavelengths. Natural variations in the clouds cause different brightness. Thick clouds, however, will saturate the detector immediately.
- Creating a flatfield from temporal background variations within the science exposure. This sounds difficult, but turned out to be the most promising approach.

In any brightness sequence, the median count rate over all pixel in each single exposure is compared to the count rate of an individual pixel. A linear fit to all pairs of these values (median of the image, count for a certain pixel) within the illumination sequence creates a response function for this single pixel. Ideally, the slope of this function should be close to 1. Pixel with a lower value react less on exposure to light than those with a higher value. Bad pixel are close to 0, hot pixel are much brighter than 1. Applying this to all pixel creates a gain map for the whole detector array. With this method variations in the sensitivity of the detector array can be identified. Dividing a raw image by this gain map would result in the corrected image, in principle. This works well for the near-IR, but for the mid-IR more sophisticated methods are necessary. The problem is that for TIMMI2 these gain maps appear to be highly variable with time.

A.4 Realisation of a mid-IR flatfield

A.4.1 Observation at different airmasses

Measuring the sky or a target at two or more different airmasses leads to a sequence of exposures with different brightness due to the increasing sky contribution with distance from zenith. A flatfield can be created as shown above. Its quality however will strongly depend on temporal and spatial atmospheric fluctuations during the observations. In our tests this flatfield could not be successfully applied to a science exposure obtained within these observations.

A.4.2 Clouds

Thin, varying clouds result in a perfect illumination sequence. However, another detector read-out mode has to be used for these observations. A flatfield obtained from these data is not compatible to the read-out mode for science observations.

A.4.3 Creating the flatfield from a science exposure

Due to background fluctuations within a science exposure, consisting of a sequence of co-added frames, also from these data an illumination sequence could be derived. Long-time exposures or those with larger background fluctuation have a better statistic in the fit of the pixel response. Only these exposures will result in a reliable flatfield.

The procedure is complex due to the spatial offsets for chopping and nodding. In the following we describe an *example* for a stellar point source observed in *four* nodding positions, i.e. two full nod cycles. For each nod position, the first chopping position is called the ON position (sometimes also called position 0). With OFF (or position 1) we specify the second chop. The number of video frames per nod be 1 in this case. Each chop and each nod position results in an individual flatfield, in our example this results in eight completely different flats. We found no correlation of flats from corresponding positions, modifications are statistical and time-dependant.

Dividing the science frame of each chop and nod position by the corresponding flatfield seems the nearest approach, but will result in corrupted data: the information of the star's position on the detector is still included in these flatfields, even though not directly visible. When dividing the frame of an individual chop and nod position by the corresponding flatfield, the resulting image is destroyed at the position where it actually should be corrected, i.e. the stellar surrounding. The following procedure avoids this and constitutes the best approximation for a TIMMI2 flatfield up to now:

- Take the arithmetic middle of the two flats from the same nod position in order to eliminate the star's position in the flatfield. Flats from different nod positions can be highly variable and may not be mixed. In the following, 'GM' denotes this average gain map per nod position:

$$GM_1 = (\text{GAIN}_{\text{NOD1 Off}} + \text{GAIN}_{\text{NOD1 On}}) / 2 \quad (\text{A.1a})$$

$$GM_2 = (\text{GAIN}_{\text{NOD2 Off}} + \text{GAIN}_{\text{NOD2 On}}) / 2 \quad (\text{A.1b})$$

$$GM_3 = (\text{GAIN}_{\text{NOD3 Off}} + \text{GAIN}_{\text{NOD3 On}}) / 2 \quad (\text{A.1c})$$

$$GM_4 = (\text{GAIN}_{\text{NOD4 Off}} + \text{GAIN}_{\text{NOD4 On}}) / 2 \quad (\text{A.1d})$$

- The following is the standard way to reduce one nod cycle of science frames (this is also performed by the TIMMI2 pipeline). Note that the sequence of nod positions does not correspond to AB AB AB AB, but instead the nodding is AB BA AB BA. With 'IMA' we denote a reduced frame obtained from the nod positions indicated as subindices:

$$\text{IMA}_{1,2} = (\text{NOD1 On} - \text{NOD1 Off}) - (\text{NOD2 On} - \text{NOD2 Off}) \quad (\text{A.2})$$

$$\text{IMA}_{3,4} = (\text{NOD3 On} - \text{NOD3 Off}) - (\text{NOD4 On} - \text{NOD4 Off}) \quad (\text{A.3})$$

$$\text{IMA}_{1,2,3,4} = \text{IMA}_{1,2} + \text{IMA}_{3,4} \quad (\text{A.4})$$

- For the best approach to a flatfielded TIMMI2 image, now perform the following calculations. 'IMA ff' signifies the flatfielded image:

$$\begin{aligned} \text{IMA ff}_{1,2} \\ = (\text{NOD1 On} - \text{NOD1 Off})/GM_1 - (\text{NOD2 On} - \text{NOD2 Off})/GM_2 \end{aligned} \quad (\text{A.5})$$

$$\begin{aligned} \text{IMA ff}_{3,4} \\ = (\text{NOD3 On} - \text{NOD3 Off})/GM_3 - (\text{NOD4 On} - \text{NOD4 Off})/GM_4 \end{aligned} \quad (\text{A.6})$$

$$\text{IMA ff}_{1,2,3,4} = \text{IMA ff}_{1,2} + \text{IMA ff}_{3,4} \quad (\text{A.7})$$

This approach can produce a kind of flatfield correction for data taken during high atmospheric variations or fair weather conditions. The calculations can be easily included in a personal reduction pipeline. On the other hand this method completely fails to flatfield good data. The worse statistics during the illumination sequence, when calculating the pixels' response function, is the reason for this.

The following section shows results from applying this technique to science data.

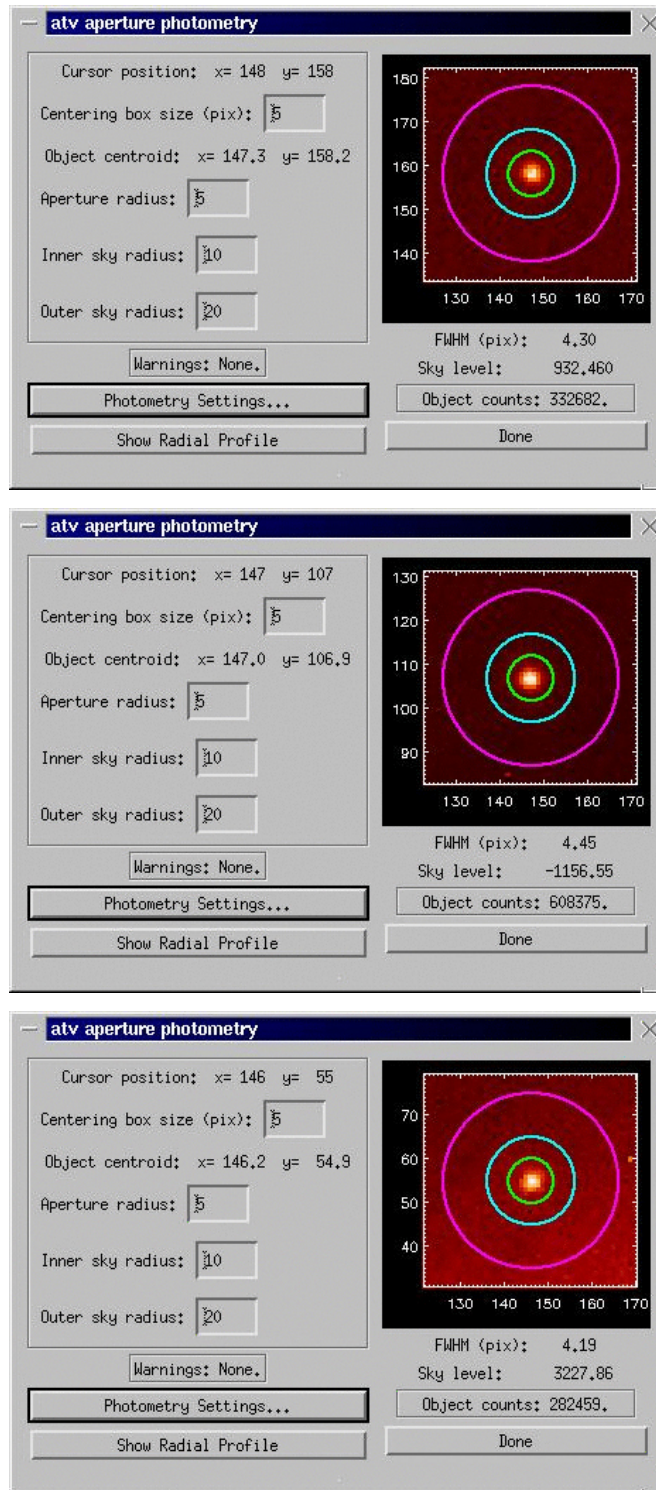


Figure A.1: Uncorrected TIMMI2 photometry at the upper source position (*top panel*), the central source position (*mid panel*) and lower source position (*bottom panel*). Inhomogeneities in the detector response can be recognised from the count values.

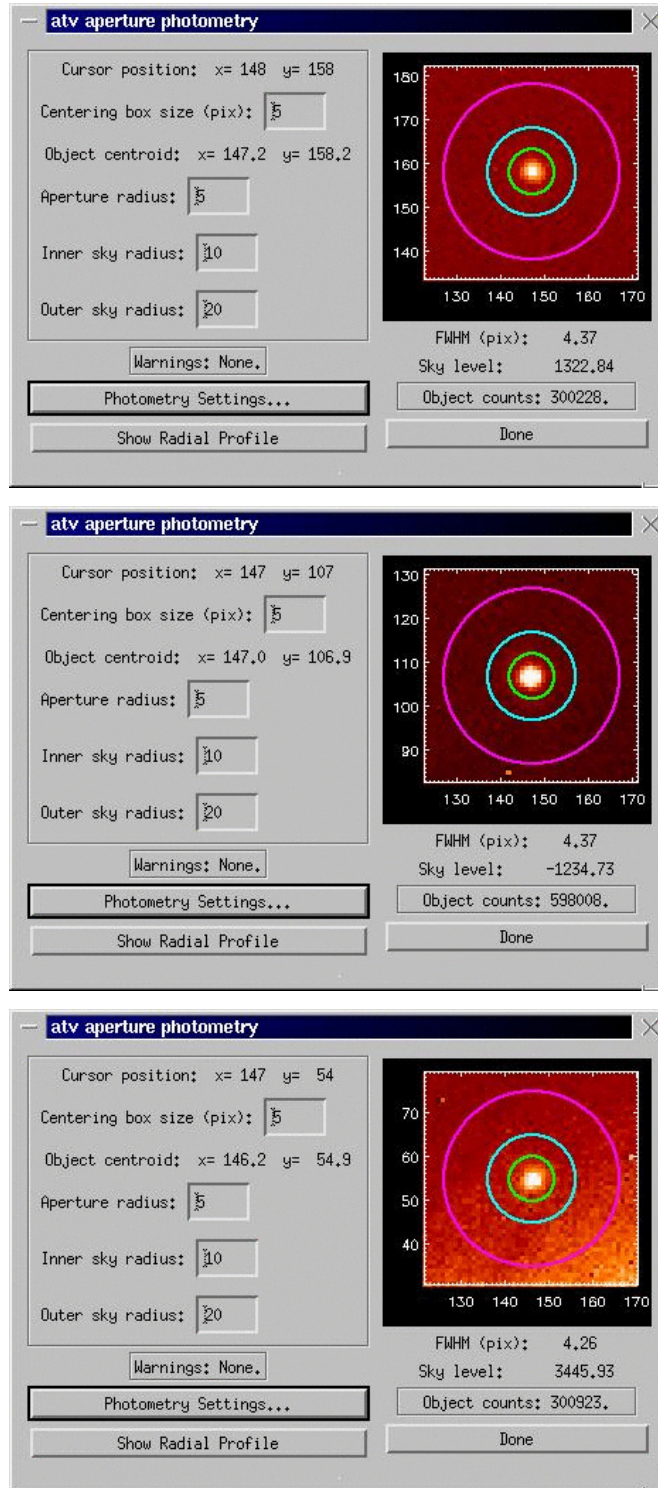


Figure A.2: Corrected TIMMI2 photometry after flatfielding, at the upper source position (*top panel*), at the central source position (*mid panel*) and the lower source position (*bottom panel*). The detector response is more equal.

A.5 Application to test data

A.5.1 Photometry before applying the flatfield correction

In the following we consider a triangular chop-nod sequence (cf. Sect. 4.1). Ideally, the source flux should be identical in the upper and lower position of the source. In the middle, the registered counts should be twice the absolute value of the upper resp. lower position.

However, as shown in Fig. A.1, in fact we have:

- upper position: 332 682 counts
- middle position: 608 375 counts
- lower position: 282 459 counts

A.5.2 Photometry after applying the flatfield correction

Following the above approach for a flatfield correction, we now get a much flatter detector response (see also Fig. A.2):

- upper position: 300 228 counts
- middle position: 598 008 counts
- lower position: 300 923 counts

A.6 Conclusions

For all ground-based mid-IR instruments no possibility of a reliable flatfield correction exists up to now. We have shown a method how TIMMI2 data in principle could be flatfielded. The resulting final image is not always of better quality, depending on meteorological conditions. No recommendation to observers can be given at the moment to apply the techniques presented here.

Appendix B

Acknowledgements

This work is based on observations collected at the European Southern Observatories La Silla and Paranal (Chile) under the observing programs 65.I-0098, 67.C-0240, 68.C-0070, 69.C-0073, 70.C-0468, 71.C-0001, 73.C-0001 and 73.C-0372. Our study made usage of the SIMBAD astronomical database and ADS, Strasbourg.

Sect. 3.2 was a cooperation with Dr. H. Bönhardt, Dr. E. Pantin, Dr. S. Els, et al. (A&A, 424, 613). Sects. 4.3 and 4.4 were carried out in collaboration with Dr. G. Meeus and Dr. M. Sterzik (A&A, in press). Sect. 5.2 was a joint project with Dr. M. Nielbock, Dr. S. Wolf, et al. (A&A, 414, L9). The ISO-SWS spectrum of Z CMa in Sect. 4.3.5 was kindly provided by B. Acke. We thank the ESO staff and telescope operators in La Silla and Paranal for their support during all observations.

I thank Dr. M. Sterzik, Dr. H. Bönhardt and Prof. T. Henning for guidance in my PhD work and Prof. I. Appenzeller, Prof. J. Wambsganß and Prof. R. Neumann for their participation in my PhD examination.

I am grateful to ESO Santiago and the MPIA Heidelberg for the funding of my PhD work.

Appendix C

Acronyms

ADONIS	Adaptive Optics Near Infrared System
AO	Adaptive Optics
CS	circumstellar
DIT	Detector Integration Time
ESO	European Southern Observatory
FOV	Field of View
FUOR	Star of FU Orionis type
FWHM	Full Width Half Maximum
HAeBe	Herbig Ae/Be Star
HPBW	Half Power Beam Width
IR	infrared
IRAS	Infrared Astronomical Satellite
ISO	Infrared Space Observatory
M2	telescope secondary mirror
MIDAS	Munich Image Data Analysis System
MOPSI	Mapping, On-Off, Pointing, Skydip, Imaging
MS	Main Sequence
ms	milli-second
Myr	Mega-year
M_{\odot}	Sun mass
M_{\oplus}	Earth mass
NACO	NAOS-CONICA
NAOS	Nasmyth Adaptive Optics System
OB	Observing Block
P2PP	Phase 2 Proposal Preparation
PDI	Polarimetric Differential Imaging
PMS	Pre-Main Sequence
PSF	Point-Spread-Function
rms	root mean square error
SDI	Simultaneous Differential Imager
SED	Spectral Energy Distribution
SEST	Swedish-ESO Submillimeter Telescope

SIMBA	SEST Imaging Bolometer Array
SIMBAD	SIMBAD Astronomical Database (http://simbad.u-strasbg.fr/Simbad)
SR	Strehl Ratio
S/N	Signal-to-Noise Ratio
TIMMI2	Thermal Infrared Multi-Mode Instrument
TNO	Trans-Neptunian Object
TTS	T Tauri Star
WFS	Wavefront Sensor
yr	year

List of Figures

1.1	Circumstellar disks at different stages of development	2
1.2	Definition of the Lada Classes	4
3.1	Principle of Adaptive Optics	10
3.2	Principle of the Shack-Hartmann wavefront sensor	11
3.3	Artefacts in coronagraphy (1)	18
3.4	Artefacts in coronagraphy (2)	19
3.5	Detection limits with ADONIS coronagraphy	23
3.6	S/N of simulated disk detections	24
3.7	Polarimetric pattern of TW Hya	26
3.8	The NACO triangle effect	30
4.1	The triangular chop-nod combination	34
4.2	The quadratic chop-nod combination	35
4.3	TIMMI2 conversion factors for photometry (N1)	39
4.4	TIMMI2 conversion factors for photometry (N8d9, N10d4)	40
4.5	TIMMI2 conversion factors for photometry (N11d9)	41
4.6	Test of our airmass correction	44
4.7	Young TIMMI2 targets: SEDs of PMS objects	51
4.8	Young TIMMI2 targets: SEDs of FUOR objects	52
4.9	Young TIMMI2 targets: spectra of PMS objects	53
4.10	Young TIMMI2 targets: spectra of FUOR objects	54
4.11	Dust grain emissivity in the mid-IR	55
4.12	Young TIMMI2 targets: dust emission features	57
4.13	Comparison of HD 72106 with the comets Halley and Hale-Bopp	58
4.14	Optical depth towards V 346 Nor, V 883 Ori and Z CMa	60
4.15	Mid-IR spectral shapes of V 346 Nor and Z CMa at different epochs	61
4.16	HD 41511: SED, spectrum and circumstellar dust emission	68
4.17	Older TIMMI2 targets: SEDs of Vega-type objects	69
4.18	Older TIMMI2 targets: spectra of Vega-type objects	70
4.19	HD 113766 and HD 172555: dust emission features	72
4.20	Comparison of HD 113766 with comet Hale-Bopp and HD 100546	74
5.1	Correcting the band pass feature in the bolometer signal	80
5.2	Typical SIMBA map of a point source	81
5.3	Model SED of ϵ Eri	84

5.4	SIMBA map of ϵ Eri	85
A.1	Inhomogeneities in the TIMMI2 detector response	95
A.2	TIMMI2 photometry after flatfielding	96

List of Tables

3.1	NACO imaging: available cameras and fields of view	13
3.2	Targets for ADONIS coronagraphy	15
3.3	Results from ADONIS observations	20
3.4	Targets for NACO differential polarimetry	28
4.1	Observing modes of the TIMMI2 camera	36
4.2	N-band extinction coefficients for La Silla	43
4.3	Test of our airmass correction (1)	45
4.4	Test of our airmass correction (2)	45
4.5	Targets observed with TIMMI2: young objects	48
4.6	Results for the young TIMMI2 targets	49
4.7	Dust mass ratios for the young TIMMI2 targets	56
4.8	Targets observed with TIMMI2: older sources	66
4.9	Results for the older TIMMI2 targets	67
4.10	Dust mass ratios for the older TIMMI2 targets	73
4.11	Dust mass limits for the older TIMMI2 targets	75
5.1	Photometry of ϵ Eri	82

Bibliography

- Ábrahám, P., Kóspál, Á., Csizmadia, Sz., et al. 2004, A&A, in press, astro-ph/0408048
- Acke, B., van den Ancker, M.E., Dullemond, C.P., van Boekel, R., & Waters, L.B.F.M. 2004a, A&A, 422, 621
- Acke, B., & van den Ancker, M.E. 2004b, A&A, in press, astro-ph/0406050
- André, P., Ward-Thompson, D., & Barsony, M. 1993, ApJ 406, 122
- André, P. 1994; in “The Cold Universe”; eds. Montmerle, T., Lada, C.J., Mirabel, I.F., Tran Thanh Van, J. (Gif-sur-Yvette, France: Editions Frontieres); 179
- Andrews, S.M., Rothberg, B., & Simon, T. 2004, ApJ, 610, L45
- Apai, D., Pascucci, I., Brandner, W., et al. 2004, A&A, 415, 671
- Augereau, J.C., Lagrange, A.M., Mouillet, D., Papaloizou, J.C.B., & Grorod, P.A. 1999a, A&A, 348, 557
- Augereau, J.C., Lagrange, A.M., Mouillet, D., & Ménard, F. 1999b, A&A, 350, L51
- Aumann, H.H., Beichman, C.A., Gillett, F.C., et al. 1984, ApJ, 278, L23
- Aumann, H.H. 1988, AJ, 96, 1415
- Backman, D.E., & Paresce, F. 1993, in “Protostars and Planets III”, eds. Levy, E.H., Lunine, J.I., & Mathews, M.S. (Tucson: Univ. Arizona Press), 1253
- Barrado y Navascués, D., Stauffer, J.R., Song, I., & Caillaut, J.-P. 1999, ApJ 520, L123
- Beuzit, J.L., Mouillet, D., Lagrange, A.M., & Paufique, J. 1997, A&AS, 125, 175
- Bhatt, H.C., & Manoj, P. 2000, A&A, 362, 978
- Boccaletti, A., Augereau, J.C., Marchis, F., & Hahn, J. 2003, ApJ, 585, 494
- Bouwman, J., Meeus, G., de Koter, A., et al. 2001, A&A, 375, 950 [= B2001]
- Bradley, J. 2003, in “The Astromineralogy of Interplanetary Dust Particles”, ed. Henning, T.K. (Berlin Springer Verlag), 217
- Bregman, J.D., Witteborn, F.C., Allamandola, L.J., et al. 1987, A&A, 187, 616
- Chen, C.H., & Jura, M. 2001, ApJ, 560, L171
- Chiang, E.I., & Goldreich, P. 1997, ApJ, 490, 368
- Chini, R., Krügel, E., & Kreysa, E. 1990, A&A, 227, L5
- Chini, R., Krügel, E., Kreysa, E., Shustov, B., & Tutukov, A. 1991, A&A, 252, 220

- Chini, R., Kämpgen, K., Reipurth, B., et al. 2003, *A&A*, 409, 235
- Clampin, M., Krist, J.E., Ardila, D.R., et al. 2003, *AJ*, 126, 385
- Cohen, M., & Witteborn, F.C. 1985, *ApJ*, 294, 345
- Crovisier, J., Leech, K., Bockelée-Morvan, D., et al. 1997, *Science*, 275, 1904
- Decin, G., Dominik, C., Malfait, K., Mayor, M., & Waelkens, C. 2000, *A&A*, 357, 533
- Decin, G., Dominik, C., Waters, L.B.F.M., & Waelkens, C. 2003, *ApJ*, 598, 636
- Dominik, C., Dullemond, C.P., Cami, J., & van Winckel, H. 2003a, *A&A*, 397, 595
- Dominik, C., Dullemond, C.P., Waters, L.B.F.M., & Walch, S. 2003b, *A&A*, 398, 607
- Dorschner, J., Begemann, B., Henning, Th., Jaeger, C., & Mutschke, H. 1995, *A&A*, 300, 503
- Draine, B.T., & Lee, H.M. 1984, *ApJ*, 285, 89
- Dullemond, C.P., Dominik, C., & Natta, A. 2001, *ApJ*, 560, 957
- Dullemond, C.P. 2002, *A&A*, 395, 853
- Fabian, D., Jäger, C., Henning, Th., Dorschner, J., & Mutschke, H. 2000, *A&A*, 364, 282
- Fabricius, C., & Makarov, V.V. 2000, *A&A*, 356, 141
- Fajardo-Acosta, S.B., & Knacke, R.F. 1995, *A&A*, 295, 767
- Fekel, F.C., Scarfe, C.D., Barlow, D.J., et al. 2002, *AJ*, 123, 1723
- Gehrz, R.D., Smith, N., Low, F.J., et al. 1999, *ApJ*, 512, L55
- Grady, C.A., Devine, D., Woodgate, B., et al. 2000, *ApJ*, 544, 895
- Graham, J.A., & Frogel, J.A. 1985, *ApJ*, 289, 331
- Greaves, J.S., Holland, W.S., Moriarty-Schieven, G., et al. 1998, *ApJ*, 506, L133
- Greaves, J.S., Coulson, I.M., & Holland, W.S. 2000, *MNRAS*, 312, L1
- Greaves, J.S., & Wyatt, M.C. 2003, *MNRAS*, 345, 1212
- Greaves, J.S., Holland, W.S., Jayawardhana, R., Wyatt, M.C., & Dent, W.R.F. 2004, *MNRAS*, 348, 1097
- Gredel, R. 1994, *A&A*, 292, 580
- Habart, E., Testi, L., Natta, A., & Vanzi, L. 2003, *A&A*, 400, 575
- Habing, H.J., Dominik, C., Jourdain de Muizon, M., et al. 2001, *A&A*, 365, 545
- Hallenbeck, S., & Nuth, J. 1997, *Ap&SS*, 255, 427
- Hanner, M.S., Brooke, T.Y., & Tokunaga, A.T. 1998, *ApJ*, 502, 871
- Hartmann, L., & Kenyon, S.J. 1996, *ARA&A*, 34, 207
- Hatzes, A.P., Cochran, W.D., McArthur, B., et al. 2000, *ApJ*, 544, L145
- Herbig, G.H., Petrov, P.P., & Duemmler, R. 2003, *ApJ*, 595, 384
- Holland, W.S., Greaves, J.S., Dent, W.R.F., et al. 2003, *ApJ*, 582, 1141
- Honda, M., Kataza, H., Okamoto, Y.K., et al. 2003, *ApJ*, 585, L59

- Hony, S., Van Kerckhoven, C., Peeters, E., et al. 2001, *A&A*, 370, 1030
- Ibragimov, M.A., & Shevchenko, V.S. 1990, in “Conf. on Classical Be stars and Ae/Be Herbig Stars”; ed. Mamatkazina, A.Kh. (Alma Ata)
- Jaeger, C., Molster, F.J., Dorschner, J., et al. 1998, *A&A*, 339, 904
- Jayawardhana, R., Holland, W.S., Greaves, J.S., et al. 2000, *ApJ*, 536, 425
- Jeans, J.H. 1922, in “The nebular hypothesis and modern cosmogony”
- Jourdain de Muizon, M., Laureijs, R.J., Dominik, C., et al. 1999, *A&A*, 350, 875
- Jura, M., Webb, R.A., & Kahane, C. 2001, *ApJ*, 550, L71
- Kalas, P., Liu, M.C., & Matthews, B.C. 2004, *Science*, 303, 1990
- Kemper, F., Vriend, W.J., & Tielens, A.G.G.M. 2004, *ApJ*, 609, 826
- Koerner, D.W., Jensen, E.L.N., Cruz, K.L., Guild, T.B., & Gultekin, K. 2000, *ApJ*, 533, L37
- Koresko, C.D., Beckwith, S.V.W., Ghez, A.M., Matthews, K., & Neugebauer, G. 1991, *AJ*, 102, 2073
- Kuhn, J.R., Potter, D., & Parise, B. 2001, *ApJ*, 553, L189
- Kurucz, R.L. 1994, “Solar abundance model atmospheres for 0,1,2,4,8 km/s”, CD-ROM No. 19. (Cambridge, Mass.: Smithsonian Astrophysical Observatory)
- Lachaume, R., Dominik, C., Lanz, T., & Habing, H.J. 1999, *A&A*, 348, 897
- Lada, C.J. 1987, *IAU Symp.* 115, 1
- Laplace, P.S. 1796, in “Exposition du système du Monde”
- Laureijs, R.J., Jourdain de Muizon, M., Leech, K., et al. 2002, *A&A*, 387, 285
- Li, A., Lunine, J.I., & Bendo, G.J. 2003, *ApJ*, 598, L51
- Liseau, R. 1999, *A&A*, 348, 133
- Liu, M.C. 2004, *Science*, in press, astro-ph/0408164
- Malfait, K., Bogaert, E., & Waelkens, C. 1998a, *A&A*, 331, 211
- Malfait, K., Waelkens, C., Waters, L.B.F.M., et al. 1998b, *A&A*, 332, L25
- Mamajek, E.E., Meyer, M.R., & Liebert, J. 2002, *AJ*, 124, 1670
- Mannings, V. 1994, *MNRAS*, 271, 587
- Mannings, V., & Barlow, M.J. 1998, *ApJ*, 497, 330
- Mannings, V., & Sargent, A.I. 2000, *ApJ*, 529, 391
- Mayor, M., in “Extrasolar Planets: Today and Tomorrow”, ASP Conference Series, in press
- Meeus, G., Waters, L.B.F.M., Bouwman, J., et al. 2001, *A&A*, 365, 476 [= M2001]
- Meeus, G., Bouwman, J., Dominik, C., Waters, L.B.F.M., & de Koter, A. 2002, *A&A*, 392, 1039
- Meeus, G., Sterzik, M., Bouwman, J., & Natta, A. 2003, *A&A*, 409, L25
- Meyer, M.R., Backman, D., Mamajek, E.E., et al. 2001, *AAS*, 199, 7608

- Mouillet, D., Lagrange, A.M., Beuzit, J.L., & Renaud, N. 1997, *A&A*, 324, 1083
- Natta, A., Testi, L., Neri, R., Shepherd, D.S., & Wilner, D.J. 2004, *A&A*, 416, 179
- Oudmaijer, R.D., van der Veen, W.E.C.J., Waters, L.B.F.M., et al. 1992, *A&AS*, 96, 625
- Padgett, D.L., Brandner, W., Stapelfeldt, K.R., et al. 1999, *AJ*, 117, 1490
- Pantin, E., Waelkens, C., & Lagage, P.O. 2000, *A&A*, 361, L9
- Perryman, M.A.C., Lindegren, L., Kovalevsky, J., et al. 1997, *A&A*, 323, L49
- Piétu, V., Dutrey, A., & Kahane, C. 2003, *A&A*, 398, 565
- Pollack, J.B., Hubickyj, O., Bodenheimer, P., et al. 1996, *Icarus*, 124, 62
- Prato, L., Ghez, A.M., Piña, R.K., et al. 2001, *ApJ*, 549, 590
- Prusti, T., Bontekoe, Tj.R., Chiar, J.E., Kester, D.J.M., & Whittet, D.C.B. 1993, *A&A*, 279, 163
- Przygodda, F., van Boekel, R., Àbrahàm, P., et al. 2003, *A&A*, 412, L43
- Quillen, A.C., & Thorndike, S. 2002, *ApJ*, 578, L149
- Racine, R., Walker, G.A.H., Nadeau, D., Doyon, R., & Marois, C. 1999, *PASP*, 111, 587
- Reichertz, L.A., Weferling, B., Esch, W., & Kreysa, E. 2001, *A&A*, 379, 735
- Reipurth, B., Chini, R., Krugel, E., Kreysa, E., & Sievers, A. 1993, *A&A*, 273, 221
- Reipurth, B., & Aspin, C. 1997, *AJ*, 114, 2700
- Reipurth, B., Hartmann, L., Kenyon, S.J., Smette, A., & Bouchet, P. 2002, *AJ*, 124, 2194
- Rietmeijer, F.J.M. 1989, in "Lunar and Planetary Science Conference, 19th", Proceedings A89-36486 15-91 (Cambridge University Press / Lunar and Planetary Institute), 513
- Roddier, F., & Roddier, C. 1997, *PASP*, 109, 815
- Saffe, C., & Gómez, M. 2004, *A&A*, 423, 221
- Sandell, G. & Weintraub, D.A. 2001, *ApJ Supp.*, 134, 115
- Schneider, G., Becklin, E.E., Smith, B.A., et al. 2001, *AJ*, 121, 525
- Servoin, J.L., & Piriou, B. 1973, *Phys. Stat. Sol. B*, 55, 677
- Sheret, I., Dent, W.R.F., & Wyatt, M.C. 2004, *MNRAS*, 348, 1282
- Sitko, M.L., Lynch, D.K., & Russel, R.W. 2000, *AJ*, 120, 2609
- Sivaramakrishnan, A., Koresko, C.D., Makidon, R.B., Berkefeld, T., & Kuchner, M.J. 2001, *ApJ*, 552, 397
- Soderblom, D.R., & Däppen, W. 1989, *ApJ*, 342, 945
- Song, I., Caillault, J.-P., Barrado y Navascués, D., & Stauffer, J.R. 2001, *ApJ*, 546, 352
- Spitzer, W.G., & Kleinman, D.A. 1961, *Phys. Rev.*, 121, 1324
- Starck, J.L., Abergel, A., Aussel, H., et al. 1999, *A&AS*, 134, 135
- Stern, S.A., Weintraub, D.A., & Festou, M.C. 1994, *IAU Circ.*, 6003, 3
- Strom, K.M., & Strom, S.E. 1993, *ApJ*, 412, L63

- Sylvester, R.J., Skinner, C.J., Barlow, M.J., & Mannings, V. 1996, *MNRAS*, 279, 915
- Sylvester, R.J., & Mannings, V. 2000, *MNRAS*, 313, 73
- Sylvester, R.J., Dunkin, S.K., & Barlow, M.J. 2001, *MNRAS*, 327, 133
- Tanaka, H., Inaba, S., & Nakazawa, K. 1996, *Icarus*, 123, 450
- Trilling, D.E., & Brown, R.H. 1998, *DPS*, 30, 23.03
- Trilling, D.E., Brown, R.H., & Rivkin, A.S. 2000, *ApJ*, 529, 499
- Van Boekel, R., Waters, L.B.F.M., Dominik, C., et al. 2003, *A&A*, 400, L21
- Van den Ancker, M.E., Blondel, P.F.C., Tjin A Djie, H.R.E., et al. 2004, *MNRAS*, 349, 1516
- Vieira, S.L.A., Corradi, W.J.B., Alencar, S.H.P., et al. 2003, *AJ*, 126, 2971
- Walker, H.J., & Heinrichsen, I. 2000, *Icarus*, 143, 147
- Webb, R.A., Zuckerman, B., Platais, I., et al. 1999, *ApJ*, 512, L63
- Weidenschilling, S.J., & Cuzzi, J.N. 1993; in "Protostars and Planets III"; eds. Levy, E.H., Lunine, J.I., & Mathews, M.S. (Tucson: Univ. Arizona Press); 1031
- Weingartner, J.C., & Draine, B.T. 2001, *ApJ*, 548, 296
- Wetherill, G.W., & Stewart, G.R. 1993, *Icarus*, 106, 190
- Wilner, D.J., Holman, M.J., Kuchner, M.J., & Ho, P.T.P. 2002, *ApJ*, 569, L115
- Wolf, S., & Hillenbrand, L.A. 2003, *ApJ*, 596, 603
- Zuckerman, B., & Becklin, E.E. 1993, *ApJ*, 414, 793
- Zuckerman, B., Forveille, T., & Kastner, J.H. 1995, *Nature*, 373, 494
- Zuckerman, B., & Webb, R.A. 2000, *ApJ*, 535, 959
- Zuckerman, B. 2001, *ARA&A*, 39, 549
- Zuckerman, B., Song, I., Bessell, M.S., & Webb, R.A. 2001, *ApJ*, 562, L87
- Zuckerman, B., & Song, I. 2004, *ApJ*, 603, 738